Comprehensive Analysis of Pre-Charge Sequence in Automotive Battery Systems

Murat Kubilay Ozguc, Eymen Ipek, Kadir Aras and Koray Erhan
Software&Electronics, AVL Research&Engineering, Istanbul, Turkey

***Abstract*—Electric vehicles (EV) have brought promising technologies for future mobility solutions. As one of the key components of EVs, battery systems have fundamental functions which disconnect the battery during parking and in case of failure. To provide a safe system, specialized high voltage (HV) electromechanical switches are used to perform these major functions such as switch on, switch off or pre-charging. Due to these components can be easily damaged, expensive, heavy and bulky, a solution based on pure semiconductors may be desired to accomplish these operations. Many studies were exhibited on EV battery systems regarding developing solid-state systems for HV switchgear. Developing technology on semiconductor devices allows to make a safety concept based on only solid-state components. This study presents a comprehensive analysis of pre-charge sequences between conventional and semiconductor switchgear to be used in electric vehicle battery systems. Spice simulations are presented to investigate advantages and drawbacks of these systems.**

***Index Terms*—electric vehicles, battery systems, li-ion, pre-charge, semiconductor**

I. INTRODUCTION

Climate change concern has become a major driver for CO_2 reduction regulations, and this brings the necessity of zero-emission transportation which ensures a decrease in local air pollution and noise emissions. Therefore, electric vehicles (EV) have received tremendous attention. By using EVs, engineers and scientists not only provide a cleaner and quieter atmosphere but also drastically reduce operating costs compared to gas-powered vehicles. Electric vehicles spend approximately 0.015 $/km, while ICE vehicles spend 0.08 $/km [1]. The increasing need for electric vehicles brought high power and energy requirements. Due to these requirements, battery packs of passenger vehicles rated at 400-600 V, sports and commercial vehicles have battery packs at the levels of 800-1000 V [2]. In addition to that, as an energy source, lithium-ion (Li-ion) batteries are utilized in electric vehicles. Usually, DC currents of approximately 300 A are needed when riding such vehicles over longer periods of time. Electric parts big in geometric size that are not simple to package in a battery scheme are needed to manage heat losses when carrying such currents. This will also lead to elevated cost and weight. EVs with voltages up to 800 V are currently targeted which will decrease the current levels in heavy load driving conditions. As a result, wiring and connectors are relatively small and can, therefore, overcome the issues described above. Conventional battery disconnect unit (BDU) of EV batteries basically consist of contactors, fuses, sensors, battery management system and connectors. Usage of semiconductors instead of contactors also brings the reduction of size and increase in efficiency [3]. Automotive applications require reliable systems over the lifetime in terms of mechanical shocks, vibrations, electrical instability, temperature and humidity conditions. Even tough mechanical and electro-mechanical components are proven against these, there is a chance to improve system performance. Especially in automotive high voltage (HV) battery systems, electromechanical parts can present a bottleneck. For instance, mechanical relays can require certain mounting positions considering their contact working axis.

Over the past few years, the use of SiC-based power semiconductor alternatives has shown enormous growth, relying on its revolution. The driving forces behind this growth of the industry are the following trends: saving energy, reducing the size, integrating the system and improving reliability [4]. Despite semiconductors' challenges, they can be used in automotive battery systems in lots of areas thanks to their compact design. Either pre-charge relay or main relay can be replaced by semiconductor switches. This will lead to a more reliable system in terms of vibration and shock. Also, this allows that the system is a thousand times faster for fault diagnosis and response. Besides, it is possible to decrease weight up to 60% and the volume reduction is up to 80% [5]. Studies on this subject generally present a solution which is having a semiconductor in parallel or in series to contactor [6]–[8]. On the other hand, some researches propose a method which consists a DC-DC converter in series with main relay is used for pre-charging action [9]–[11]. However, it is aimed to remove the main relay and control the power flow by using stand alone semiconductor. Moreover, the rapid progress of semiconductor technologies will enable this approach to become widespread and used in practice. At the inverter input, filter capacitors exist, that generate a severe inrush current when the circuit is closed. If this current is not limited, it may damage the cells, contactors or other battery system components. The functional requirement of the high voltage pre-charge circuit is to minimize the peak current out from the power source by slowing down the dV/dT of the input voltage. In this paper, it is compared the characteristics of the conventional pre-charging with pre-charging with semiconductor switches by SPICE simulation results.

OPEN ACCESS
TRANSACTIONS ON ENVIRONMENT AND ELECTRICAL ENGINEERING ISSN 2450-5730 Vol 4, No 1 (2020)

II. SYSTEM PARAMETERS

Tesla Model S is chosen because it is a popular vehicle and easy to reach the system specifications. The battery pack specifications of the Tesla Model S 100P is selected to determine the simulation parameters in Fig. 1. As shown in Table I, the maximum voltage of the package is 403.2 V_{DC} within the package configuration is 16 modules in series that every module has 6 series 86 parallel cell configuration. Panasonic NCR18650B cells are used in the selected battery pack with nominal cell resistances of 18 mΩ and considering the contact resistances and internal resistances of the BDU components, the total equivalent resistance of the pack is calculated as 22.10 mΩ by using Eq.(1). Equivalent inductance values of the elements in the package and the cables going from the package to the inverter are accepted as 30 µH in total. The values in the table are official values besides the cell inner resistance, stray inductance and DC link capacity. These values are determined according to AVL know-how.

$$R_{\text{BS}} = ((R_{\text{DCIR}} + 2 * R_{\text{c}}) * \frac{n_{\text{s}}}{n_{\text{p}}}) * n_{\text{m}} + R_{\text{MB}} + R_{\text{BDU}} \tag{1}$$

where;

- R_{BS}: Battery system resistance
- R_{DCIR}: DC internal resistance
- R_c: Contact resistance of the cells
- R_{MB}: Module busbar resistance
- R_{BDU}: BDU components' resistance
- n_m: Number of modules
- n_s: Number of cells in series
- n_p: Number of cells in parallel

By using Eq.(1), Battery System Resistance is calculated as 22.10 mΩ. The busbar plates that make the connection of modules are accepted as they have resistance of 1 mΩ and BDU components accepted as they have 1 mΩ internal resistance.

TABLE I
SYSTEM PARAMETERS [12]

Parameter	Value
Vehicle Model	Tesla Model S
Battery Capacity	100 kWh
Pack Configuration	16 MS (6S86P)
Nominal Cell Voltage	3.6
Maximum Cell Voltage	4.2
Cell Inner Resistance (@3.6 V)	18 mΩ
Nominal Pack Voltage	345.6 V
Maximum Pack Voltage	403.2 V
Stray Inductance	30 µH
Battery System Resistance	22.10 mΩ
DC Link Capacity (Tolerance)	550 µF (m%10)
Voltage Difference	5 V

III. CONVENTIONAL PRE-CHARGE

When DC power source is applied to a capacitive load, the step response of the voltage input will cause the input capacitor to charge. The capacitor charging starts with inrush current and ends with an exponential decay down to the steady state condition. The current drawn by a capacitor can be calculated by using Eq.(2).

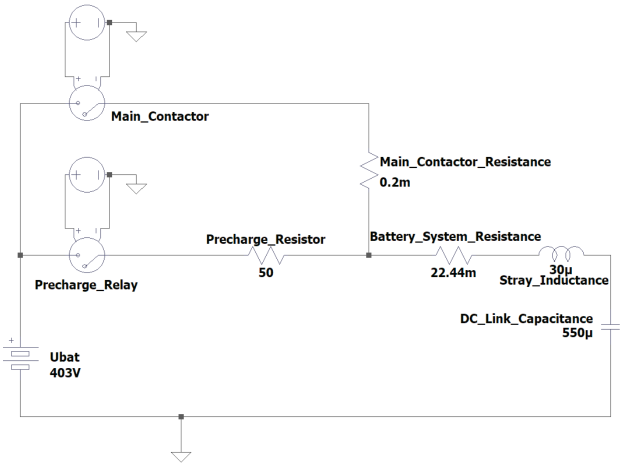

Fig. 1. Simulation circuit with contactor.

$$I_{\text{C}} = C * \frac{dV}{dt} \tag{2}$$

where;

- I_C: Current passing through capacitor
- C: DC capacitance of battery system in Farads
- dV: Voltage change in Volts
- dt: Time change in seconds

As can be seen in Eq.(2), the peak inrush current depends upon the capacitance C and the rate of change of the voltage (dV/dT). The functional requirement of the high voltage pre-charge circuit is to minimize the peak current out from the power source by slowing down the dV/dT of the input power voltage. Upon completion of the pre-charging sequence, the pre-charge resistor is switched out of the power supply circuit and returns to a low impedance power source for normal mode. In order to find inrush current, pre-charge resistor value can be calculated with Eq.(3). In this simulation, pre-charge time is decided as 120 ms and voltage difference between DC-Link capacitor and battery pack is determined as 5 V. With pre-charge time of 120 ms, pre-charge resistance is calculated as 49.79 Ω using Eq.(3). However, in the simulation, it is rounded up to 50 Ω.

$$R_{\text{pre}} = -\frac{t}{C * ln(\frac{\Delta U}{U_{\text{Bat.}_{\text{max}}}})} \tag{3}$$

where;

- R_{pre}: Resistance value of pre-charge resistor in Ω
- ΔU: Voltage change in Volts
- $U_{Bat._{max}}$: Maximum battery system voltage in Volts

In the simulation circuit, the capacity value is taken as 550 µF and start of the sequence have 10 ms delay to get a coherent output on graphs. The result of the simulation circuit shown in Figure 1 can be seen in Fig. 2, the capacity voltage has reached 398 V within 120 ms. At the end of 180 ms, there is no voltage difference between the capacity and the battery pack. Meanwhile, the pre-charge current reaches the peak value of 8 A at the start time (i.e. 10 ms), then exponentially reduces and cuts off around 180 ms.

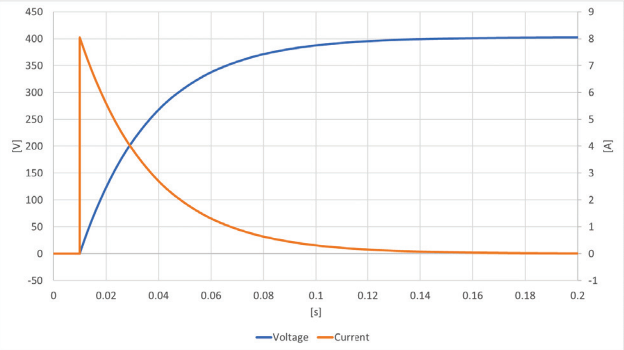

Fig. 2. Simulated pre-charge waveforms.

As shown in Fig. 3, the maximum power dissipated on pre-charge resistor is 3.25 kW. Consequently, in 120 ms sequence total energy loss is 44.71 Ws.

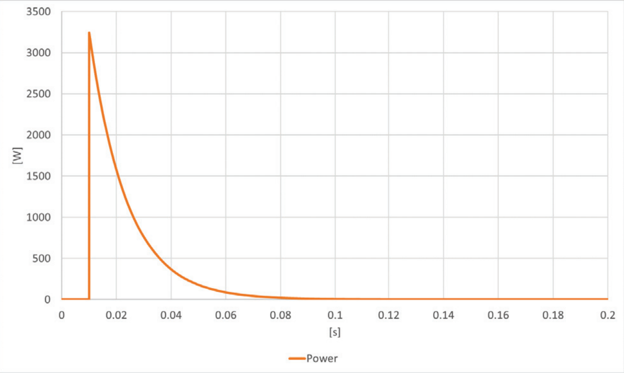

Fig. 3. Power dissipation on pre-charge resistor.

IV. PRE-CHARGE WITH SEMICONDUCTOR

On the other hand, the pre-charge sequence can be achieved by using semiconductor switches. A silicon-based switch allows not only removing pre-charge contactor but also resistor. At low to medium power levels which require few hundred volts of blocking capability, MOSFETs are ideal semiconductors to use in this application because they are capable of fast switching time against majority carrier devices, lower switching loss due to fast rise and fall times, uncomplicated gate drive and low $R_{DS(on)}$ to increase the efficiency by decreasing the voltage drop during steady state operation. Since this is an only a new and innovative method can be applied, it is assumed that only a single MOSFET to use which's parameters can be seen in Table II. However, to cover power ratings of general battery packs, semiconductors in the market need to be used in parallel.

TABLE II
SELECTED MOSFET PARAMETERS [13]

Parameter	Value	Unit
V_{DS}	650	V
$R_{DS(on)}$, Max	0.048	Ω
Continuous Drain Current (T_c=100C)	40	A
Pulsed Drain Current (T_c=25C)	228	A
Power Dissipation	500	W

Because of being automotive compatible, having low On-resistance and covering voltage spikes with its high voltage rating of 650 V, Infineon IPW65R048CFDA MOSFET model is used in these SPICE simulations which can be seen in Fig. 4.

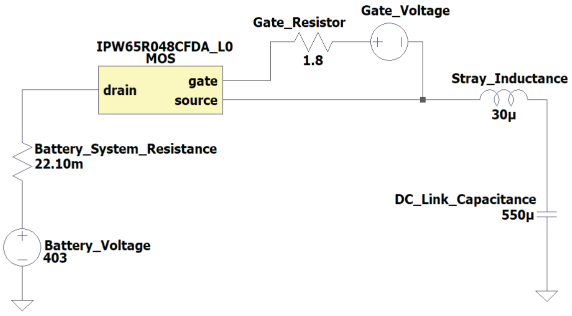

Fig. 4. Simulation circuit with semiconductor.

A. *Pre-charging with PWM Method*

The capacitor charge can be done via PWM switching of semiconductors since a switching action will block inrush currents from the battery until the difference is acceptable. After the capacitors reached a certain voltage level, semiconductors can be turned-on fully. As seen in Fig. 5, DC link voltage rises while pre-charge current stays at same level with approximately 10 A in MOSFET's on state.

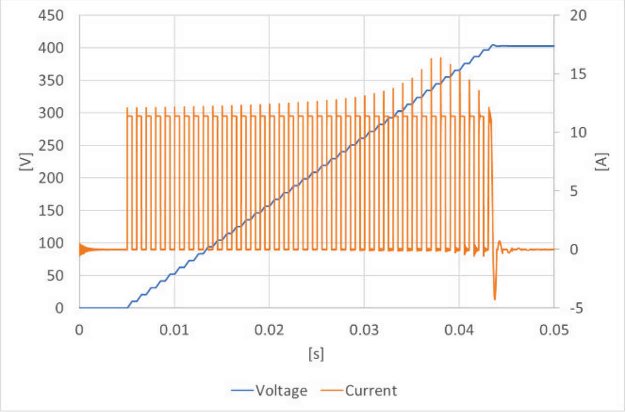

Fig. 5. PWM method DC-Link capacitance waveforms.

This method can adjust the peak value of inrush current and settling time by PWM control sequence of MOSFET as shown in Fig. 6. However, it has a limitation due to switching losses of PWM operation and needs proper heatsink design.

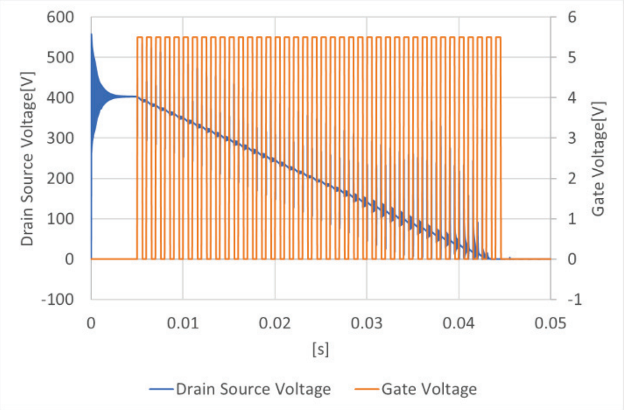

Fig. 6. MOSFET voltage waveforms.

As shown in Fig. 7, the maximum power dissipated on MOSFET during PWM operation reaches to 5.275 kW peak. Consequently, in 40 ms sequence, total energy loss is 44.60 Ws.

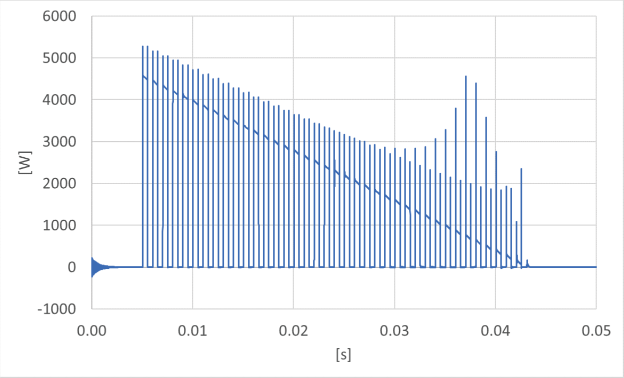

Fig. 7. Power dissipation on MOSFET.

B. Pre-charging with Controlling the Turn–on Switching of MOSFET

Limitation of inrush current comes from the gate charge characteristic of MOSFET when the device is turned on. The gate charge characteristic is originated from the equivalent capacitance of the MOSFET [14]. The quicker the capacitance is charged and discharged will dictate the easier the system turns on or off. The most efficient way to obtain and control the MOSFET switching mechanism is by using the gate-charge transfer curves provided on datasheet [15].

Fig. 8 shows the turn–on gate–charge transfer curve from SPICE simulation. This curve shows how the voltage curve pattern of V_{GS} and V_{DS} changes for limiting the drain current which is also same current that flows through dc-link capacitor.

Pre–threshold region and the constant current are used for rising of V_{GS} to device threshold voltage V_{th} at a linear slope. When V_{GS} has reached the V_{th}, the drain current rises to its steady state region. After that, the drain–source voltage starts its transition and the gate–charge transfer curve starts to level off. As the voltage across the drain–gate reduces even more. DC Link capacity voltage as can be seen in Fig. 9 reaches its expected value. Gate voltage is increased and MOSFET starts conduct as full on mode. Since changes in drain–source voltage affects drain current, the pre-charging time collaborates with gate voltage directly. The drain voltage control capability will allow the dV_{DS}/dt to be fully controlled independently of the load condition. The ability to control dV_{DS}/dt will allow the capacitive load or resistive load to be controlled by the inrush current [7].

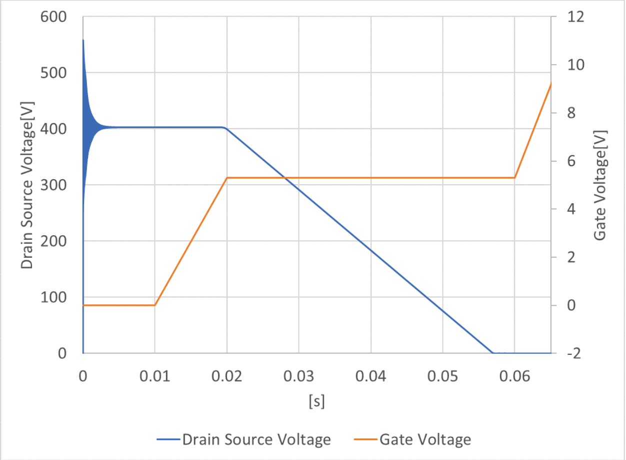

Fig. 8. MOSFET gate charge transfer curve.

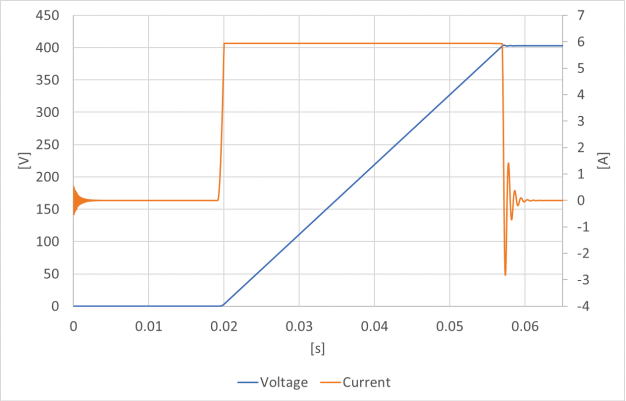

Fig. 9. Linear mode method DC-Link capacitance waveforms.

As shown in Fig. 10, the maximum power dissipated on MOSFET during Turn-on switching operation reaches to 2400 kW peak. Consequently, in 40 ms sequence total energy loss is 44.65 Ws.

Oscillations which are seen in Fig. 5, 6, 7, 8, 9 will occur in real system. Therefore, it is necessary to use snubber circuit for absorbing oscillations during switching in experimental studies.

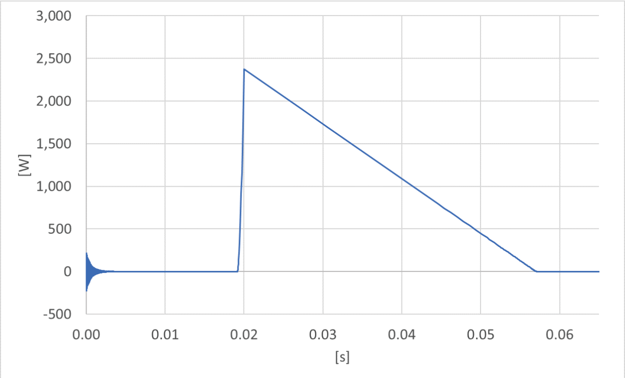

Fig. 10. Power dissipation on MOSFET.

V. Conclusion

As shown in Table III, pre-charge sequence can be performed 80 ms faster by using semiconductor, while maximum power loss varies depending on which active pre-charge method is used. In contrast to the 2.34 kW power dissipation value of the pre-charge sequence with the conventional resistance, peak values reach the value of 5.28 kW in the PWM method and 2.38 kW in turn-on control method. Since the energy stored in the capacitor depends on voltage applied and the capacity of capacitor, in all 3 simulations energy losses are similar. However, in addition to these results, it should be taken into consideration that semiconductor solutions will be much lighter and take up less space than mechanical relay solutions. On the other hand, semiconductor switchgears need cooling unlike mechanical relays. According to all findings in this paper, it can be clearly seen that the usage of stand-alone semiconductor switch gear empowers pre-charging action in automotive battery systems with its notable advantages compared to a conventional mechanical relay system. Moreover, solid-state technology is more reliable against mechanical shocks, electrical abnormalities, and environmental conditions. Besides, there is no strict requirement of mounting of solid-state circuits. Semiconductors can react in microseconds during electrical failures. Thanks to superiorities of semiconductors comparing electro-mechanical parts, one can say that they will surpass their current usage areas. In the near future, they will be used in many additional areas as well as automotive battery systems.

References

[1] Siang Fui Tie, Chee Wei Tan "A review of energy sources and energy management system in electric vehicles", Renewable and Sustainable Energy Reviews, vol. 20, pp 82-102, April 2013.

[2] ZVEI, "Voltage cases for electric mobility" p. 11-12. Available: zvei.org/fileadmin/user_upload/Presse_und_Medien/Publikationen/2014/april/Voltage_Classes_for_Electric_Mobility/Voltage_Classes_for_Electric_Mobility.pdf [Accessed November 20, 2019].

[3] AVL Trimerics GmbH, High Performance 800v E-Motor for Automotive Application, Available: https://bit.ly/2k9Q4YS [Accessed November 20, 2019].

[4] Friedrichs, P., Buschkuehle, M. (2016). The Future of Power Semiconductors : Rugged and High Performing Silicon Carbide Transistors.

TABLE III
Comparison Between Switchgears

	Mechanical Relay	Semiconductor Switchgear	
Parameter	Pre-Charge Resistor	PWM Method	Turn-On Control Method
Time [ms]	120	40	40
Maximum Power Dissipation [kW]	3.24	5.28	2.38
Energy Loss [Ws]	44.71	44.60	44.65
Volume [l]	>1	<1	
Weight [Kg]	>1	<1	
Cooling	Not necessary	Required	

[5] Rößler, Werner. "When Do We Get the Electronic Battery Switch?." In Advanced Microsystems for Automotive Applications 2014, pp. 165-177. Springer, Cham, 2014.

[6] Parrish, R., Elankumaran, K., Gandhi, M., Nance, B., Meehan, P., Milburn, D., ... & Brenz, A. (2011). Voltec battery design and manufacturing (No. 2011-01-1360). SAE Technical Paper.

[7] Mensah-Brown, A. K., Hashim, H. R., Blakemore, B. C., & Gale, A. R. (2017). U.S. Patent No. 9,573,474. Washington, DC: U.S. Patent and Trademark Office.

[8] Burkman, W. E., & Sturza, J. (2018). U.S. Patent Application No. 15/469,012.

[9] Soldati, A., Imamovic, E., & Concari, C. (2019). Bidirectional Bootstrapped Gate Driver for High-density SiC-based Automotive DC/DC Converters. IEEE Journal of Emerging and Selected Topics in Power Electronics.

[10] Blakemore, B. C., Gale, A. R., Degner, M. W., Mensah-Brown, A. K., & Wang, C. L. (2015). U.S. Patent Application No. 14/250,231.

[11] Mensah-Brown, A. K., Gale, A. R., Blakemore, B. C.,& Wang, C. L. (2017). U.S. Patent No. 9,796,288. Washington, DC: U.S. Patent and Trademark Office.

[12] Tesla Motors. "Tesla Model S. Palo Alto" Available: http://my.teslamotors.com/de_DE/models/design, [Accessed 2015].

[13] Infineon, "650V CoolMos CFDA Power Transistor" IPW65R048CFDA datasheet, Mar. 2012.

[14] Lee, Eun-Ju, Jung-Hoon Ahn, Seung-Min Shin, and Byoung-Kuk Lee. "Comparative analysis of active inrush current limiter for high-voltage DC power supply system." In IEEE Vehicle Power and Propulsion Conference 2012, pp. 1256-1260. IEEE 2012.

[15] Motorola Inc, Applitaction Note AN1542.

Kubilay OZGUC was born in 1996 in Istanbul/Turkey. He received his BSc in Electrical Engineering from Yıldız Technical University (YTU), Turkey in 2018. Then he started to his MSc in Electrical Engineering at Istanbul Technical University (ITU) in 2019 and he is a MSc student in ITU. He had worked on power electronics and renewable energy during his BSc. He is currently working as Battery Development Engineer in the field of Battery Systems at AVL R&D Company, Turkey.

Eymen IPEK was born in 1995 in Istanbul/Turkey. He received his BSc in Electrical Engineering from Istanbul Technical University (ITU), Turkey in 2017. Then he started to his MSc in Electrical Engineering at Istanbul Technical University in 2017 and he is a MSc student in ITU. He had worked on power electronics, electric & hybrid electric vehicles, Li-Ion batteries and battery systems topics during his BSc. He is currently holding position of Battery Development Engineer in the field of Battery Systems at AVL R&D Company, Turkey. He has published 2 papers about battery systems for electric & hybrid electric vehicles.

Kadir ARAS was born in 1994 in Antalya/Turkey. He received his BSc in Electrical Engineering from Istanbul Technical University (ITU), Turkey in 2018. He had worked on renewable energy sources, electric & hybrid electric vehicles, Li-Ion batteries and battery systems topics during his BSc. He is currently holding position of Battery Development Engineer in the field of Battery Systems at AVL R&D Company, Turkey. He has published 1 paper about battery systems for electric & hybrid electric vehicles.

Koray ERHAN was born in 1987 in Turkey. He received his BSc in Electrical Engineering from Yildiz Technical University, Turkey in 2010. Then he completed his MSc in Electrical Engineering at Istanbul Technical University in 2013. Finally, he got his PhD at Department of Energy Systems Engineering, Kocaeli University in 2018. He became a research assistant in 2010 at Istanbul Technical University and in 2013 at Kocaeli University. He has published more than 30 papers in different subjects including electric & hybrid electric vehicles photovoltaic power generation systems, renewable energy sources, energy storage technologies, and smart grid integration and automation systems. He has been a referee in SCI and other indexed journals. He is currently holding position of Battery Development Engineer at AVL R&D Company, Turkey.

Feasibility Check of Electrification in Istanbul Metrobus Line

Turgay Gucukoglu, Haluk Sari and Koray Erhan
Software & Electronics, AVL Research & Engineering, Istanbul, Turkey

***Abstract*—Today, climate change is a significant effect of population growth, especially in big cities. Transport in metropolitan cities is the most important reason for climate change with the contribution of CO_2 pollution that threatens human health and the environment. Electrified transport systems can therefore provide a suitable solution to air pollution and health problems. This study investigates feasibility of applying electric buses to Metrobus line in Istanbul. Initially, Metrobus line data regarding to number of vehicles, number of stops, route length is gathered from official Istanbul transportation system to define how much energy is needed for the routes. Then, it is analyzed how to re-charge proposed batteries for allocation of chargers on the stations where is applicable.**

Keywords—Electric Bus, Metrobus, Electrification analysis

I. INTRODUCTION

With the urbanization in the world, the population of the city increases day by day. The increase in population causes serious damage to the city's natural environment and air quality. Public transportation plays a major role in cities to ensure urban sustainability in order to mitigate the effects of population growth. The decision which was initiated by major metropolises to gradually discontinue the purchase of fossil fuel buses has played an important role in zero-emission public transport systems. Moreover, improvements in battery capacities and fast charging systems have enabled many bus companies to expand their production and R&D (Research and Development) activities in the field of electric buses **[1].**

The buses used for public transportation can be divided into six types. These are diesel, compressed natural gas (CNG), biofuels, hybrid diesel, hydrogen, and electric bus (e-bus) **[2,3].** Although diesel buses are the most widely used bus type, hybrid and e-buses are alternative to conventional diesel buses **[4].** Furthermore, many of diesel bus manufacturers such as Man, Volvo, Iveco, VDL, and Irizar also manufacture e-buses. E-buses have been used in cities for short routes early on **[5,6].** Generally, the ranges of e-buses are between 30-300 km and battery capacities change between 76-340 kWh. The range of e-bus depends on some features such as battery capacity, charging methodology, cooling, driving cycle, etc. **[1,6].**

In this study, the case of replacement conventional buses with the e-buses is analyzed in accordance with the obtained data from a Metrobus line in Istanbul, Turkey. In conclusion, it is determined that which line is effective to transform the buses to electrified buses instead of conventional buses. In consideration of the data obtained, it is analyzed on which lines buses can be turned into electric buses. Metrobus line in Istanbul is the largest compared to similar applications around the world. Accordingly, electrifying such a big transportation line is a huge challenge. In addition, many studies are being carried out on the electrification of this line in Turkey. The results obtained here will serve as an example for similar applications in the world. In this context, relevant additions have been made to the study.

II. E-BUS

There has been a significant increase in e-bus production worldwide in recent years. In the European region, e-bus production accounts for 9% of global production. The size of e-bus fleet in European region and the USA is given in Fig. 1.

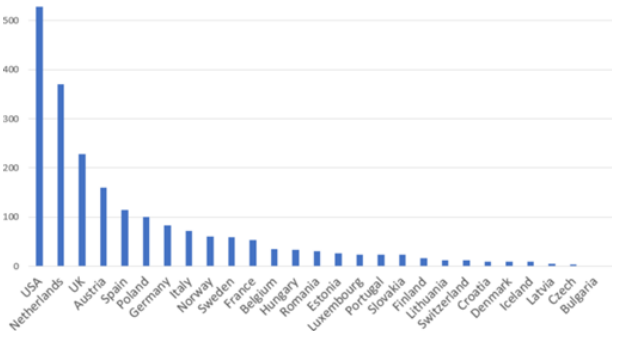

Fig. 1. The size of e-bus fleet in European region and USA **[7].**

Currently, the e-bus production leader in the world is China. There are currently 400,000 e-buses used in China. China accounts for 90% of the electric bus production in the world and 75% of the batteries of these electric buses in the world. LFP (Lithium Iron Phosphate ($LiFePO_4$)) batteries are used more than %97 in e-buses **[8].** Distribution of estimated bus market share in 2020 is given in Fig. 2.

In Turkey, the first electric bus was used in Konya in 2016 for public transportation. At the beginning of 2017, it was announced that 200 electric buses will be bought by IETT (Istanbul Electric Tram and Tunnel Operations) in Istanbul. The first e-bus domestic production was done by Bozankaya. With E-Karat, Turkey has gone into producing electric buses **[9].** The other e-bus manufacturer except Bozankaya are Otokar, Karsan, BMC, and TEMSA in Turkey **[10].** E-bus manufacturers in Turkey is given in Fig. 3.

E-buses differ in themselves in many ways, such as energy source type, charging strategy, charging refueling interface, on-board energy source, drive motor, drive topology, cooling and heating.

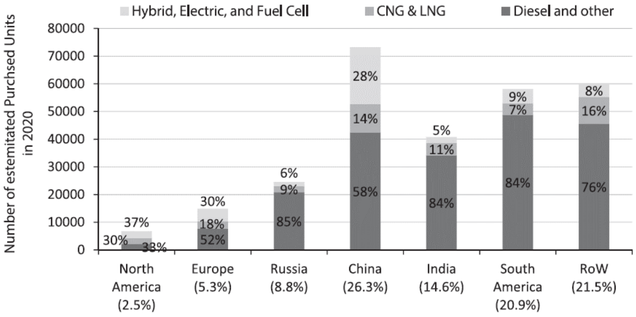

Fig. 2. Distribution of estimated bus market share in 2020 **[10].**

Fig. 3. E-bus manufacturers in Turkey **[11].**

LFP, NMC (Lithium Nickel Manganese Cobalt Oxide ($LiNiMnCoO_2$)), and LTO (Lithium Titanite (Li_2TiO_3)) are generally preferred as battery chemistry in electric buses. In addition to battery technology, it is used as a power source in addition to the battery in fuel cells and supercapacitors. Rails, low, medium and high voltage are used in addition to the built-in battery and H_2 tank to provide the necessary power to the electric buses. Opportunity, in motion, and depot are charging strategies used in e-bus. Manual, pantograph, induction, trolleybus current collector, and battery swapping methods are used to charge the battery. The most common types of electric motors used in electric buses are permanent magnet synchronous, electrically excited synchronous, asynchronous, and switched reluctance and central motor, and wheel hub motor are used as drive topologies. Body type of e-buses can be divided into 4 as 12 m single-deck, 18 m single-deck, 24 m bi-articulated and double-deck**.** Electric air-conditioning is used as a cooling system and electric resistance heating, electric heat pump, and fuel heating are preferred heating systems in e-buses **[12].**

According to UNECE (United Nations Economic Commission for Europe) regulations, there are vehicle categories which classify a land vehicle for regulatory purposes. In that categorization, M class is defined as 'Vehicles having at least four wheels and used for the carriage of passengers (e.g., standard car with 2, 3, 4 doors).' M class vehicles are also spread into 3 categories as M1, M2 and M3 which is directly referring to buses with the definition as 'Vehicles used for the carriage of passengers, comprising more than eight seats in addition to the driver's seat, and having a maximum mass exceeding 5 tones' [**13**].

The buses may also be categorized according to different specifications. Single decker, articulated, coach, midi-bus, mini-bus and double decker buses can be a categorization according to different use-cases while low floor, low entry and high floor buses can be another category according to design criteria. In this study, further specifications are evaluated regarding articulated class bus. Electrification feasibility of Metrobus line in Istanbul/Turkey is studied in the next sections.

III. Proposed E-bus concept for metrobus

The metrobus line where the study is carried out is in Istanbul. This metrobus line operates intercontinental and main target is to reduce traffic jam between crowded centers. With the capacity to carry 950,000 passengers per day, it is the largest among its kind in the world **[14].** There are 8 lines on the Metrobus route with 44 stations. The first and last stops of each of these lines are different. In addition, the number of buses operating on each line varies daily. Table I shows the numerical data of the metrobus line. There is a total of 495 buses moving along the line. These buses are grouped for each line. The distance covered for the shortest line is 11 km and the distance covered for the longest line is 52 km. Line and route information for each line is given in Table II. Route map is also seen in Figure 4.

When calculating the required battery capacity values, it is considered that a bus has the capacity to cover the longest line twice. The energy consumption value is 250 kWh / 100 km for the 19.725-meter bus and 239 kWh / 100 km for the 18.125-meter bus respectively. These consumption values are calculated by considering vehicle dynamics such as air drag force, rolling resistance, gear box loses, axle loses, etc.

TABLE I
METROBUS LINE GENERAL DATA

Route Number	Number of vehicles	Turnaround time (one cycle)	Track length (km)	Number of stops	Average vehicle speed (km/h)	Average turnaround time (s)	Total range per vehicle (km)
34	92	125	30	27	34	82	**423**
34A	22	94	22	20	30	256	**88**
34AS	100	162	41.5	35	31	97	**493**
34BZ	128	154	40	39	31	72	**562**
34C	70	115	29	26	35	99	**361**
34G	15	180	52	44	35	720	**260**
34U	38	40	11	6	38	63	**32**
34Z	30	52	11.5	8	31	104	**700**
Total	495	N/A	N/A	N/A	N/A	N/A	N/A

TABLE II
ROUTE FOR EACH METROBUS LINE

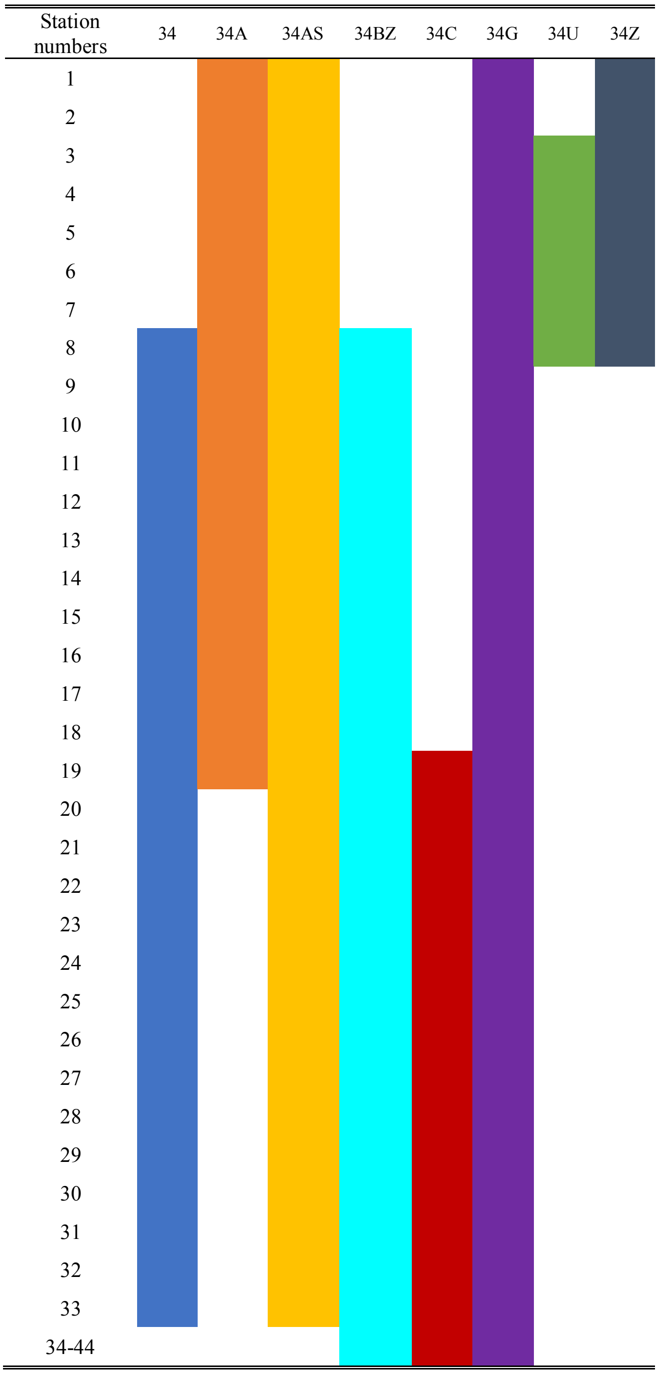

Station numbers	34	34A	34AS	34BZ	34C	34G	34U	34Z
1		■	■			■		■
2		■	■			■		■
3		■	■			■	■	■
4		■	■			■	■	■
5		■	■			■	■	■
6		■	■			■	■	■
7		■	■			■	■	■
8	■	■	■	■		■	■	■
9	■	■	■	■		■		
10	■	■	■	■		■		
11	■	■	■	■		■		
12	■	■	■	■		■		
13	■	■	■	■		■		
14	■	■	■	■		■		
15	■	■	■	■		■		
16	■	■	■	■		■		
17	■	■	■	■		■		
18	■	■	■	■		■		
19	■	■	■	■	■	■		
20	■		■	■	■	■		
21	■		■	■	■	■		
22	■		■	■	■	■		
23	■		■	■	■	■		
24	■		■	■	■	■		
25	■		■	■	■	■		
26	■		■	■	■	■		
27	■		■	■	■	■		
28	■		■	■	■	■		
29	■		■	■	■	■		
30	■		■	■	■	■		
31	■		■	■	■	■		
32	■		■	■	■	■		
33	■		■	■	■	■		
34-44				■	■	■		

Fig. 4. Metrobus line route on the map (blue line)

In the analyses, energy consumption value which is greater than the other is taken into consideration. One of the advantages of this is the production-based price advantage of using one type of battery. Figure 5 gives percentage of energy losses due to vehicle dynamics and auxiliary loads.

Detailed consumption data for buses is shown in Table III. In the calculations, the average speed value of the buses is taken as 40 km/h **[15].** The passenger carrying capacity of buses is a factor affecting on total weight. Both buses can carry a total of 160 passengers. In the calculations, the average occupancy rate is taken as 60% using with official data (IETT).

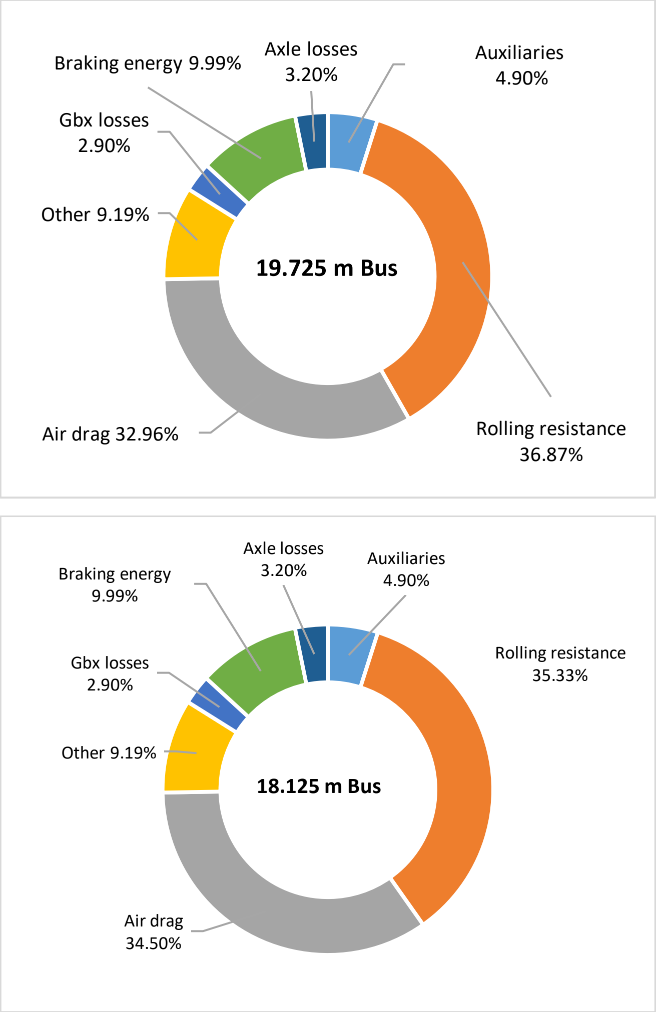

Fig. 5. Energy losses rates

The energy and power densities of the battery packs used in electric buses play important role which directly effects on vehicle range. Battery design should be made by considering the weight of the buses and the constant carrying of passengers throughout the day as it requires full time operation during a day. In this type of application, battery system is requested to deliver high number of cycles in demand. That demand is provided by LFP type cell which is suitable for high cycle life-time. Accordingly, the average number of cycles is assumed as 6000. The energy consumption values of buses carrying passengers on each line is given in Table IV. The total desired energy value plays important role in determining the battery capacity of buses.

Required energy for buses to make two cycles on the longest line (52 km) is approximately 520 kWh. However, this value is the usable energy required by bus. Batteries should not charge and discharge between 0% and 100% SoC (State of Charge) values. At that point, the concept of SoC window is defined. The energy value is given in here represents usable energy. SoC window value was determined as 5-92% in order to extend the life of the batteries. In this case, installed battery capacity value is calculated as 600 kWh.

According to the energy values obtained in Table IV, daily charge per vehicle is calculated in Table V. The purpose of this calculation is to determine how many times a day the bus with 600 kWh battery capacity needs to be charged. Calculations are made separately for all lines.

According to obtained data, buses operating on line 34 should be charged 187 times a day. Considering buses that start to operate in this line, each bus needs to be charged about 2 times a day. These values are given in Table V for each line code. Total desired Bus/Charge number for all metrobus line is 1026. This value indicates that total chargers installed along the line should charge 1026 vehicles per day. A bus with a 600-kWh battery capacity will charge between 3 and 6 hours as average. When a vehicle's charging time is assumed to be approximately 4 hours, a charger can charge 6 battery packs in 24 hours. That means 1026 vehicle batteries can be recharged for approximately 24 hours of continuous operation by approximately 171 chargers. On the Metrobus line, there are five stations where buses can be parked for required charging time. Referred station numbers are 1, 8, 19, 33 and 44. Therefore, chargers shall be in those 5 stops. However, it is not possible to install those number of chargers due to limited space in the stations located in city centre.

When the places that are suitable for charging stations are examined, it is not possible to place more than 50 chargers in total considering available bus parking lot. Based on these results, it is possible to charge a total of 300-350 buses in 24 hours. This is equal to approximately 30-35% of the total number of buses. With this assumption, the lines which are suitable for the operation of electric buses are shown in green in the column of daily vehicle / charge number in Table V. Lines that are not applicable for electrification are marked with red.

On the other hand, battery lifetime is also assessed. Maximum charge-discharge cycle of applied cells is assumed as 6000. Based on these values, battery lifetime of buses operating in each line is given in Table V. Battery lifetime which is less than 7 - 8 years is not effective compared to internal combustion engine in terms of TCO (Total Cost Ownership).

TABLE III
REQUIRED ENERGY VALUES FOR E-BUSES

Required energy content for 2 cycle on the longest route 34G				
Model	Average energy consumption	Required energy content	Unit	Selected energy content
Citaro	**239kWh/100km**	**496.69**	kWh	**600**
Capacity	**250kWh/100km**	**519.77**	kWh	**600**

TABLE IV
ENERGY CONSUMPTION VALUES FOR ONE CYCLE

Route	->	34	34A	34 AS	34 BZ	34 C	34 G	34 U	34 Z
Distance (km)	->	30	22	41.5	40	29	52	11	11.5
Energy consumption (kWh)	Citaro	**71.6**	**52.5**	**99.1**	**95.5**	**69.2**	**124.2**	**26.3**	**27.5**
Energy consumption (kWh)	Capacity	**75.0**	**55.0**	**103.7**	**100.0**	**72.5**	**129.9**	**27.5**	**28.7**

TABLE V
NUMBER OF DAILY CHARGES PER LINE

Line Route	Number of daily bus trips	Trips per bus	Number of daily charges	Total bus/charge number	Battery EOL (years)	Feasibility for e-Bus	Required Charger
34	1296	14	**2.03**	**187**	**8**	+	**187**
34A	88	4	**0.42**	**9**	**39**	+	**9**
34 AS	1188	12	**2.37**	**237**	**7**	-	-
34 BZ	1798	14	**2.70**	**346**	**6**	-	-
34 C	872	12	**1.74**	**122**	**9**	+	**122**
34 G	75	5	**1.25**	**19**	**13**	+	**19**
34 U	110	3	**0.15**	**6**	**110**	+	**6**
34 Z	1827	61	**3.37**	**101**	**5**	-	-
Total	N/A	N/A	N/A	**1026**	N/A	N/A	**343**

According to that assumption, green lines in the Battery EOL (End of Life) column in Table V are compatible with electrification and the red marked lines are not feasible. When both columns (Total bus/charge number and Battery EOL) are examined together, it is seen that 5 lines (34, 34A, 34C, 34G, 34U) are suitable for electrical conversion of transportation.

IV. CONCLUSION

Today, demand for electric vehicles is limited by the introduction of some parameters. In this context, the cost of batteries is fundamental, especially in commercial vehicles that are constantly in use. With the decrease in battery costs in the following years, demand for electric vehicles is expected to increase.

When the results obtained in this study are reviewed, operating time (distance) is very important especially in electric bus applications. Electric bus is not advantageous in terms of TCO value, since operating distance is above a certain value, especially as the battery life ends very quickly.

As a result, obtained values in the study are considered and it is not possible to completely electrify the Metrobus line. However, in order to reduce emission values, it is reasonable to convert some routes to electric buses.

For future studies, the feasibility study shall be performed in order to re-charge the batteries on all buses. Initially, the whole transportation system should be designed so that the operation of the electric buses can be carried out. As an example, the charging station network infrastructure should be installed and the parking spaces where buses can wait while charging should be considered.

Taking everything into account, the problem could be focus on optimization techniques and linear programming to determine the electric buses recharging scheduling for a transportation network in Istanbul/TURKEY.

REFERENCES

[1] Yilmaz, C. (2018). *Economic Evaluation of Urban Electric Bus Charge Stations: Case of Eindhoven, The Netherlands.* MSc Thesis, Istanbul Technical University, Graduate School of Natural and Applied Sciences, Istanbul.

[2] Alves, B. B., Sethi, K., Dodero, A. L., Guerrero, A. H., Puga, D., Yeghyaian, E., Bose, R. (2019). *Green Your Bus Ride: Clean Buses in Latin America* (No. 133929).

[3] "Maria XYLIA, Towards electrified public bus transport: The case of Stockholm Doctoral thesis, KTH Royal Institute of Technology Industrial Engineering and Management Department of Energy Technology Energy and Climate Studies, Stockholm, Sweden, 2018."

[4] Göhlich, D., Kunith, A., & Ly, T. (2014). Technology assessment of an electric urban bus system for Berlin. *WIT Trans. Built Environ*, *138*, 137-149.

[5] Lajunen, A., & Lipman, T. (2016). Lifecycle cost assessment and carbon dioxide emissions of diesel, natural gas, hybrid electric, fuel cell hybrid and electric transit buses. *Energy*, *106*, 329-342.

[6] Teoh, L.E., Khoo, H.L., Goh, S.Y., Chong, L.M., (2018). Scenario-based electric bus operation: A case study of Putrajaya, Malaysia. Int. J. Transp. Sci. Technol, 7, pp. 10-25.

[7] Houbbadi, A., Pelissier, S., Trigui, R., Redondo-Iglesias, E., & Bouton, T. (2019, May). Overview of Electric Buses deployment and its challenges related to the charging-the case study of TRANSDEV.

[8] De-Leon, S., E-Bus Battery Market 2019. https://www.emove360.com/wp-content/uploads/2019/10/E-Bus-Battery-Market-2019.pdf, date of access: 24.12.2019

[9] Mahmoud, M., Garnett, R., Ferguson, M., & Kanaroglou, P. (2016). Electric buses: A review of alternative powertrains. *Renewable and Sustainable Energy Reviews*, *62*, 673-684.

[10] https://zeeus.eu/uploads/publications/documents/zeeus-ebus-report-2.pdf, date of access: 11.11.2019

[11] EVTrader, https://evtrader.com/c/electric-bus-manufacturers/, date of access: 24.12.2019

[12] Göhlich, D., Fay, T. A., Jefferies, D., Lauth, E., Kunith, A., & Zhang, X. (2018). Design of urban electric bus systems. Design Science, 4.

[13] UNECE TRANS/WP.29/1045 - Special Resolution No. 1

[14] https://www.iett.istanbul/tr/main/pages/tarihce/2, date of access: 22.12.2019

[15] https://www.iett.istanbul/tr/main/hatlar/, date of access: 22.12.2019

Turgay Gucukoglu was born in 1988 in Kahramanmaras/Turkey. He received his BSc in Electrical Engineering from Yildiz Technical University (YTU), Turkey in 2011. Then, he completed his MSc in Control and Automation Engineering at Yildiz Technical University in 2019.He is currently holding position of Senior Battery Development Engineer in the field of Battery Systems at AVL R&D Company, Turkey. He has published 1 paper about battery systems for electric & hybrid electric vehicles.

Haluk Sarı was born in 1988 in Kırklareli/TURKEY. He graduated as an Automotive Engineer from Ruse "Angel Kanchev" University, Bulgaria in 2012. He has 6 year-experience in field of xEV Powertrain and Battery Systems. He is currently holding position of Battery Development Engineer at AVL R&D Company, Turkey.

Koray ERHAN was born in 1987 in Turkey. He received his B.Sc. in Electrical Engineering from Yildiz Technical University, Turkey in 2010. Then he completed his MSc in Electrical Engineering at Istanbul Technical University in 2013. Finally, he got his PhD at Department of Energy Systems Engineering, Kocaeli University in 2018. He became a research assistant in 2010 at Istanbul Technical University and in 2013 at Kocaeli University. He has published more than 30 papers in different subjects including electric & hybrid electric vehicles photovoltaic power generation systems, renewable energy sources, energy storage technologies, and smart grid integration and automation systems. He has been a referee in SCI and other indexed journals. He is currently holding position of Battery Development Engineer at AVL R&D Company, Turkey.

Modeling and Performance Evaluation of an Electromagnetic Voltage Regulator via Series Compensation

Vinícius Henrique Farias Brito, José Carlos de Oliveira, Fabricio Parra Santilio

Abstract— **Although there currently exists a wide range of voltage regulators that are commercially available, the search for devices with a simpler physical design remains the focus of research studies. Following this line, an electromagnetic voltage regulator (EVR) arrangement has been proposed. The EVR is constituted of an autotransformer that supplies, via discrete taps, a series transformer that injects voltage for regulating the feeder voltage. Even though its operating principle is shown as being similar to that of other devices on the market, the physical arrangement and operating strategy of EVR show novelties which result in properties such as: economic attractiveness, constructive simplicity, and operational reliability. Moreover, when installing voltage regulators, efficacy studies must be carried out to optimize equipment design. In this context, this paper aims at evaluating the factors that influence the effectiveness of the EVR in restoring voltage variations according to the determinations imposed by regulatory agencies. The ultimate goal of this study is to determine the voltage deviation range that the EVR is able to restore. To achieve this goal, a mathematical modeling of the EVR is given and study cases are computationally carried out to investigate its performance when connected to a typical distribution feeder.**

Index Terms—**Computational Modelling, Distribution System, Electromagnetic Voltage Regulator, Performance Evaluation, Power Quality, Voltage Regulation.**

I. INTRODUCTION

AMONG the electrical power supply requirements imposed on power utilities, power quality indices are included, such as long-duration and short-duration voltage variations, harmonic distortions, unbalances, etc. In this scenario, the issues related to the voltage magnitude variations at power frequency are particularly highlighted, since distinguished normative documents establish limits for these phenomena in terms of long and short duration [1].

In Brazil, the definitions of voltage variation severity and duration are set by the Brazilian Electricity Regulatory Agency (ANEEL) in the technical standard titled Electricity Distribution Procedures in the National Electric System (PRODIST) - Module 8 [2]. This document classifies long-duration voltage variations as changes in the RMS value of the voltage over a period longer than 3 minutes. On the other hand, short-duration phenomena include those voltage variations manifested for periods shorter than the 3-minute limit. Moreover, the directive also establishes the magnitude limits for long and short duration voltage variation events.

When the voltage magnitude infringes the established limits, regulation or compensation processes are carried out in order to regulate the voltages to the acceptable levels defined by legislation. A wide range of equipment is currently employed to perform this task. In general, it is recognized that compensation devices are based on two basic strategies. The first comprises of voltage compensation by indirect methods, such as voltage control via static or dynamic devices associated with the control of reactive power flow. The second performs its function by acting directly on the voltage magnitudes using devices that change the voltage values via tap changers or direct injections of compensating voltage [3].

In the context of devices based on the control of reactive power, the simplest devices are capacitor and reactor banks – fixed or automatic [4]. Another possibility, widely used in the past in large power systems, is the synchronous compensator [5]. Further still, with the evolution of electronic switching technologies, commercial products that make use of the well-known FACTS technology have arisen [6]. This group includes the Static Var Compensators (SVCs) and Synchronous Static Compensators (STATCOMs).

Regarding compensation technology which acts directly on voltage magnitudes, traditional transformers with on-load tap changer (OLTC) and no-load tap changer (NLTC) [7] stand out, as well as other electromagnetic regulators based on tap changes to adjust the electrical quantities, such as the Step Voltage Regulator (SVR) [8]. Additionally, other devices, based on electronic switching, are available on the market. This is, for example, the case of the Dynamic Voltage Regulator (DVR) [9].

In light of the above, one recognizes, therefore, that there is a diversity of devices available on the market with operating properties capable of regulating the voltage at the load in

---

This study was financed by the Coordenação de Aperfeiçoamento de Pessoal de Nível Superior – Brazil (CAPES) – Finance Code 001.

Vinícius Henrique Farias Brito and José Carlos de Oliveira are with the Faculty of Electrical Engineering, Federal University of Uberlandia, Uberlandia, Brazil (e-mail: vinicius.brito@ufu.br; jcoliveira@ufu.br).

Fabricio Parra Santilio is with the Electrical Engineering Department, Federal University of Mato Grosso, Cuiaba, Brazil. (e-mail: fabricio.qee@gmail.com.br).

accordance with the required standards. However, the most widely used strategy to mitigate long-duration voltage variations, in distribution systems, is the direct compensation of the voltage magnitude [10].

Furthermore, in terms of the voltage regulators based on the direct compensation of the voltage magnitudes mentioned previously, there exists in this same category a device proposed in [11], which is called the electromagnetic voltage regulator (EVR). This device consists of a shunt autotransformer with taps supplying a transformer connected in series with the electrical feeder focused on the regulation process. The series transformer is responsible for the injection of a controlled reinforcement voltage, being that additive or subtractive, which aims at compensating the voltage at the load terminals. The fundaments that govern this proposal are found in [12], which shows that, via discrete switching, different taps of the autotransformer can be used to make the reinforcement voltage compatible with the required compensation level. The possibility of disconnecting the shunt autotransformer, as well as the switches, provides greater operational reliability for the network to which the EVR is connected. That is, in the event of a failure or maintenance of the regulator, despite the loss of the regulation process, the power flow between the source and the load is not interrupted.

In line with the aforementioned topological proposition, more recent works, such as [10] and [13], covering similar physical structures and commercial products have shown the feasibility of the arrangement focused upon in this paper. In fact, with a topology similar to the EVR, [14] describes a new conception for a voltage compensator, which was installed on a rural medium voltage feeder in Germany with high presence of distributed generation. The commercial equipment was called the line voltage regulator (LVR) and the results of its performance indicated great improvements in the voltage profiles of the rural medium voltage feeder. In addition to the operational effectiveness, the work highlights that the LVR presented a cost-benefit ratio higher than other options for voltage compensation, which significantly increased the network distributed generation capacity. Within the same constructive and operational strategy, [15] showed that the solution proved to be efficient for different voltage levels.

Even though the efficacy of the EVR injection has been verified for a constant load consumption [11] [12], its effectiveness for a load with dynamic behavior must be further investigated. In fact, variables such as the long-duration voltage variation magnitudes, the feeder and load parameters, and the available taps of the EVR are features that will strongly affect the performance of the device.

In this context, this paper aims at evaluating the relationship among these influencing factors since they define the range of voltage variations that the EVR can restore to the adequate voltage level set in the standards.

For a better understanding, initially, the physical arrangement and operating principle of EVR are presented, as well as the development of its mathematical modeling in the frequency domain. In the following, a detailed performance evaluation study and computational case studies are carried out to achieve the goal proposed in this paper.

II. ELECTROMAGNETIC VOLTAGE REGULATOR: PHYSICAL ARRANGEMENT AND MATHEMATICAL MODELING

Before deriving the mathematical model of the EVR, its physical arrangement is shown in the schematic diagram given in Fig. 1. It can be noted that the device enables the control of the load voltage (Bus 2) by injecting a series compensation voltage (additive or subtractive reinforcement), which, when summed to the supply voltage, leads to a controlled voltage at the load terminals.

In Fig. 1, the regulator is operating to restore the load voltage (Bus 2) when an undervoltage occurs on Bus 1. Once this phenomenon happens, the control on the regulator detects it and selects the tap of the autotransformer that offers the most adequate level of compensating voltage for injection into the system. This compensation voltage when summed to the supply voltage restores the voltage at Bus 2 to its required value or close to it. Subtractive voltages are also feasible for injection by the series transformer, in the case of overvoltages. This can be carried out by changing the contacts using the SWpp and SWpn switches.

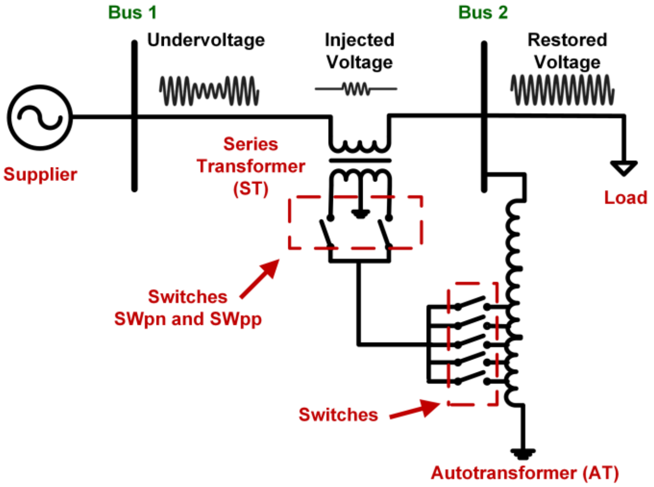

Fig. 1. Schematic diagram of the Electromagnetic Voltage Regulator. Adapted from [11].

The equivalent electrical circuit of the EVR and overall system arrangement, related to a specific steady state operational condition, is given in Fig. 2. Noteworthy here is that the equivalent circuit shown is applicable to a given selected tap when operating to restore undervoltages.

The corresponding equation to establish the relationship among the system (EVR, load, and feeder) parameters and the load voltage is given by (1). Noted also is that the magnetizing branches of the transformers are disregarded. The variables in (1) are identified in (2) to (5).

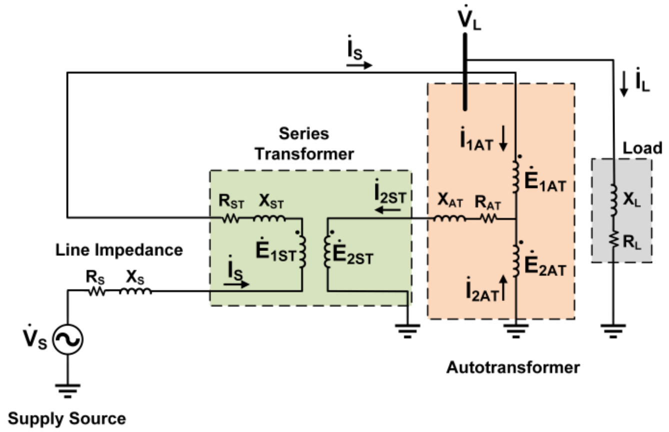

Fig. 2. Equivalent electrical circuit of the EVR, feeder and load.

$$\dot{V}_L = \frac{\dot{V}_S}{1 - \frac{\alpha_{ST}}{\alpha_{AT}} + \dot{K}_1 + \dot{K}_2} \tag{1}$$

$$\dot{K}_1 = \left(\frac{\alpha_{ST}^2 . \alpha_{AT}}{\alpha_{AT} - \alpha_{ST}} \right) * \frac{\dot{Z}_{AT}}{\dot{Z}_L} \tag{2}$$

$$\dot{K}_2 = \left(\frac{\alpha_{AT}}{\alpha_{AT} - \alpha_{ST}} \right) * \frac{\left(\dot{Z}_{ST} + \dot{Z}_S \right)}{\dot{Z}_L} \tag{3}$$

$$\alpha_{AT} = \frac{E_{1AT} + E_{2AT}}{E_{2AT}} \tag{4}$$

$$\alpha_{ST} = \frac{E_{1ST}}{E_{2ST}} \tag{5}$$

where:

- $\dot{V}_S$ is the supply voltage.
- $\dot{V}_L$ is the voltage at the load terminals.
- α_{AT} is the transformation ratio of the autotransformer.
- α_{ST} is the transformation ratio of the series transformer.
- $\dot{Z}_S$ is the supply network short-circuit impedance.
- $\dot{Z}_{ST}$ is the total impedance of the series transformer referred to the primary side.
- $\dot{Z}_{AT}$ is the total impedance of the autotransformer referred to the secondary side.
- $\dot{E}_{1ST}$ and $\dot{E}_{2ST}$ are the voltages on the primary and secondary sides of the series transformer, respectively.
- $\dot{E}_{1AT}$ and $\dot{E}_{2AT}$ are the voltages on the primary and secondary sides of the autotransformer, respectively.

III. A CASE STUDY OF THE EVR PERFORMANCE

In order to carry out the performance investigation of the overall system arrangement and the EVR effectiveness during the occurrence of voltages deviations from the standard values, a typical electrical system has been utilized. It consists of a radial feeder, whose parameters are found in Table I. It is noteworthy that, without the action of the regulator, the connection of the rated load to the feeder leads to a voltage drop of about 3.5% at the series impedance, assuming the supply voltage is 1 pu.

TABLE I
FEEDER AND LOAD CHARACTERISTICS

Parameter	Value
Rated Voltage	13.8 kV
Network Short Circuit Power	200 MVA
R/X ratio	0.5
Load Power Factor	0.94 (lag)
Rated Load Power	10 MVA

As for the EVR, the compensator is connected to the feeder, in accordance with the electrical circuit of Fig. 2. Its regulation range (Reg. Range) goes up to ± 20% in steps of 2.5%. The autotransformer has 8 taps, therefore, the EVR, via its tap 8, is capable of providing a maximum line voltage of:

$$\begin{aligned} V_{1ST} &= \mathrm{Re}g.\ Range(pu) * V_{RATED} \\ V_{1ST} &= 0.2 * 13.8kV = 2.76kV \end{aligned} \tag{6}$$

In order to reduce the current level of the switches of the taps, the transformation ratio of the series transformer was chosen as $\alpha_{TS} = 0.5$. One is reminded that under this condition, the current on the primary side of the series transformer will be 50% of the feeder (load) current. Therefore, due to this transformation ratio of the series transformer, the voltage on the secondary side of the autotransformer must be twice the voltage value intended for injection. Taking tap 8 as an example, to achieve a compensating voltage of 20%, it is necessary that the voltage on the secondary side of the autotransformer be 40% of the feeder rated voltage. Similar reasoning applies to the other taps.

Regarding the rated power of the transformers, both autotransformer and series transformer have the same rated power, as determined by (7).

$$\begin{aligned} S_{ST} = S_{AT} &= \left(\frac{\mathrm{Re}g\ Range(pu)}{1 - \mathrm{Re}g\ Range(pu)} \right) * S_{LOAD} \\ S_{ST} = S_{AT} &= 2.5MVA \end{aligned} \tag{7}$$

where:

- S_{ST} is the rated power of the series transformer.
- S_{AT} is the rated power of the autotransformer.
- S_{LOAD} is the rated load power.

Table II provides the characteristics of the two electromagnetic units that make up the EVR. The impedances and resistances are in line with typical designs.

TABLE II
SERIES TRANSFORMER AND AUTOTRANSFORMER CHARACTERISTICS

Data	**Power (MVA)**	**Primary/Secondary Winding Voltages**	**Zcc (%)**	**Rcc (%)**
Series Transformer	2.5	2.76/5.52 kV	5	1
Autotransformer	2.5	13.8 kV/Taps	5	1
Autotransformer taps – Secondary Winding Voltage		5.52 kV (Tap 8) – 4.83 kV (Tap 7) 4.14 kV (Tap 6) – 3.45 kV (Tap 5) 2.76 kV (Tap 4) – 2.07 kV (Tap 3) 1.38 kV (Tap 2) – 0.69 kV (Tap 1)		

Once the feeder, the load, and the design characteristics of the regulator are defined, the premises for the studies are listed as follow:

- The studies performed are associated with phenomena classified as long-duration voltage variations.
- According to the criteria defined in [2], the voltage values between 0.93 pu and 1.05 pu are considered as adequate. This voltage range is delimited by the green region of Fig. 3.
- When the limits of this range are violated, the action of the voltage regulator is represented, for each tap of the autotransformer, by lines that are changed according to the tap used.

Fig. 3 shows, initially, that the supply network suffers a 0.15 pu voltage drop. Then, with the load disconnected, the load voltage reaches the value of 0.85 pu. Once such a voltage variation is detected by the equipment control, the EVR starts to operate using tap 4 of the autotransformer – the corresponding reinforcement voltage is 2.76 kV, therefore, $\alpha_{AT\text{-}TAP4}$ is equal to 5, as shown in (8). Thus, still in the condition of the disconnected load, (9) shows that the load voltage increases to 0.94 pu. This value is obtained by (1) when K_1 and K_2 are equal to zero, as such; it corresponds to the maximum compensation achieved by tap 4.

$$\alpha_{AT-TAP4} = \frac{13.8kV}{2.76kV} = 5 \tag{8}$$

$$\dot{V}_L = \frac{\dot{V}_S}{1-\frac{\alpha_{ST}}{\alpha_{AT-TAP4}}} = \frac{0.85}{1-\frac{0.5}{5}} = 0.94pu \tag{9}$$

where:

$\alpha_{AT-TAP4}$ is the transformation ratio of the autotransformer when tap 4 is selected.

Therefore, under the above-mentioned conditions, tap 4 was sufficient for restoring the voltage to the appropriate range. However, as the load is connected and its power increases the complex coefficients K_1 and K_2 change, and despite the injection of the voltage from tap 4 being maintained, as expected, the load voltage gradually decreases; the decay rate is defined by the feeder and series transformer impedances. Fig. 3 shows that, starting from a 3 MVA load, tap 4 is no longer sufficient to adjust the load voltage to the adequate range. Then, the control changes to tap 5, and a new line starts in Fig. 3, with a similar decay behavior, however, starting with an adequate voltage value. When the load becomes equal to 7.9 MVA, the situation repeats once more.

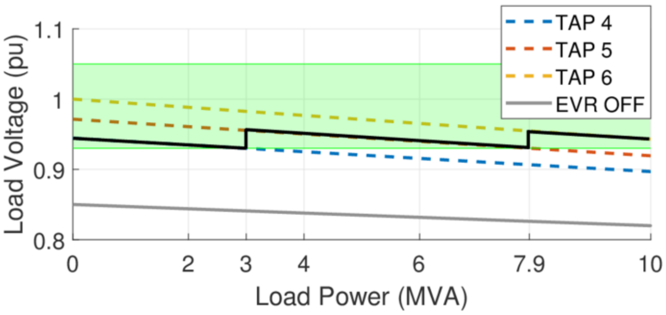

Fig. 3. Correlation between the load voltage and the load power for an undervoltage of 0.85 pu.

The results of the performance studies carried out so far reveal that the voltage compensation efficacy decreases with the increase of the load power, for each tap, as expected. Therefore, in order to maintain the load voltage within the adequate range, it becomes necessary to change the tap to compensate for the loss of regulation efficiency caused by the increase in the K_1 and K_2 coefficients, according to (1).

Moreover, the dynamics of the control and switching system will define the regulator response time for the voltage regulation.

From another evaluative aspect, performance studies are now carried out for a constant 10 MVA load under different undervoltages that occurred on the network. In doing so, the behavior of the set source-feeder-EVR-load is considered for various undervoltage magnitudes, and the effectiveness of the voltage regulation is evaluated for the 8 taps, as shown in Fig. 4.

Fig. 4 shows that under different undervoltages, as the taps of the autotransformer change from 1 to 8 (increasing the reinforcement voltage), the load voltage also rises as desired. The graph shows that each tap determines an undervoltage limit for which the EVR is able to ensure that the load voltage is within the adequate range. Consequently, the most critical undervoltage magnitude that the EVR is effective in restoring is set by tap 8. The figure indicates that for a 10 MVA load the regulator is capable of compensating, for the adequate range, undervoltage magnitudes up to 0.8 pu at the supply voltage.

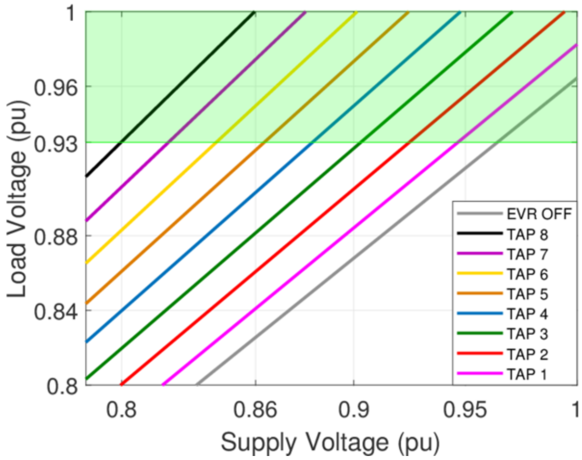

Fig. 4. Undervoltage magnitudes compensated by the EVR according to the autotransformer tap for a 10 MVA load.

IV. Dynamic Relationship Between Undervoltages Phenomena and the EVR Effectiveness

In addition to the studies related to the previously presented operational limits, this section aims at showing the dynamic performance of the EVR under specific operating conditions. Hence, the system used as a case study was implemented in the MATLAB Simulink, as shown in Fig. 5. The parameters of the system are the same as those shown in Tables I and II.

The two operational situations considered are the following:

- Case 01: Initially, the 13.8 kV voltage supply (1 pu) feeds the rated load (10 MVA). At t = 0.5 s, the supply voltage drops to 11.73 kV (0.85 pu). Then, the EVR is set to turn on at t = 1 s with tap 8 selected.
- Case 02: This situation is similar to the previous one, except for the fact that the voltage drop is more severe (10.35 kV or 0.75 pu).

A. *Case 01 - Undervoltage of 0.85 pu*

Fig. 6 presents the voltage profile at the load terminals. It is shown that, between t = 0 and 0.5 s, the load voltage has a value of 13.25 kV (0.96 pu). The 0.04 pu voltage drop is due to the feeder impedance. At t = 0.5 s, the load voltage reduces to 11.27 kV (0.82 pu), due to the voltage variation imposed on the supplier. Next, at t = 1 s the regulator starts operating, with the autotransformer switched to tap 8. Under these conditions, the load voltage is restored to 13.69 kV (0.99 pu), thus showing the effectiveness of the regulator.

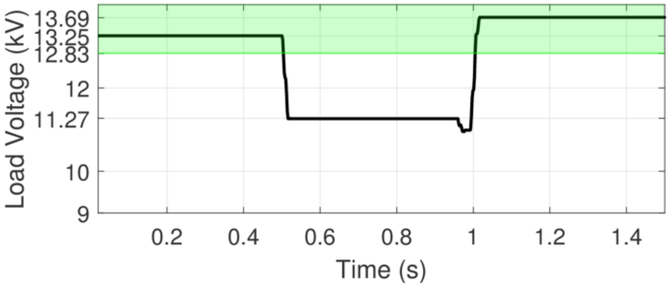

Fig. 6. Load voltage profile for Case 01.

B. *Case 02 - Undervoltage of 0.75 pu*

The results associated with a more drastic undervoltage are indicated in Fig. 7. As one notes, from 0 to 0.5 s the load voltage remains at 13.25 kV (0.96 pu) and, then, the load voltage is suddenly reduced to 9.94 kV (0.72 pu). After the regulator insertion, at t = 1 s, with the autotransformer switched to tap 8, the load voltage is increased to 12.08 kV (0.87 pu). Therefore, for this situation, the EVR does not have sufficient characteristics to restore the load voltage to the adequate range. In fact, the specified regulator is capable of restoring undervoltages up to 0.80 pu for a 10 MVA load. Despite the demonstrated limitation, the load voltage increased from 0.72 pu to 0.87 pu, which lessens the voltage variation at the load bus.

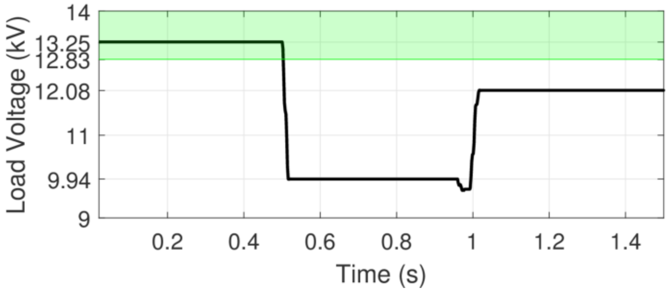

Fig. 7. Load voltage profile for Case 02.

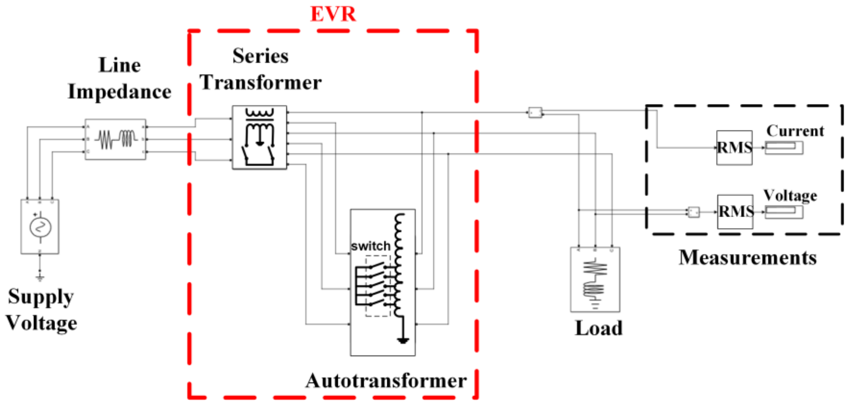

Fig. 5. System implemented in the MATLAB Simulink.

The main electrical quantities associated with the operating conditions of the EVR, for the two cases analyzed, are summarized in Table III. Comparing those to the rated currents of the series transformer (105 A) and the autotransformer (523 A), the values obtained are within the rated characteristics of these electromagnetic components. The same applies to the voltage on the primary side of the series transformer.

TABLE III
CURRENTS AND VOLTAGES ASSOCIATED WITH THE STUDIED CASES

Electrical Quantity	**Case 01**	**Case 02**
I_L	415.1 A	366.2 A
I_S	518.9 A	457.8 A
I_{1AT}	103.8 A	91.6 A
V_{1ST}	2.61 kV	2.3 kV

Finally, Fig. 8 highlights the EVR performance for other load power values, previously fixed at 10 MVA. The figure shows the undervoltage magnitudes that the regulator is capable of restoring to the adequate range at the load bus. As expected, as the load power is reduced, the EVR can restore more severe undervoltage magnitudes.

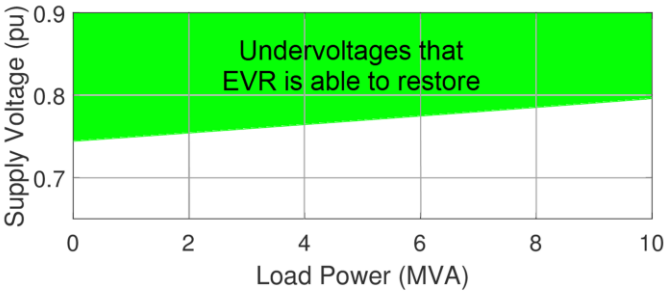

Fig. 8. Undervoltage magnitudes compensated by the EVR for the adequate range according to load power.

V. CONCLUSIONS

This paper presented an electromagnetic device for compensating voltage variations. The proposal acts directly on the load voltage by inserting a reinforcement – additive or subtractive – to restore the voltage magnitude to the standards established by legislation. The device has an attractive operating strategy given the use of components that offer constructive and operational simplicity, reliability, attractive costs, versatility of installation in uncontrolled environments, among other attributes. In order to contextualize the theme, general information concerning the physical arrangement and mathematical modeling of the regulation process was synthesized. As exposed in the introduction, the EVR was initially proposed by [11] and a similar device was materialized as a commercial product by [14] [15]. Once the device physical and mathematical model were presented, studies related to the effectiveness of the device when faced with typical influence quantities of electrical networks were carried out. The results clearly showed that the EVR, in the terms designed and defined by its basic characteristics, also presents a strong dependence on the feeder and load parameters. Its efficacy may be full, partial or insufficient, depending on the variables involved in the voltage regulation process. In general, the results obtained are encouraging for the diffusion of the technology contemplated herein. Regarding the discrete response and the use of the EVR for restoring short-duration voltage variations, it can be implemented with fine-tunes based on the use, for example, of electronic techniques for controlling switches continuously, which is a subject for future works. Finally, it should be noted that, although the study presented has explored phenomena associated with undervoltages in the supply network, the regulator can also be used when overvoltages occur on the network.

REFERENCES

[1] M. H. Bollen, *Understanding Power Quality Problems: Voltage Sags and Interruptions*. Punta Gorda: Wiley-IEEE Press, 1999.

[2] ANEEL, “Procedimentos de Distribuição de Energia Elétrica no Sistema Elétrico Nacional - PRODIST - Módulo 8,” 2018.

[3] T. V. Da Silva, “Uma proposta para o controle eletrônico de reguladores eletromagnéticos através do reforço série de tensão,” M.S. thesis, Universidade Federal de Uberlândia, 2012.

[4] S. Haffner, L. A. Pereira, L. V. Gasperin, and L. Barreto, “Alocação de bancos de capacitores em redes de distribuição de energia visando eliminar violações de tensão,” *Control. Automação*, vol. 20, no. 4, pp. 546–563, 2009.

[5] F. O. Igbinovia, G. Fandi, Z. Muller, J. Svec, and J. Tlusty, “Optimal location of the synchronous condenser in electric-power system networks,” *Proc. - 2016 17th Int. Sci. Conf. Electr. Power Eng. (EPE)*, 2016.

[6] K. R. Padiyar, *FACTS controllers in power transmission and distribution*. New Delhi: New age International (P) Limited, Publishers, 2007.

[7] H. Zhou, X. Yan, and G. Liu, “A review on voltage control using on-load voltage transformer for the power grid,” *IOP Conf. Ser. Earth Environ. Sci.*, vol. 252, no. 3, 2019.

[8] L. A. Kojovic, “Modern techniques to study voltage regulator - DG interactions in distribution systems,” *2008 IEEE/PES Transm. Distrib. Conf. Expo.*, pp. 1–6, 2008.

[9] S. A. Taher, H. T. Fard, and E. B. Kashani, “New switching approach for DVR using one cycle control method,” *Ain Shams Eng. J.*, vol. 9, no. 4, pp. 2227–2254, 2018.

[10] P. R. P. Sarathy, “Analysis and optimization of medium voltage – line voltage regulator,” M.S. thesis, Norwegian University of Science and Technology Department, 2018.

[11] F. P. Santilio, “Proposta, modelagem e validação de uma nova concepção de regulador eletromagnético através do reforço série de tensão,” Ph.D. dissertation, Universidade Federal de Uberlândia, 2013.

[12] L. E. Vasconcelos, “Modelagem no domínio da frequência de um regulador eletromagnético de tensão baseado na compensação série,” M.S. thesis, Universidade Federal de Uberlândia, 2014.

[13] G. Ram, V. Prasanth, P. Bauer, and E. M. Barthlein, “Comparative analysis of on-load tap changing (OLTC) transformer topologies,” *2014 16th Int. Power Electron. Motion Control Conf. Expo.*, pp. 918–923, 2014.

[14] M. Carlen *et al.*, “Line voltage regulator for voltage adjustment in MV-Grids,” *CIRED 23rd Int. Conf. Electr. Distrib.*, 2015.

[15] G. Leci and F. Cornelius, “Increasing grid capacity to connect renewable energies,” *CIGRE*, pp. 1–9, 2016.

An Ingenious Application-Specific Quality Assessment Methods for Compressed Wireless Capsule Endoscopy Images

Kinde Anlay Fante, Fetulhak Abdurahman and Mulugeta Tegegn Gemeda
Faculty of Electrical and Computer Engineering, Jimma Institute of Technology, Jimma University, Ethiopia

Abstract—**Image quality assessment methods are used in different image processing applications. Among them, image compression and image super-resolution can be mentioned in wireless capsule endoscopy (WCE) applications. The existing image compression algorithms for WCE employ the general-purpose image quality assessment (IQA) methods to evaluate the quality of the compressed image. Due to the specific nature of the images captured by WCE, the general-purpose IQA methods are not optimal and give less correlated results to that of subjective IQA (visual perception). This paper presents improved image quality assessment techniques for wireless capsule endoscopy applications. The proposed objective IQA methods are obtained by modifying the existing full-reference image quality assessment techniques. The modification is done by excluding the non-informative regions, in endoscopic images, in the computation of IQA metrics. The experimental results demonstrate that the proposed IQA method gives an improved peak signal-to-noise ratio (PSNR) and structural similarity index (SSIM). The proposed image quality assessment methods are more reliable for compressed endoscopic capsule images.**

Index Terms—**Image quality assessment, wireless capsule endoscope, compressed images, image compression.**

I. INTRODUCTION

Wireless capsule endoscopy (WCE) is a tablet size camera with a radio frequency transmitter which can be easily ingested by patients to diagnose gastrointestinal abnormalities [1]. It enables the non-invasive imaging of the gastrointestinal tract with a high-resolution camera operating in the visible electromagnetic spectrum. The capsule captures the image of the inner wall of the human digestive system and transmits it to a data recorder located outside the patient's body. The transmission of high-resolution images via a wireless link consumes high power and requires a high transmission bandwidth [2]. In order to reduce the power consumption and transmission bandwidth, image compression algorithms are included inside the capsule [3]. Image processing software on workstation is used to decompress and process the received images in order to improve the visual quality. Among the image processing methods, super-resolution algorithms [4] are proposed to improve the spatial resolution of the images, image post-processing and error-correcting codes are proposed to suppress the distortion due to transmission channel noise [5], and computer-aided diagnosis systems [6] are used to improve the detection of abnormalities during the evaluation phase.

Generally, high quality images are required for accurate diagnosis of abnormalities. Ideally, lossless image compression methods are needed to retain all information in medical images. However, the lossless image compression algorithms achieve a low compression rate. It cannot significantly reduce the power consumption and the bandwidth requirement of the WCE transmission system. Hence, lossy image compression algorithms are preferred to achieve a high compression rate. The amount of information loss due to the compression process should not affect the diagnosis outcome [7]. On the other hand, image compression algorithms that have high information loss achieve a high compression rate. A good compromise between the image quality and compression rate needs to be maintained in this particular application.

In order to design an image compression algorithm that can achieve a high compression ratio without affecting the diagnosis accuracy, we need reliable image quality assessment methods. Such methods can help us to optimize the parameters of the image compression algorithms, such as quantizer values and sub-sampling factors [2]. The image quality assessment methods can be categorized into two groups: the subjective and objective quality assessment methods [8]. The subjective quality assessment method is more accurate, time-consuming, and expensive. Hence, the objective image quality assessment methods are widely used in practice. The objective image quality assessment methods are widely used to quantify the quality of medical images in compression algorithms [2], [3]. Among the popular methods, the peak signal-to-noise ratio (PSNR) [9], structure similarity index (SSIM) [10], and feature similarity index (FSIM) [11] were employed to evaluate the distortion introduced due to the quantization operation of the endoscopic image compression algorithms. In literature, a minimum peak signal-to-noise ratio (PSNR) value of 30 dB has been considered to be sufficient for accurate diagnosis of pathology in endoscopic images [12]. However, in [7], [13], a PSNR value of 35 dB was considered as a threshold value for an accurate diagnosis of abnormalities using medical images. A reliable objective IQA method for WCE application will help to preserve the information needed for accurate diagnosis of abnormalities and optimize the parameters of image compression algorithms. Some of these IQA methods, for instance, PSNR and SSIM, give equal importance to all parts of the image in their evaluation of the image quality assessment metrics. However, the quality of all the parts of the image may not be equally important in some applications. For example, in an endoscopic capsule image, the four corners of the image are non-informative regions. The pixels in those regions are all zero. These regions have no important information, and the quality of the pixels in these regions is unaffected by the image compression algorithms. This makes the existing objective image quality assessment techniques less reliable for WCE application, and their correlation with the subjective assessment techniques is low. In this work, we present an improved objective image quality assessment methods that exclude the impact of the non-informative regions. The proposed ad-hoc algorithm improves the performance of general-purpose algorithms by incorporating knowledge about the nature of the images. The incorporated knowledge helps these algorithms to completely remove the impact of non-informative regions in the IQA metrics calculation.

The existing objective IQA methods can be classified into three categories based on the availability of reference images [14]. These are full reference, reduced reference, and non-reference IQA methods. The focus of this paper is on full reference IQA methods for compressed endoscopic capsule images. The full reference IQA methods can be further divided into two broad categories. The fist category uses statistical error metrics such as mean square error (MSE), PSNR, and visual signal-to-noise ratio (VSNR), etc. And the second category takes into account the knowledge of the human visual system (HVS), which includes FSIM, SSIM, Visual Information Fidelity (VIF), etc. These IQA metrics are general-purpose methods and may not be suitable for some applications. An example is an image taken using a capsule camera, as shown in Fig. 1. Due to the circular shape of the lens of the capsule camera and the rectangular shape of the image sensor arrays, the four corners of the WCE image are occluded from the illumination source. The corner regions of this image have no important information. and, all of its pixel values are zero. It also creates a sharp transition boundary between the corner regions and the circular visual region of the image. We can put forward the following two observations from the nature of endoscopic capsule images. First, the quality of the four corner regions of endoscopic images is unaffected by lossy image compression algorithms since all pixel values are zeros. This affects the statistical error based image quality metrics such as MSE and PSNR. Second, the sharp transition boundary between the corner regions (non-informative regions) and circular visual region of the endoscopic capsule image is highly affected by lossy image compression algorithms that involve sub-sampling and quantization such as DCT-based [15] and DWT-based [16] algorithms. Similarly, the quantization and subsampling operation in DPCM-based [17], [18], and error due to inadequate side information in distributed video coding algorithms [19]. However, this region has no significant information relevant to the diagnosis of abnormalities in the gastrointestinal tract. Most of the IQA methods that use the knowledge about the human visual system, such as FSIM, SSIM, VIF, etc., estimate the information content of image regions based on the variance of the image blocks. An image block that lies in the boundary between the non-informative regions and the circular visual region has a very high variance. The presence of this high variance region significantly affects the reliability of the IQA metrics for this particular domain of images.

Generally, we can use three types of knowledge in the design of image quality assessment methods. These are pieces of knowledge about the human visual system (HVS), statistics of the image, and the distortion type [14].

The previous works on this topic assessed the suitablity of the general-purpose image quality assessment methods for WCE application. Both subjective and objective image quality assessment methods were presented [20]–[22]. However, the objective image quality assessment methods for compressed WCE images [20] have not taken into consideration the peculiar nature of the WCE images. By using the knowledge about the WCE camera, we developed more reliable image quality assessment methods. In this work, we use the knowledge about the statistics of the image acquisition system to improve the performance of the general-purpose objective IQA methods for wireless capsule endoscopy applications. The contribution of this work is that it excludes non-informative regions in the computation of objective image quality assessment methods for WCE application. To the best of our knowledge, this the first work which takes into consideration the peculiar nature of WCE images in the image quality assessment method for WCE application. The remaining sections of the paper are organized as follows. Section II discusses the analysis of the proposed IQA method. In Section III, the result and discussions are given. Finally, the conclusion is given in Section IV.

II. ANALYSIS OF THE PROPOSED IMAGE QUALITY ASSESSMENT METHODS

The proposed IQA algorithm improves the performance of the general-purpose IQA methods by excluding the following two regions in the computation of the IQA metrics. These are: (1) the non-informative (corner) regions, and (2) the boundary between the corner regions and the circular visual region. This section will investigate the overall impact of excluding these two regions in the computation of general-purpose IQA metrics for WCE application. The block diagram of a full-reference image quality assessment method is depicted in Fig. 1. The image is compressed to reduce its size for storage or transmission. The lossy image compression process introduces distortion to the image. In both DPCM-based [2] and DCT-based [23] image compression algorithms, the chroma subsampling and quantization processes introduce distortion. The compressed image is then decompressed (decoded) for visualization. The amount of distortion in the decompressed is quantified using image quality assessment method. The image quality assessment method takes both the decoded image and the reference image to compute the objective image quality assessment metrics.

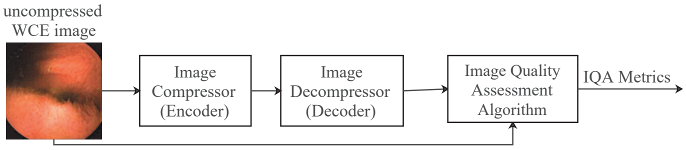

Fig. 1. Block diagram of a full-reference objective image quality assessment method for compressed WCE Images.

A. The Effect of Corner Regions

As shown in Fig. 2, the visual region of the capsule camera is the circular region. For the image of size $W \times W$, the area of the visual region is $\frac{\pi W^2}{4}$, and the area of the whole image is W^2. The total area of the non-informative regions, A_{ni}, is given by:

$$A_{ni} = W^2(1 - \frac{\pi}{4}) \tag{1}$$

For $W = 256$, $A_{ni} = 14064$ pixels. This is about 21.46 % of the total pixels of the image, which constitutes nearly 220, 8×8 patches. The total number of pixels in the non-informative region is more than one-fifth of the total numbers of pixels of the image, and the impact on the image quality assessment metrics must be considered. The exclusion of the pixels in the non-informative regions in the computation of image quality assessment metrics improves the reliability of the methods. Several image quality assessment methods were used to evaluate the performance of wireless capsule endoscopy image compression algorithms. Among them, mean squared error (MSE) and peak signal-to-noise ratio (PSNR) can be mentioned [2]. These methods give equal importance to all pixels in the image during the computation of quality assessment metrics. Hence, they are generally not correlated with subjective image quality assessment methods [25]. They are used because they are based on the energy of the error signal (difference in signal between the images being compared), which is preserved after linear unitary (orthogonal) transforms such as Discrete Cosine Transform (DCT). The MSE and PSNR are computed using the following equations [9].

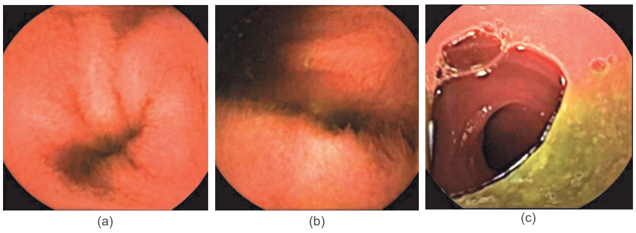
(a) (b) (c)

Fig. 2. Wireless capsule endoscopy images [24].

$$MSE = \frac{\sum_{i=1,j=1,k=1}^{M,N,3}(X_{i,j,k} - Y_{i,j,k})^2}{M \times N \times 3} \tag{2}$$

$$PSNR = 10log_{10}(\frac{255^2}{MSE}) \tag{3}$$

Where $X_{i,j,k}$ is the pixel value of the reference image, $Y_{i,j,k}$ is the pixel value of the decompressed image, M, N are sizes of the image, i, j are spatial coordinates of the image array and k is the index of the color components of a color image.

As described above, the pixel value error in the corner regions of an endoscopic image during the compression process is zero, but the number of pixels shown in equation (2) includes the corner pixels. This reduces the MSE and increases the PSNR which makes these methods less correlated with the subjective image quality assessment method. To alleviate this drawback, the modified versions of mean squared error (MSE_WCE) and peak signal-to-noise ratio ($PSNR\_WCE$) are given below.

$$MSE\_WCE = \frac{\sum_{i=0,j=0,k=0}^{M,N,2}(X_{i,j,k} - Y_{i,j,k})^2}{M \times N \times 3 - 3 \times N_c} \tag{4}$$

Where N_c represents the number of corner pixels.

$$PSNR\_WCE = 10log_{10}(\frac{255^2}{MSE\_WCE}) \tag{5}$$

The number of corner pixels, in equation (4), includes those pixels whose values are unaltered by the image decompression process. It should be noted that the corner pixel values which are near to the boundary between the circular visual region and corner regions are affected by the reconstruction process of the lossy image decompression algorithms.

Furthermore, the effect of the pixels in the corner regions on the objective image quality assessment methods can also be investigated using the structural similarity index (SSIM). It is given by the following equation [10].

$$S(X,Y) = \frac{(2\mu_x\mu_y + C_1)(2\delta_{xy} + C_2)}{(\mu_x^2 + \mu_y^2 + C_1)(\delta_x^2 + \delta_y^2 + C_2)} \tag{6}$$

Where μ_x, μ_y are the mean values, δ_x, δ_y are the unbiased standard deviations of the reference and distorted images respectively, and C_1, C_2 are constants. From equation (6), we can conclude that the presence of zero-value corner pixels reduces the mean values and increases the values of variances in both the reference and distorted images. Moreover, the corner regions have no structural units that can be affected by compression algorithms. Hence, the structures in the decompressed and original images are similar in the corner regions of endoscopic images. This tends to increase the SSIM value, which is misleading.

To eliminate the effect of the corner regions, the pixel values in the circular visual regions only are included in the computation of IQA metrics. We clip the corner regions and compute the metrics. Overall, the presence of corner regions in capsule endoscopic images increases both PSNR and SSIM values during the evaluation of the quality metrics of the image compression algorithms. Hence, the exclusion of the corner regions in the image quality assessment metrics computation of wireless capsule endoscopy images makes the metrics more reliable. This is due to the fact that non-informative regions are not affected by the image compression process, and it increases the image quality scores of the IQA methods.

B. The Effect of Boundary Region

Unlike natural image boundaries, the boundary between corner regions and the circular visual region has a sharp pixel value transition. Consequently, it contains large high-frequency components when a block-based transform image compression algorithm is applied. The high-frequency components are quantized using larger quantizer values in such algorithms. Hence, this region is highly distorted by image compression algorithms. The highest distortion occurs in this region in both DPCM-based image compression algorithms that employ sub-sampling [2] and transform coding (DCT and

DWT) methods [15], [16]. This is due to the fact that there is little correlation between the corner pixel values and those in the visual region.

The drawback of the existing objective image quality assessment methods for WCE is that both the PSNR and the SSIM values decrease as a result of the artificial boundary. This leads to unrealistic quality metrics value. Fig. 3 shows the scaled structural similarity map of the image given in Fig. 2(a). As we can see from the figure, the boundary between the corner regions and the circular visual region shows a very high difference. Unlike the rest of the region, the boundary region pixels are uncorrelated. This leads to significantly large high-frequency components in block-based transforms. Similarly, the uncorrelated nature of the pixels leads to a large error in subsampling based image compression algorithms. However, the distortion in this region has no effect on the quality of the visual perception of the image for of gastrointestinal abnormalities.

Fig. 3. The structural similarity map of the image shown in Fig. 2 (a).

Similar to the corner regions, the proposed solution in this work is the exclusion of the boundary region in the computation of IQA metrics. In this particular case, thread-like region whose width is 17 pixels (8 pixels into the corner region and 8 pixels into the visual region) perpendicular to the boundary is considered as a boundary region. The exclusion of the boundary region pixels helps us achieve reasonable image quality assessment metrics for WCE.

III. RESULTS AND DISCUSSIONS

The experimental setup, the results obtained from the experiments, and the analysis of the results are discussed in this section.

A. Experimental Setup

Extensive experiments were performed to compare the proposed IQA methods with general-purpose IQA methods. The experiments were designed and implemented by modifying the existing lossy image compression algorithms, which were proposed for WCE application. These image compression algorithms use DCT [15], DWT [16], and DPCM with subsampling [2] based image processing methods. The comparative analysis of the general-purpose and the proposed IQA methods was performed. The two selected IQA methods used in this work for demonstration purposes are PSNR and SSIM. These metrics are chosen here because they are widely used in the performance analysis of image compression algorithms for WCE. In addition to that, the two methods are good representatives of the two categories of objective IQA algorithms. PSNR is based on the statistical error, and SSIM is based on the HVS perception [26], [27]. The main goal of these experiments is to prove the concept in practical scenarios using comparative analysis. It is not to compare the performance of different image compression algorithms.

In order to evaluate the performance of the proposed IQA methods, 120 images from Gastrolab [24] were selected. The selected images are in RGB format with different resolutions. The images from this database were used in the performance evaluation of several image compression algorithms [2], [17].

B. Analysis of Results

The comparison of mean squared error (MSE) of the pixel values in the boundary region and those inside the visual area are shown in Fig. 4. As shown in the figure, the average MSE values of pixels in the boundary region are 54.82, and those of the pixel values inside the visual area are 3.55 for standard JPEG image compression algorithm with quantizer value of 1.5. This shows that the pixels around the boundary region are highly affected by the compression algorithms due to the lack of correlation of the pixel values in the two regions. This leads to IQA metrics, which has less correlation with the subjective image quality assessment method.

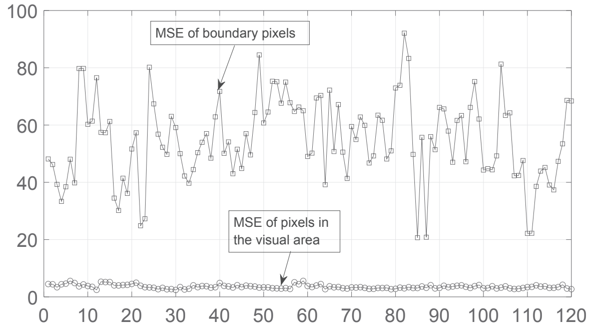

Fig. 4. The mean square error value of the pixels in the boundary and those in the visual region of 120 endoscopic images for standard JPEG image compression algorithm with a quantizer value of 1.5.

The performance of the proposed ad-hoc IQA methods are evaluated using the implementation of eight different image compression algorithms which were proposed for WCE application. Both the general-purpose and the proposed IQA methods were implemented for comparative analysis. The summary of the comparison is given in Table I. As compared to the conventional IQA methods, the proposed algorithm that employs only the exclusion of corner regions in the IQA metrics computation achieves lower values of PSNR and SSIM. When the corner region pixels, which are not affected by the image compression process, are excluded from the computation of the IAQ metrics, the MSE increases as given in equations 2 and 4. This, in turn, leads to a lower PSNR value in all the image compression algorithms as shown in equations 3 and 5. On the other hand, the exclusion of

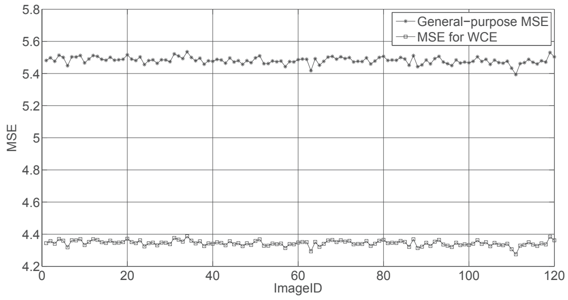

(a) Mean squared-error for 120 test images [24].

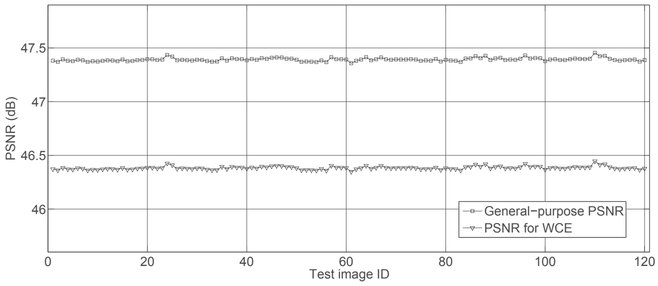

(b) PSNR value for 120 test images [24].

Fig. 5. Comparison of the MSE and PSNR values for the conventional and proposed IQA methods.

TABLE I
THE COMPARISON OF DIFFERENT IMAGE QUALITY ASSESSMENT METHODS.

Image Compression Methods	*Conventional IQA Methods*		*Proposed IQA Methods for WCE*			
	PSNR (dB)	*SSIM*	*Corner Clipping*		*Corner Clipping and Boundary Region Exclusion*	
			PSNR (dB)	*SSIM*	PSNR (dB)	*SSIM*
JPEG-based [3]	30.79	0.9998	30.07	0.9997	36.38	0.9997
DPCM-based [2]	38.23	0.9996	37.50	0.9995	41.65	0.9998
DCT-based [15]	38.62	0.9987	37.89	0.9985	38.94	0.9984
DWT-based [16]	39.90	0.9899	39.42	0.9894	40.56	0.9905
Modified H.264 [28]	38.29	0.9990	37.57	0.9988	37.76	0.9988
DCT-based [29]	43.60	0.9995	42.88	0.9994	43.66	0.9994
DCT-based [30]	31.45	0.9991	30.73	0.9991	31.38	0.9995
DCT and sub-sampling [23]	35.99	0.9049	35.26	0.9009	36.65	0.9061
Average	**37.11**	**0.9863**	**36.42**	**0.9857**	**38.37**	**0.9865**

the boundary region which is highly affected by the image compression processes reduces the MSE value and increases the PSNR value. In a nutshell, the exclusion of the corner regions alone reduces the PSNR value, whereas the removal of corner pixels alone increases the PSNR value. For the eight image compression algorithms implemented shown in Table I, the exclusion of corner regions in the computation of PSNR alone reduces it from 37.11 dB to 36.42 dB on average. Similarly, the exclusion of both corner regions and boundary region increases the PSNR value to 38.37 dB on average. This gives an improvement of 1.12 dB average value of PSNR. Hence, the combined effect is dominated by the impact of the boundary region between the corner regions and the visual region because this region is highly distorted by most the image compression algorithms due to the existence of sharp transition of pixel values at the boundary which leads to large values of high frequency components. This is consistent in all the images, compression algorithms. The observed PSNR value difference obtained differs from one algorithm to another since different algorithms induce a different level of distortion to the boundary region of WCE image.

Unlike the PSNR, SSIM value depends on image contrast, hue, and distribution of error [26], [27]. Because of this, we have not obtained a consistent pattern of changes in all image compression algorithms shown in Table I. On average, it is observed that the SSIM decreases from 0.9863 to 0.9857 with application of only corner clipping algorithm. It has increased to 0.9865 of average SSIM value with both corner clipping and boundary region omission in the computation of objective IQA for WCE images.

Obviously, the level of distortion of the corners pixels is zero since all the pixel values are zero. As a result, the average SSIM and PSNR values reduce when the corner region pixels are omitted in the computation of IQA metrics. The overall effect of corner clipping is decreasing the considered IQA metrics on average. The IQA metrics, which exclude only the boundary regions in the IQA computations, achieve a lower value of MSE compared to the original value as depicted in Fig. 4. Hence, it results in higher values of PSNR and SSIM than those of the conventional methods. This is due to the fact that the boundary region is highly affected by the image compression processes. The quantization and sub-sampling algorithms introduce high error at the boundary between the informative and non-informative regions due to the abrupt transition of intensity values of pixels in WCE images, as shown in Fig. 3. The distortion in these regions has no significance for the detection of abnormalities in this particular application. The modified IQA metrics, which are implemented with a combination of both corner clipping and boundary region exclusion in IQA metrics computation, show more realistic metric values than the conventional methods. Generally, the cumulative effect of excluding both regions is dominated by the impact of the boundary pixels. This shows that the distortion that occurs in the boundary region dominates the overall process, and the proposed IQA metrics are higher than that of the general-purpose IQA metrics. The simulation result shows consistent results for the majority of the evaluated image compression algorithms and test images, as shown in Fig. 5 (b).

Overall, more consistent image quality assessment metrics that are more correlated with subjective image quality assessment are proposed in this work, which can be reliably used in the image compression and super-resolution algorithm optimization process. The exclusion of the informative regions in the computation of the image quality assessment methods can sightly increase the computational complexity of the objective image quality assessment methods. However, with the workstation computational power, we have now, its impact in practical scenarios is negligible in terms of delay.

IV. CONCLUSION

In this paper, an application-specific objective image quality assessment method for wireless capsule endoscopy is presented. The proposed method uses knowledge about the statistics of the image acquisition system to improve the performance of the general-purpose image quality assessment methods. Specifically, the corner regions, which are not affected by image compression algorithms, and the boundary regions between informative and non-informative regions, which are highly distorted by the image compression algorithms, are excluded in the computation of the objective image quality assessment metrics. The distortion in these two regions has no significance for the detection of abnormalities in this particular application. Hence, the proposed algorithm has a higher correlation to subjective quality assessment than the general-purpose IQA metrics. The overall impact of excluding the two regions in the computation of IQA metrics is that the general-purpose image quality measures are lower than the IQA measures proposed for WCE particular application. The proposed IQA method can be used in the optimization of image compression and image super-resolution algorithms. The proposed algorithm can easily be applied to other image quality assessment methods such as FSIM [11] etc.

REFERENCES

[1] G. Iddan, G. Meron, A. Glukhovsky, and P. Swain, "Wireless capsule endoscopy," *Nature*, vol. 405, no. 6785, pp. 417–417, 2000.

[2] K. A. Fante, B. Bhaumik, and S. Chatterjee, "Design and implementation of computationally efficient image compressor for wireless capsule endoscopy," *Circuits, Systems, and Signal Processing*, vol. 35, no. 5, pp. 1677–1703, 2016.

[3] C. Cheng, Z. Liu, C. Hu, and M. Q.-H. Meng, "A novel wireless capsule endoscope with jpeg compression engine," in *2010 IEEE International Conference on Automation and Logistics*. IEEE, 2010, pp. 553–558.

[4] Y. Wang, C. Cai, and Y. Zou, "Single image super-resolution via adaptive dictionary pair learning for wireless capsule endoscopy image," in *2015 IEEE International Conference on Digital Signal Processing (DSP)*. IEEE, 2015, pp. 595–599.

[5] P. A. Floor, I. Farup, M. Pedersen, and Ø. Hovde, "Error reduction through post processing for wireless capsule endoscope video," *EURASIP Journal on Image and Video Processing*, vol. 2020, pp. 1–15, 2020.

[6] S. Charfi and M. El Ansari, "Computer-aided diagnosis system for colon abnormalities detection in wireless capsule endoscopy images," *Multimedia Tools and Applications*, vol. 77, no. 3, pp. 4047–4064, 2018.

[7] R. Istepanian, N. Philip, M. Martini, N. Amso, and P. Shorvon, "Subjective and objective quality assessment in wireless teleultrasonography imaging," in *2008 30th Annual International Conference of the IEEE Engineering in Medicine and Biology Society*. IEEE, 2008, pp. 5346–5349.

[8] Z. Wang and A. C. Bovik, "Modern image quality assessment," *Synthesis Lectures on Image, Video, and Multimedia Processing*, vol. 2, no. 1, pp. 1–156, 2006.

[9] J. Korhonen and J. You, "Peak signal-to-noise ratio revisited: Is simple beautiful?" in *2012 Fourth International Workshop on Quality of Multimedia Experience*. IEEE, 2012, pp. 37–38.

[10] Z. Wang, A. C. Bovik, H. R. Sheikh, and E. P. Simoncelli, "Image quality assessment: from error visibility to structural similarity," *IEEE transactions on image processing*, vol. 13, no. 4, pp. 600–612, 2004.

[11] L. Zhang, L. Zhang, X. Mou, and D. Zhang, "Fsim: A feature similarity index for image quality assessment," *IEEE transactions on Image Processing*, vol. 20, no. 8, pp. 2378–2386, 2011.

[12] M.-C. Lin, L.-R. Dung, and P.-K. Weng, "An ultra-low-power image compressor for capsule endoscope," *BioMedical Engineering OnLine*, vol. 5, no. 1, pp. 1–8, 2006.

[13] P. C. Cosman, R. M. Gray, and R. A. Olshen, "Evaluating quality of compressed medical images: Snr, subjective rating, and diagnostic accuracy," *Proceedings of the IEEE*, vol. 82, no. 6, pp. 919–932, 1994.

[14] L. He, F. Gao, W. Hou, and L. Hao, "Objective image quality assessment: a survey," *International Journal of Computer Mathematics*, vol. 91, no. 11, pp. 2374–2388, 2014.

[15] P. Turcza and M. Duplaga, "Low power fpga-based image processing core for wireless capsule endoscopy," *Sensors and Actuators A: Physical*, vol. 172, no. 2, pp. 552–560, 2011.

[16] K. A. Fante, B. Bhaumik, and S. Chatterjee, "A low-power color mosaic image compressor based on optimal combination of 1-d discrete wavelet packet transform and dpcm for wireless capsule endoscopy." in *BIODEVICES*, 2015, pp. 190–197.

[17] I. Intzes, H. Meng, and J. Cosmas, "An ingenious design of a high performance-low complexity image compressor for wireless capsule endoscopy," *Sensors*, vol. 20, no. 6, p. 1617, 2020.

[18] C. Babu, D. A. Chandy, and P. Karthigaikumar, "Novel chroma subsampling patterns for wireless capsule endoscopy compression," *Neural Computing and Applications*, vol. 32, no. 10, pp. 6353–6362, 2020.

[19] B. Sushma and P. Aparna, "Distributed video coding based on classification of frequency bands with block texture conditioned key frame encoder for wireless capsule endoscopy," *Biomedical Signal Processing and Control*, vol. 60, p. 101940, 2020.

[20] M. A. Usman, M. R. Usman, and S. Y. Shin, "Quality assessment for wireless capsule endoscopy videos compressed via hevc: From diagnostic quality to visual perception," *Computers in biology and medicine*, vol. 91, pp. 112–134, 2017.

[21] M. A. Usman and M. G. Martini, "On the suitability of vmaf for quality assessment of medical videos: Medical ultrasound & wireless capsule endoscopy," *Computers in biology and medicine*, vol. 113, p. 103383, 2019.

[22] L. Lévêque, H. Liu, S. Baraković, J. B. Husić, M. Martini, M. Outtas, L. Zhang, A. Kumcu, L. Platisa, R. Rodrigues *et al.*, "On the subjective assessment of the perceived quality of medical images and videos," in *2018 Tenth International Conference on Quality of Multimedia Experience (QoMEX)*. IEEE, 2018, pp. 1–6.

[23] M.-C. Lin and L.-R. Dung, "A subsample-based low-power image compressor for capsule gastrointestinal endoscopy," *EURASIP Journal on Advances in Signal Processing*, vol. 2011, no. 1, p. 257095, 2011.

[24] "Gastrolab," date last accessed January 10,2020. [Online]. Available: http://gastrolab.net/

[25] Q. Huynh-Thu and M. Ghanbari, "The accuracy of psnr in predicting video quality for different video scenes and frame rates," *Telecommunication Systems*, vol. 49, no. 1, pp. 35–48, 2012.

[26] A. Hore and D. Ziou, "Image quality metrics: Psnr vs. ssim," in *2010 20th international conference on pattern recognition*. IEEE, 2010, pp. 2366–2369.

[27] Z. Kotevski and P. Mitrevski, "Experimental comparison of psnr and ssim metrics for video quality estimation," in *International Conference on ICT Innovations*. Springer, 2009, pp. 357–366.

[28] L.-R. Dung, Y.-Y. Wu, H.-C. Lai, and P.-K. Weng, "A modified h. 264 intra-frame video encoder for capsule endoscope," in *2008 IEEE Biomedical Circuits and Systems Conference*. IEEE, 2008, pp. 61–64.

[29] P. Turcza and M. Duplaga, "Hardware-efficient low-power image processing system for wireless capsule endoscopy," *IEEE journal of biomedical and health informatics*, vol. 17, no. 6, pp. 1046–1056, 2013.

[30] K. Wahid, S.-B. Ko, and D. Teng, "Efficient hardware implementation of an image compressor for wireless capsule endoscopy applications," in *2008 IEEE International Joint Conference on Neural Networks (IEEE World Congress on Computational Intelligence)*. IEEE, 2008, pp. 2761–2765.

Kinde A. Fante received the BSc degree in Electrical Engineering from Bahir Dar University in 2008, the M.Tech degree in Electronics and Computer Engineering from Addis Ababa University, Ethiopia, in 2010,Ethiopia and the Ph.D. degree in Electrical Engineering from the Indian Institute of Technology Delhi, India, in 2016. Currently, he is an Assistant Professor in the Faculty of Electrical and Computer Engineering, Jimma Institute of Technology, Jimma University. His research interests include Biomedical Signal processing, low-power integrated circuits, VLSI design for real-time image and video processing, and machine learning.

Fetulhak Abdurahman received the BSc in Electrical Engineering in 2009 and the MSc in Computer Engineering in 2014 from Addis Ababa University. From 2009- 2020 working as a lecturer in Jimma University, Ethiopia. His research interest includes computer vision, pattern recognition and natural language processing.

Mulugeta T. Gemeda received a BSc degree in Electrical and Computer Engineering in 2017 and M.Sc. degree in Electronics Communication Engineering from Jimma University, Ethiopia, in 2019. Currently, he is working as Lecturer at Jimma Institute of Technology in the Faculty of Electrical and Computer Engineering, Jimma University. His research interests include antenna design, mobile communication, and computer networking.

A comparative study among PID structures applied on a Buck converter control

Luís Fabiano Barone Martins[1], Ricardo Breganon[2], Uiliam Nelson Lendzion Tomaz Alves[3], João Paulo Lima Silva de Almeida[4], and Elenilson de Vargas Fortes[5]

Abstract— **In this work, a state-space model and control of a DC-DC Buck converter, considering a continuous operating, are presented. A PID controller is considered in the strategy, that considers a low pass filter in the derivative term. The proposed model is validated by comparing it with a switched model. The PID gains are obtained by the Ziegler-Nichols method. In order to improve the system's performance considering an environment containing high-frequency noises, the modified PID controller is implemented with several configurations.**

***Index Terms*—Choppers, Step Down Converter, PID Controller, Ziegler-Nichols Method, Average Model.**

I. INTRODUCTION

POWER electronics is an applied science that aims the static converters study in order to control and convert electrical energy into a compatible signal (voltage level and/or frequency) to determined devices. These converters operate by switching semiconductor devices and they can classified as: AC-DC, AC-AC, DC-AC and DC-DC [1], [2].

DC-DC converters, also known as Choppers, are power electronic circuits with linear and non-linear characteristics, that are composed by resistors, capacitors and inductors and semiconductor switches, respectively [3]. Their applications encompass from power sources for electronic devices to photovoltaic generation plants. By controlling the input voltage switching, DC-DC converters can adjust the magnitude of the output voltage analogously to a AC transformer, adding the possibility of adjusting the output voltage [4].

The mentioned converters operate by the Pulse Width Modulation (PWM) principle, in which a semiconductor switch, actuated by a pulse generator, is used to control the amperage level from the input to the output of the electrical system [2], [4]. This technique aims to reach the highest efficiency as possible (100%), however, due to the real characteristics (non-ideal) of these semiconductor devices, a typical efficiency related to the converters ranges from 70% to 95% [5].

The four classical topologies for non-isolated DC-DC converters are: Cuk, Buck (Step-Down); Boost (Step-Up); and e Buck-Boost [6]. Each one of them has exclusive properties that include the steady-state voltage gain, the source of the input and output currents and the oscillatory characteristics of the output voltage. The most common topology, and probably the simplest, is the Buck (step-down), possibly because its output voltage is always less than the input voltage, with the same polarity and not isolated.

The first step to project an efficient controller to the Choppers is to obtain a complete system's model, including the most part of the non-linearities. A linear model with small signals, by means of a state-space average model around an adequate operation point, is a valid option [7].

In general, the most control techniques applied on Choppers represents a challenging field due to their non-linear and time-varying characteristics [8]. These techniques perform the switching control of the semiconductor devices aiming the maximization of the efficiency related to the power transfer and the good tracking of the output voltage. Several control techniques are used in these converters, although there is a preference for controllers with simple and low cost architecture in industrial applications [9], [10]. In this way, Proportional-Integrative-Derivative (PID) controllers are highlighted [11], [12].

One of the most popular method to adjust the PID gains is the proposed by Ziegler e Nichols (ZN) [13], due to its simple rules and satisfactory performances when it is applied on first order systems [14]. In general, ZN method is used to tune PID controllers under ideal conditions without significant noises and disturbances, which often does not represent a real situation. Therefore, it is necessary to consider their effects in the control algorithm [15].

On the other hand, a filter system is necessary when there are significant noise levels in the control plant. Traditionally, filters are applied on derivative term, due to its characteristic in amplification high-frequency noises.

This work approaches the high-frequency noise effects in DC-DC Buck converter coupled to a PID controller, with a low-pass filter in the derivative term and tuned by ZN method.

To do this, a linear model to small disturbances of the Buck converter is considered, by means of the average state-space model and also considering the dynamic of the PID controller. Finally, the system's output response for two different PID gains with the low-pass filter in the derivative term is compared with a standard PID architecture.

The rest of the paper is divided as follows: the PID control structures considered in this work are presented in Section II; in Section III, the mathematical description of the PID controller considering the average model of the Buck converter is addressed; the ZN method is discussed in Section IV; the main results and conclusions are presented in the Sections V and VI, respectively.

II. PID CONTROLLER

The feedback loop in control systems aims to provide the real output signal (controlled variable added to noises, disturbances, and others) of the plant to the control system's input and then to generate a signal to be applied on the manipulated variable, according to the considered control law and aiming to reach a desired reference. The PID controller uses this feedback concept with the proportional (P), integrative (I) and derivative (D) gains, all of them related to the error (difference between the desired reference and the real output signal), which present specific contributions in the control signal calculation [16]. The well-known PID topology, the ISA algorithm [17], is presented in Eq. (1).

$$u(t)=k_p\left(e(t)+\frac{1}{T_i}\int_0^t e(\tau)\,d\tau+T_d\frac{de(t)}{dt}\right) \tag{1}$$

where u is the control variable; $e=r-y$ is the error calculation; r is the reference value (set point); y is the controlled variable (system's output); while T_i and T_d are constants integral and derivative times, respectively, and k_p is the proportional gain of the PID controller.

Although simple, the control output computed by the Eq. (1) presents severe implications in real applications, mainly due to the derivative part (related to T_d constant time), that carries out noise amplification and then the control variable (u) may be unfeasible.

Let n a sinusoidal noise with amplitude and frequency(ω) given by (2), and u_n is its contribution to the derivative term in the control signal, given by (3).

$$n=a\sin(\omega t) \tag{2}$$

$$\begin{aligned}u_n&=k_pT_d\frac{d}{dt}\left[a\sin(\omega t)\right]=ak_pT_d\,\omega\cos(\omega t)\\&=k_{hf}\,a\cos(\omega t)\end{aligned} \tag{3}$$

According to Eq. (3), when $\omega\to\infty$, $k_{\mathrm{hf}}\to\infty$.

In order to avoid unfeasible values (very high values) from derivative part in high frequencies, a common procedure is to limit its bandwidth using a low-pass filter with the transfer function (TF) defined in (4) [18].

$$G_f=\frac{1}{\alpha T_d s+1} \tag{4}$$

According to [16], acceptable values for α ranges from 0.05 to 0.125. Converting ISA algorithm presented in Eq. (1) into frequency domain and applying the TF of Eq. (4) to derivative term, Eq. (5) can be defined.

$$U(s)=k_p\left[1+\frac{1}{sT_i}+\frac{sT_d}{s(\alpha T_d)+1}\right]E(s) \tag{5}$$

In addition to limiting gains of the high frequency components from the error, by the relation k_p/α , the low-pass filter solves the problem of the non-causality of the ideal PID controller (Eq. (1)) adding a pole in its transfer function.

III. ZIEGLER-NICHOLS METHOD

Ziegler and Nichols publish in 1942 a work [19] in which two they describe two strategies to tune P, PI and PID gains. These strategies contemplate a step and frequency response methods. In this work, the step response method is adopted.

Ziegler and Nichols defined as acceptable that the ratio between the amplitude peaks (due to a disturbance in the operation point) in the closed-loop response (A_1 and A_2 in Fig. 1 (a)) is about 4. However, there is no guarantee that this ratio corresponds to a real system, after tunning process.

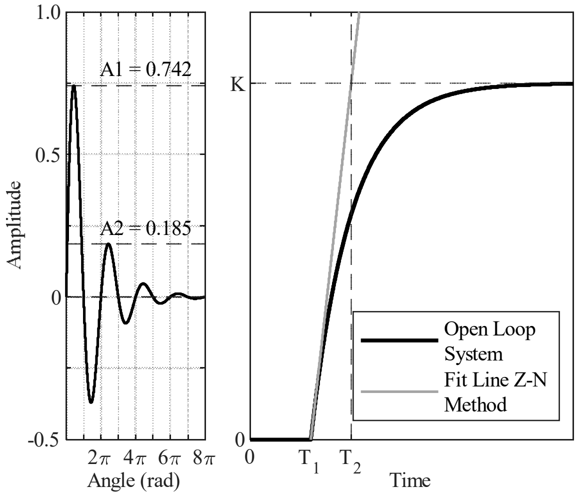

(a) (b)

Fig. 1. (a) Impulse response of a system with transport delay; (b) Step response method.

An illustrative example of the step response method is shown in Fig. 1 (b), considering an open-loop system. This response represents a first-order system with delay transport and its transfer function $H(s)$ is presented in Eq. (6).

$$H(s)=\frac{K}{(T_2-T_1)s+1}e^{-sT_1} \tag{6}$$

The first-order response (Fig 1 (b)) is composed by two parameters: the time delay (T_1) and the time constant T_2-T_1. They can be determined with a tangent line to the inflection point and by observing its intersections between the axis related to the time and the state-steady value, K.

In real time control systems, a wide variety of process plant can be modeled as (6) and from K, T_1 and T_2 it is possible to obtain the controller gains as described in TABLE I.

TABLE I
CONTROLLER'S GAINS OBTAINED FROM THE STEP RESPONSE METHOD.

Tipo do controlador	k$_p$	T$_i$	T$_d$
P	$\frac{T_2-T_1}{T_1}$		
PI	$\frac{9}{10}\frac{T_2-T_1}{T_1}$	$\frac{10}{3}T_1$	
PID	$\frac{6}{5}\frac{T_2-T_1}{KT_1}$	$2T_1$	$\frac{1}{2}T_1$

IV. PID CONTROLLER ADDED TO THE AVERAGE STATE SPACE MODEL

In DC-DC Buck converter, shown in Fig. 2, the input voltage is represented by an ideal DC source V_{in}, while the switch S is a MOSFET transistor. i_L is the current through inductor L, v_C is the capacitor's voltage (C) and $d \in [0,1]$ is the PWM's duty cycle and it is the control signal of the switch S. R and D are resistor and diode, respectively.

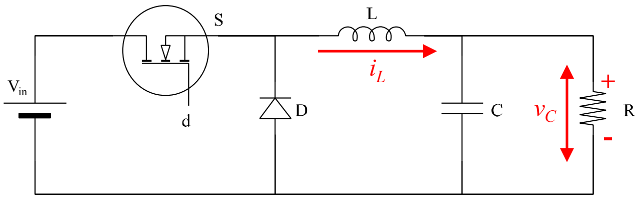

Fig. 2. DC-DC Buck converter.

In order to determine the differential equations of the Buck converter, with switching period T, the Kirchhoff's Laws are applied to each functioning state, that is, when S is closed at $[0,dT]$ and when S is open at $[dT,T]$. In this way, the average state space model for the Buck converter [7] is given by Eq. (7)-(8).

$$\dot{i}_L=-\frac{1}{L}v_C+\frac{V_{in}}{L}d \tag{7}$$

$$\dot{v}_C=\frac{1}{C}i_L-\frac{1}{RC}v_C \tag{8}$$

The transfer function in (9) is related to the capacitor voltage under a small duty cycle variation around the operation point of the Buck converter.

$$G(s)=\frac{\Delta v_C(s)}{\Delta d(s)}=\frac{\frac{1}{LC}}{s^2+\frac{1}{RC}s+\frac{1}{LC}}V_{in} \tag{9}$$

From the Buck converter definition (Eq. (7)-(8)), an expanded state-space model is proposed, including the modified PID dynamics (Eq. (5)).

The Buck converter dynamic with a PID controller can be described by (10).

$$\begin{aligned}\dot{x}&=f(x,w,u)\\0&=h(x,w,u)\\y&=g(x,w,u)\end{aligned} \tag{10}$$

where f, h and g represent differential, algebraic and output equations, respectively, while x, w and u are the following vectors, respectively: state variables, algebraic vector and system's input.

The use of linear techniques for stability analysis under small disturbances in a dynamic system is a valid approach due to its linearization around an equilibrium point. In this way, assuming small variations around the operation point (x_0,w_0,u_0), the linearized form of (10) can be described in matrix form as (11).

$$\begin{bmatrix}\Delta\dot{\mathbf{x}}\\\mathbf{0}\\\Delta\mathbf{y}\end{bmatrix}=\begin{bmatrix}\mathbf{J}_1&\mathbf{J}_2&\mathbf{B}_1\\\mathbf{J}_3&\mathbf{J}_4&\mathbf{B}_2\\\mathbf{J}_5&\mathbf{J}_6&\mathbf{B}_3\end{bmatrix}\begin{bmatrix}\Delta\mathbf{x}\\\Delta\mathbf{w}\\\Delta\mathbf{u}\end{bmatrix} \tag{11}$$

In (11), $\mathbf{J}$ matrices are the system's Jacobians at the equilibrium point (x_0,w_0,u_0). Assuming that $\mathbf{J}_4$ is non-singular, $\Delta\mathbf{w}$ (vector of linearized algebraic variables) can be excluded and then the linear and time-invariant in (11) can be rewritten as (12).

$$\begin{bmatrix}\Delta\dot{\mathbf{x}}_e\\\Delta\mathbf{y}\end{bmatrix}=\begin{bmatrix}\mathbf{A}_e&\mathbf{B}_e\\\mathbf{C}_e&\mathbf{D}_e\end{bmatrix}\begin{bmatrix}\Delta\mathbf{x}_e\\\Delta\mathbf{u}\end{bmatrix} \tag{12}$$

In (12), the state $\mathbf{A}_e$, input $\mathbf{B}_e$, output $\mathbf{C}_e$ and feedback $\mathbf{D}_e$ matrices can be defined, respectively by Eq. (13)-(16).

$$\mathbf{A}_e=\mathbf{J}_1-\mathbf{J}_2\mathbf{J}_4^{-1}\mathbf{J}_3 \tag{13}$$

$$\mathbf{B}_{\mathrm{e}} = \mathbf{B}_1 - \mathbf{J}_2\mathbf{J}_4^{-1}\mathbf{B}_2 \tag{14}$$

$$\mathbf{C}_{\mathrm{e}} = \mathbf{J}_5 - \mathbf{J}_6\mathbf{J}_4^{-1}\mathbf{J}_3 \tag{15}$$

$$\mathbf{D}_{\mathrm{e}} = \mathbf{B}_3 - \mathbf{J}_6\mathbf{J}_4^{-1}\mathbf{B}_2 \tag{16}$$

For the system addressed in this paper, the output variables are not related to the system's input which implies $\mathbf{D}_{\mathrm{e}} = \mathbf{0}$.

In order to represent the Buck converter with a control about the capacitor voltage v_C, as in (12), it is necessary to consider each term of the PID dynamic equation (Eq. (5)), individually. From that, Fig. 3 illustrates the considered control structure through block diagram with the algebraic and states variables from (7) and (8).

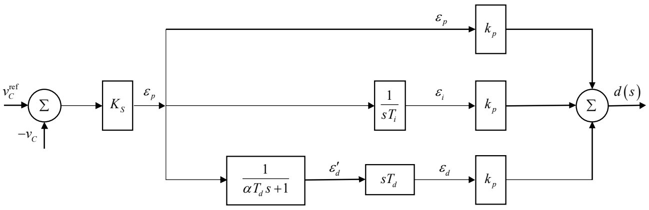

Fig. 3. Block diagram of the system with the PID controller.

From Fig. 3, it is possible to obtain the new state variables, ε_i and ε_d', in addiction to the equations that define the algebraic variables ε_p, ε_d and $d(s)$, as shown in Eq. (17)-(21), respectively.

$$\dot{\varepsilon}_i = \frac{1}{T_i}\varepsilon_p \tag{17}$$

$$\dot{\varepsilon}_d' = \frac{1}{\alpha T_d}\left(\varepsilon_p - \varepsilon_d'\right) \tag{18}$$

$$\varepsilon_p = K_S\left(-v_C + v_C^{\mathrm{ref}}\right) \tag{19}$$

$$\varepsilon_d = \frac{1}{\alpha}\left(\varepsilon_p - \varepsilon_d'\right) \tag{20}$$

$$d = k_p\left(\varepsilon_p + \varepsilon_i + \varepsilon_d\right) \tag{21}$$

Applying the linearization by first order Taylor approximation to Eq. (7)-(8) and (17)-(21) and considering the linearized system's output as $\Delta y = \Delta v_C$, it is possible to obtain the matrix formulation for the complete system PID-Buck, as shown in (22), in which the vector of the expanded state variables $\mathbf{\Delta x}_{\mathrm{e}} = \left[\Delta i_L \quad \Delta v_C \quad \Delta\varepsilon_i \quad \Delta\varepsilon_d'\right]^t$.

$$\left[\begin{array}{c} \Delta\dot{i}_L \\ \Delta\dot{v}_C \\ \Delta\dot{\varepsilon}_i \\ \Delta\dot{\varepsilon}_d' \\ \hline 0 \\ 0 \\ 0 \\ \hline \Delta y \end{array}\right] = \left[\begin{array}{cccc|ccc|c} 0 & -\frac{1}{L} & 0 & 0 & 0 & 0 & \frac{V_{\mathrm{in}}}{L} & 0 \\ \frac{1}{C} & -\frac{1}{RC} & 0 & 0 & 0 & 0 & 0 & 0 \\ 0 & 0 & 0 & 0 & \frac{1}{T_i} & 0 & 0 & 0 \\ 0 & 0 & 0 & -\frac{1}{\alpha T_d} & \frac{1}{\alpha T_d} & 0 & 0 & 0 \\ \hline 0 & -K_S & 0 & 0 & -1 & 0 & 0 & K_S \\ 0 & 0 & 0 & -\frac{1}{\alpha} & \frac{1}{\alpha} & -1 & 0 & 0 \\ 0 & 0 & k_p & 0 & k_p & k_p & -1 & 0 \\ \hline 0 & 1 & 0 & 0 & 0 & 0 & 0 & 0 \end{array}\right] \left[\begin{array}{c} \Delta i_L \\ \Delta v_C \\ \Delta\varepsilon_i \\ \Delta\varepsilon_d' \\ \hline \Delta\varepsilon_p \\ \Delta\varepsilon_d \\ \Delta d \\ \hline \Delta v_C^{\mathrm{ref}} \end{array}\right] \tag{22}$$

The submatrices $\mathbf{J}$ and $\mathbf{B}$ are used to determine $\mathbf{A}_{\mathrm{e}}$, $\mathbf{B}_{\mathrm{e}}$ and $\mathbf{C}_{\mathrm{e}}$, from (22) and (13)-(16), resulting (23)-(25).

$$\mathbf{A}_{\mathrm{e}} = \begin{bmatrix} 0 & -\frac{1}{L} - \frac{V_i k_p(\alpha+1)K_S}{\alpha L} & \frac{V_i k_p}{L} & -\frac{V_i k_p}{\alpha L} \\ \frac{1}{C} & -\frac{1}{RC} & 0 & 0 \\ 0 & -\frac{K_S}{T_i} & 0 & 0 \\ 0 & -\frac{K_S}{\alpha T_d} & 0 & -\frac{1}{\alpha T_d} \end{bmatrix} \tag{23}$$

$$\mathbf{B}_{\mathrm{e}} = \begin{bmatrix} \frac{V_i k_p(\alpha+1)K_S}{\alpha L} & 0 & \frac{K_S}{T_i} & \frac{K_S}{\alpha T_d} \end{bmatrix}^t \tag{24}$$

$$\mathbf{C}_{\mathrm{e}} = \begin{bmatrix} 0 & 1 & 0 & 0 \end{bmatrix} \tag{25}$$

From Eqs. (23)-(25), it is possible to represent the dynamic model of the Buck converter in matrix form and compact, when it is under small disturbances around an operating point $\left(\mathbf{X}_{\mathrm{e}}, v_C^{\mathrm{ref}}\right)$.

The transfer function ($G_P(s)$), aiming the control of voltage v_C, is obtained according to the model parameters in state space, assuming that the disturbance inputs are null, as in Eq. (26).

$$G_P(s) = \frac{\Delta v_C(s)}{\Delta v_C^{\mathrm{ref}}(s)} = \mathbf{C}_{\mathrm{e}}\left(s\mathbf{I} - \mathbf{A}_{\mathrm{e}}\right)^{-1}\mathbf{B}_{\mathrm{e}} \tag{26}$$

In this work, results obtained considering the both PID (standard) and modified, according to Eq. (1) and (5), respectively, are compared, in order to validate the approach addressed in this paper. For that, the transfer function of each compared controller, defined in (27) and (28), with the constants a_0, a_1, a_2 and a_3, is defined in Eq. (29)-(32).

$$G_{P1}(s)=\frac{a_0\left(T_iT_d s^2+T_i s+1\right)}{s^3+a_2 s^2+a_1 s+a_0} \qquad (27)$$

$$G_{P2}(s)=$$

$$\frac{\frac{1}{\alpha T_d}a_0\left[(\alpha+1)T_iT_d s^2+\left(T_i+\alpha T_d\right)s+1\right]}{s^4+\frac{1}{\alpha T_d}a_3 s^3+\frac{1}{\alpha T_d}\left(a_2+\alpha T_d a_1\right)s^2+\frac{1}{\alpha T_d}\left(a_1+\alpha T_d a_0\right)s+\frac{1}{\alpha T_d}a_0} \qquad (28)$$

$$a_0=\frac{1}{LC}\frac{k_p K_S V_i}{T_i} \qquad (29)$$

$$a_1=\frac{1}{LC}\left(k_p K_S V_i+1\right) \qquad (30)$$

$$a_2=\frac{1}{LC}\left[k_p K_S V_i T_d+\frac{L}{R}\right] \qquad (31)$$

$$a_3=\frac{1}{LC}\left(LC+\alpha T_d\frac{L}{R}\right) \qquad (32)$$

V. RESULTS

The proposed system, based on the transfer functions of Buck converter, $G(s)$, and PID controller, $G_C(s)$, and considering the voltage sensor gain, K_S, can be represented through the diagram of Fig. 4.

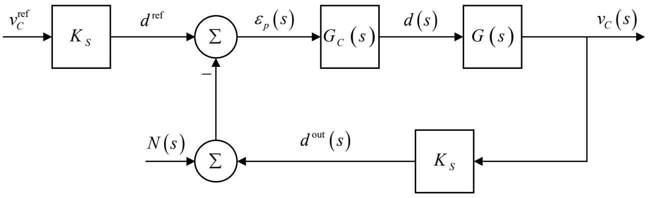

Fig. 4. System's diagram.

In Fig. 4, $N(s)$ represents the measurement noises of v_C and $G_C(s)$ encompasses Eq. (27)-(32) and the characteristics of the Buck converter shown in TABLE II.

TABLE II
PARAMETERS OF THE CONTROLLED SYSTEM

PARAMETER	VALUE
Input voltage (V_{in})	12 V
Output voltage (v_C)	5 V
Inductance (L)	2.4 mH
Output capacitance (C)	5.6 µF
Load resistance (R)	10 Ω
PWM frequency (f)	10 kHz

With the output power of 10 W, the ripples of the output voltage, δv_C, and of the inductor's current, δi_L, are 5.39% and 6.04%, respectively, which leads the converter to operate in continuous mode.

In order to validate the average state-space model of the Buck converter, represented by Eq. (7) and (8), the simulation software PSIM® was used. To do that, all parameters of TABLE II were considered to obtain the switched model response. Furthermore, a 5V step was applied in the reference voltage of the switched models, aiming to obtain the open-loop response. The respective responses under disturbances are presented in Fig. 5.

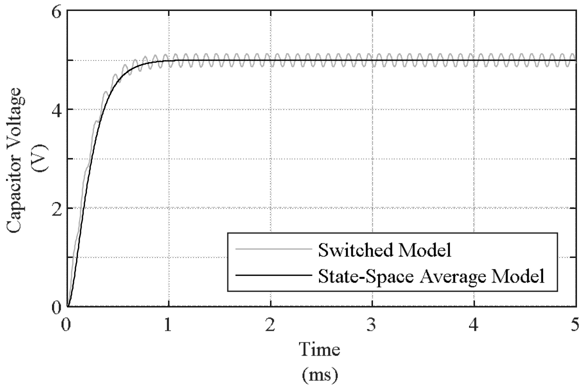

Fig. 5. Transfer functions' response related to the state-space and switched model.

It is important to highlight in Fig. 5 that the state-space average model is a satisfactory representation of the converter's dynamic under low frequency. The suppression of high frequency components of the switched model, due to the discontinuity of the switching process, occurs with the use of average values of the instantaneous variables for a switching period of the power switch S of Fig. 2.

After validation of the average model, the response of the open-loop transfer function not compensated was obtained (Fig. 6), considering $G_C(s)=1$ and $N(s)=0$. In this way, a step of 0.415 was applied in the duty-cycle of PWM reference (d^{ref}). That response is presented in Fig. 6 and it can be represented by (6) with a line tangent to its inflection point.

The constants of static gain, transport delay and apparent time (Eq. (6)) can be determined by inspection of Fig. 6, that is, $K=0.415$, $T_1=32$ µs and $T_2-T_1=322$ µs. Based on these values and according to the TABLE I, the PID parameters are presented in TABLE III.

TABLE III
GAIN AND TIME CONSTANTS OF PID CONTROLLER BY MEANS OF ZIEGLER-NICHOLS METHOD.

Controller	k_p	***T_i (µs)***	***T_d (µs)***
PID	29	64	16

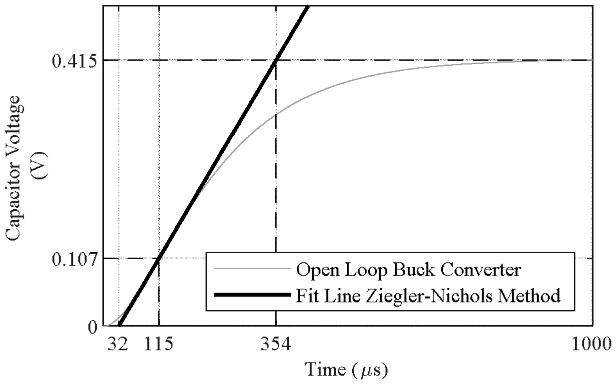

Fig. 6. Response for Ziegler-Nichols method.

Applying the constants of TABLE I and III in the closed-loop transfer function presented in (27), that is, considering a standard PID ($\alpha = 0$), it is possible to determine the constants about damping ($\xi = -0.391$) and the damped frequency ($\omega_d = 36.4$ krad/s) of the oscillatory mode caused by the pair of conjugated complex poles. The time response with $v_C^{\text{ref}} = 5$ V is presented in Fig. 7.

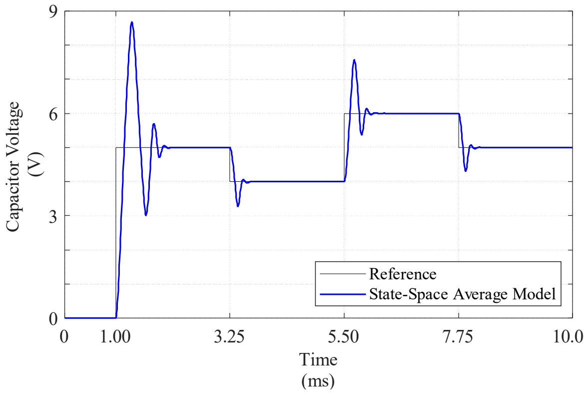

Fig. 7. Response of the capacitor voltage (v_C) with changes in the reference voltage (v_C^{ref}).

From the response presented in Fig. 7, it is possible to conclude that the controlled variable presents low accommodation time for starting ($T_a < 1$ ms) and for disturbances around the equilibrium point ($T_a < 0.7$ ms), however the percentual overshoot is higher than 60%. Therefore, if the designer aims a better performance for overshoot characteristic, a fine tuning would be necessary in the PID gains.

According to the literature [16]–[18], a standard PID controller requires a special attention in its derivative term when it is applied in real process. In order to mitigate this situation, a modified structure is considered in this work, in which a low-pass filter is added to derivative term, as presented in (5). To compare the performance between the standard and modified PID architectures, a Gaussian noise (average value equal to zero, components at frequencies up to 2.5 MHz and standard deviation $\sigma = 0.1$) is inserted into the system.

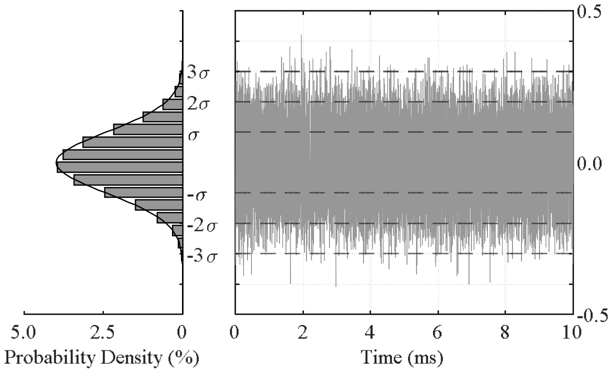

(a)
(b)

Fig. 8. (a) Density and probability function; (b) Gaussian noise.

The response of the density and probability function is shown in Fig. 8 (a), while in Fig. 8 (b) is the Gaussian noise along the time (applied in $N(s)$).

To compare the performance between the considered standard and modified PID controllers, 3 levels of α (Eq. (28)) are considered: $\alpha = 0$ (PID standard in (27)); $\alpha = 0.05$; and $\alpha = 0.125$. The last two values are chosen based on [16]. The system's responses to small disturbances around the operation point, considering the two mentioned controllers are presented in Fig. 9.

In the first experiment ($\alpha = 0$), the obtained response is the dotted line (Fig. 9), which suggests the difficulty of the control action to follow the reference quickly, when this characteristic is compared to the other cases. In the following experiments, with $\alpha = 0.05$ and $\alpha = 0.125$, the responses are presented in blue and black colors, respectively. It is reasonable to conclude that the voltage v_C is faster when $\alpha = 0.125$, in which there is a greater rejection of high-frequency disturbances due to the modified PID. This effect can be explained due to the lower cutoff frequency of the low-pass filter with $\alpha = 0.125$ (79 kHz), when it is compared to $\alpha = 0.05$ (198 kHz).

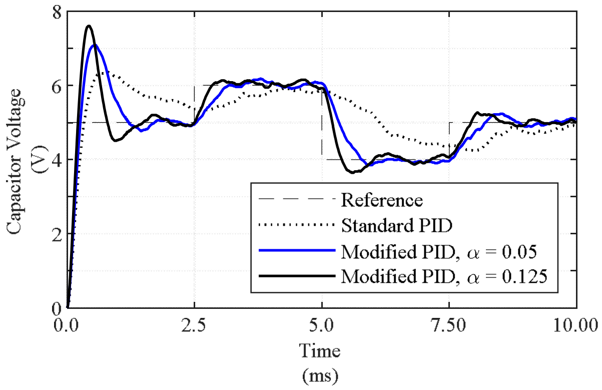

Fig. 9. Response of the capacitor voltage (v_C) to the changes in the reference voltage (v_C^{ref}).

It is important to notice that the increase of α causes a higher overshoot in the system's response related to the reference voltage, what is expected due to the decrease in the derivative term.

VI. CONCLUSIONS

A modified PID controller (a low-pass filter is added to the derivative term) was considered in the state-space average model of a DC-DC Buck converter. From the expanded state equations, that is, adding the controller dynamics, two closed-loop transfer functions were obtained, related to the use of standard and the modified PID controllers, respectively.

In order to validate the proposed model, its step response was compared to the switching model available on PSIM® software and the obtained results show equivalent dynamics.

The PID controller was tuned by means of Ziegler-Nichols method. Is can be observed that, from a step input reference, the output voltage reaches acceptable performance, according to the project requirements adopted in this work.

Aiming the minimization of a high frequency noises effects, a low-pass filter was considered in the derivative term of the PID controller. Its performance was compared to a standard PID, according to the literature. From the presented results, it can be concluded that the system's output shows faster response, when it is compared to the other addressed cases.

In future works, we intend to consider other control techniques with optimization methods, aiming to minimize the overshoot and the stabilization time.

REFERENCES

[1] N. Mohan and M. P. E. R. \& Education, *First Course on Power Electronics and Drives*. MNPERE, 2003.

[2] B. K. Bose, "Power electronics-a technology review," *Proc. IEEE*, 1992, doi: 10.1109/5.158603.

[3] R. B. Ridley, "A New, Continuous-Time Model For Current-Mode Control," *IEEE Trans. Power Electron.*, 1991, doi: 10.1109/63.76813.

[4] N. Mohan, T. M. Undeland, and W. P. Robbins, *Power electronics: converters, applications, and design*, no. v. 1. John Wiley \& Sons, 2003.

[5] R. W. Erickson, "DC–DC Power Converters," in *Wiley Encyclopedia of Electrical and Electronics Engineering*, American Cancer Society, 2007.

[6] E. Van Dijk, J. N. Spruijt, D. M. O'Sullivan, and J. B. Klaassens, "PWM-switch modeling of DC-DC converters," *IEEE Trans. Power Electron.*, vol. 10, no. 6, pp. 659–665, 1995, doi: 10.1109/63.471285.

[7] R. D. Middlebrook and S. Cuk, "A general unified approach to modelling switching-converter power stages," in *1976 IEEE Power Electronics Specialists Conference*, 1976, pp. 18–34, doi: 10.1109/PESC.1976.7072895.

[8] S. Buso, "Design of a robust voltage controller for a buck-boost converter using /spl mu/-synthesis," *IEEE Trans. Control Syst. Technol.*, vol. 7, no. 2, pp. 222–229, 1999, doi: 10.1109/87.748148.

[9] C. K. Tse and K. M. Adams, "Quasi-linear modeling and control of DC-DC converters," *IEEE Trans. Power Electron.*, vol. 7, no. 2, pp. 315–323, 1992, doi: 10.1109/63.136248.

[10] A. J. Forsyth and S. V. Mollov, "Modelling and control of DC-DC converters," *Power Eng. J.*, vol. 12, no. 5, pp. 229–236, 1998, doi: 10.1049/pe:19980507.

[11] S. Seshagiri, E. Block, I. Larrea, and L. Soares, "Optimal PID design for voltage mode control of DC-DC buck converters," in *2016 Indian Control Conference (ICC)*, Jan. 2016, pp. 99–104, doi: 10.1109/INDIANCC.2016.7441112.

[12] D. E. Rivera, M. Morari, and S. Skogestad, "Internal model control: PID controller design," *Ind. Eng. Chem. Process Des. Dev.*, vol. 25, no. 1, pp. 252–265, Jan. 1986, doi: 10.1021/i200032a041.

[13] J. G. Ziegler and N. B. Nichols, "Optimum Settings for Automatic Controllers," *J. Dyn. Syst. Meas. Control*, vol. 115, no. 2B, pp. 220–222, 1993, doi: 10.1115/1.2899060.

[14] C. C. Hang, K. J. Astrom, and W. K. Ho, "Refinements of the Ziegler-Nichols tuning formula," *IEE Proc. D - Control Theory Appl.*, vol. 138, no. 2, pp. 111–118, 1991, doi: 10.1049/ip-d.1991.0015.

[15] S. Agrawal, V. Kumar, K. P. S. Rana, and P. Mishra, "Optimization of PID controller with first order noise filter," in *2015 International Conference on Futuristic Trends on Computational Analysis and Knowledge Management (ABLAZE)*, 2015, pp. 226–231, doi: 10.1109/ABLAZE.2015.7154996.

[16] K. J. Äström and T. Hägglund, *Advanced PID control*. Research Triangle Park, NC: ISA-The Instrumentation, Systems, and Automation Society, 2006.

[17] A. O'Dwyer, *Handbook of PI and PID controller tuning rules*, 3rd ed. Covent Garden, London: Imperial College Press, 2009.

[18] M. A. Johnson *et al.*, *PID control: New identification and design methods*. London: Springer-Verlag, 2005.

[19] J. G. Ziegler and N. B. Nichols, "Optimum Settings for Automatic Controllers," *The American Society of Mechanical Engineers (ASME)*, vol. 64, pp. 759–768, 1942.

Luís Fabiano Barone Martins is Professor at the Federal Institute of Paraná, Jacarezinho, is graduated in Electrical Engineering from São Paulo State University (UNESP), Campus Ilha Solteira, MSc. degree in Electrical Engineering and PhD. degree in Electrical Engineering from UNESP Campus Bauru and Ilha Solteira, respectively. His research interests include Electrical Power Systems, Power Electronics, Bio-Inspired Optimization Metaheuristics, Industrial Automation and Dynamic Systems Control.

Ricardo Breganon is Professor at the Federal Institute of Paraná, Jacarezinho, holds degree in Production Engineering from Estacio de Sa University and in Mechanical Technology from Federal Technological University of Paraná, MSc. degree in Mechanical Engineering and PhD. degree in Mechanical Engineering with a concentration in Aeronautical from School of Engineering of São Carlos - University of São Paulo. His research interests include Industrial Automation and Dynamic Systems Control.

Uiliam Nelson L. T. Alves is graduated in Control and Automation Engineering from UniCesumar, Maringá, PR, Brazil (2011). MSc. and PhD. in Electrical Engineering from UNESP (Universidade Estadual Paulista), Campus of Ilha Solteira, SP, Brazil in 2014 and 2017, respectively. At this moment, he is Control and Industrial Processes professor in IFPR (Instituto Federal de Educação, Ciência e Tecnologia do Paraná), campus Jacarezinho. His research interests include Fuzzy modeling and control, Robust and nonlinear control.

João Paulo Lima Silva de Almeida received the B.Sc. degree in Industrial Automation (2011), the M.Sc. degree in Electrical Engineering (2014) and the Ph.D. degree in Electrical Engineering (2019) from Federal University of Technology - Paraná. He has been with the Federal Institute of Paraná, since 2012. His research interests include intelligent systems to model and control dynamic systems.

Elenilson de Vargas Fortes received the degree in mathematics in 2004 from the Federal University of Espírito Santo, São Mateus, Brazil, the M.Sc. degree in mathematics in 2007 from the Federal University of Brasília, Brasília, Brazil, and the Ph.D. degree in electrical engineering in 2016 from the São Paulo State University, Ilha Solteira, Brazil. He is currently a professor at the Goiás Federal Institute of Education, Science, and Technology, Jataí, Brazil. His current research interests include small-signal stability analysis in power systems.

Prediction of Probabilistic Transient Stability Using Support Vector Machine

Umair Shahzad

Abstract**—Transient stability assessment is an integral part of dynamic security assessment of power systems. Traditional methods of transient stability assessment, such as time domain simulation approach and direct methods, are appropriate for offline studies and thus, cannot be applied for online transient stability prediction, which is a major requirement in modern power systems. This motivated the requirement to apply an artificial intelligence-based approach. In this regard, supervised machine learning is beneficial for predicting transient stability status, in the presence of uncertainties. Therefore, this paper examines the application of a binary support vector machine-based supervised machine learning, for predicting the transient stability status of a power system, considering uncertainties of various factors, such as load, faulted line, fault type, fault location and fault clearing time. The support vector machine is trained using a Gaussian Radial Basis function kernel and its hyperparameters are optimized using Bayesian optimization. Results obtained for the IEEE 14-bus test system demonstrated that the proposed method offers a fast technique for probabilistic transient stability status prediction, with an excellent accuracy. DIgSILENT PowerFactory and MATLAB was utilized for transient stability time-domain simulations (for obtaining training data for support vector machine) and for applying support vector machine, respectively.**

Index Terms**—Artificial Intelligence (AI), dynamic security assessment (DSA), machine learning, probabilistic transient stability, support vector machine (SVM).**

I. INTRODUCTION

THE reliability of a power system is defined as the ability of the power system to provide electric energy to consumers on a continuous basis and with acceptable service quality, for both planned and unplanned outages [1]. One of the main requirements to maintain the reliability of the power is to continually operate the synchronous generators and with satisfactory capacity to satisfy the load. In the domain of power system stability, transient stability is the ability of the synchronous machines to remain in synchronism during few seconds (usually 5-10 seconds), after a large disturbance, such as a short circuit fault, occurs [2]. In addition to fault type, fault location, system inertia, and system load, fault clearing time (FCT) and critical clearing time (CCT) are significant parameters in assessing transient stability [3]. FCT is the time at which fault is cleared after fault occurrence, whereas CCT is the maximum FCT after which the system becomes transiently unstable [3]. Transient stability is an integral component of dynamic security assessment (DSA). DSA deals with evaluation of transient performance of the system after the occurrence of contingency [2]. To evaluate the transient stability status, time-domain simulation approach is generally used to solve a set of nonlinear differential-algebraic equations, which represent the dynamics of the network [4]. Although, the time-domain approach is the most accurate method and usually yields promising results, it is time consuming, as it must traverse a set of differential-algebraic equations, which can be computationally intensive, especially for large-scale systems [5]. The transient energy function (TEF) method [6]-[7], and the extended equal area criterion (EEAC) [8] have also been applied to transient stability evaluation; however, these approaches have some restrictions regarding modeling, and they require many computations to evaluate an index for transient stability status [9]. Moreover, these methods are not appropriate for online transient stability prediction [10].

Conventionally, deterministic methods, employing worst-case scenarios (seasonal peak load, three-phase fault, etc.), have been used to evaluate transient stability [11]-[13]. These approaches are very conservative and ignore the probability of various input parameters linked with transient stability, such as load, fault type, fault location, etc. With the continuous integration of renewable generation, the increasing prevalence of competitive electricity market, and the rising uncertainties in the power system, these conventional methods are becoming obsolete and unsuitable. Compared with the deterministic assessment approaches, probabilistic assessment techniques can provide an inclusive and realistic measure of system stability status [14]. Novel probabilistic assessment techniques are desirable and are being established. Probabilistic transient stability (PTS) assessment has been recognized to be a fitting approach to analyze the effect of uncertain parameters on transient stability [15]–[21]. Additionally, the results from PTS analysis can be associated with risk assessment, which is imperative for system operators, as economic and technical reasons can result in the power system to operate near the stability limit [21]. Although, it has been long established that deterministic studies may not sufficiently characterize the full extent of system dynamic behavior, the probabilistic approach has not been extensively used in the past in power system studies,

U. Shahzad is with the Department of Electrical and Computer Engineering, University of Nebraska-Lincoln, Lincoln, NE, 68588-0511 USA (email: umair.shahzad@huskers.unl.edu).

mainly due to lack of data, limitation of computational resources, limited commercial softwares for probabilistic analysis, deterministic nature of standards enforced by regulatory authorities, such as North American Electric Reliability Corporation (NERC), and mixed response from power utilities and planners [17], [20]. However, in recent times, there has been some research in PTS. For instance, [22] presented an analytical approach to determine PTS for online applications. [23]-[24] used Monte-Carlo Simulation (MCS) approach to present a stochastic-based approach to assess the PTS index. [15] proposed the inclusion of probabilistic considerations in transient stability investigation of a multimachine practical power system. Some other relevant work can be found in [25]-[30]. A major drawback of these works is that these use conventional numerical and analytical methods, such as, MCS, time-domain simulation, EEAC, TEF, hybrid method, etc. to estimate the transient stability index. These approaches may be suitable for an offline study, however, for real-time online prediction, a faster method is required. Artificial intelligence (AI)-based approaches provide a good alternative to fulfil this vital objective.

Among various AI approaches, Machine learning (ML) is an upcoming approach for solving power system problems, including transient stability [31]-[33]. ML is generally classified into three categories: supervised, unsupervised and reinforcement [34]. In supervised learning, the goal is to learn a mapping relation between the inputs to outputs, based on a given a labeled set of input/output pairs. Unsupervised learning deals with the training of an algorithm is using unlabeled data so that the algorithm may group the data based on similarity or difference. In reinforcement learning (RL), there is an interaction of an agent with its environment and consequently, the agent adapts its course, based on the reward because of its actions. The focus of this research work is Supervised Machine Learning (SML). Although, SML has various types [35], such as Artificial Neural Network (ANN), Decision Tree (DT), Random Forest, Support Vector Machine (SVM), etc., this work focuses on SVM-based SML for prediction of PTS.

In recent years, application of ML algorithms, such as ANN, to power system is an area of rising interest; the chief reason being the ability of ANN to process and learn intricate nonlinear relations [36]. Although ANN is the most commonly used ML method for transient stability classification, it generally requires an extensive training process and an intricate design procedure. Moreover, ANN usually performs well for interpolation but not so well for extrapolation, which reduces its generalization ability. They are more susceptible to becoming trapped in a local minimum. Although, majority of ML algorithms can overfit if there is a dearth of training samples, but ANNs can also overfit if training goes on for a very long duration [37]. Due to these downsides, it becomes essential to develop a more efficient classifier for transient stability status prediction. SVM do not suffer from these drawbacks and has the following advantages, over ANN [38]: (1) less number of tuning parameters, (2) less susceptibility to overfitting, and (3) the complexity is depended on number of support vectors (SVs) rather than dimensionality of transformed input space.

Support vector machine (SVM) is an evolving ML approach that incapacitates some of the drawbacks of ANN. A SVM essentially is a SML algorithm that can use given data to solve certain problems by trying to convert them into linearly separable problems. Recently, SVM has been applied to power system transient stability classification problem. An SVM-based transient stability classifier was trained in [39] and its performance was compared with a multilayer perceptron (MLP) classifier. Reference [37] devised a multiclass SVM classifier for static and transient stability assessment and classification. Reference [40] suggested a SVM classifier to predict the transient stability status using voltage variation trajectory templates. Reference [38] trained a binary SVM classifier, with combinatorial trajectories inputs, to predict the transient stability status. Reference [41] employed the SVM to rank the synchronous generators based on transient stability severity and classify them into vulnerable and nonvulnerable machines. Reference [42] proposed two SVMs, using Gaussian kernels, for classifying the post-fault stability status of the system. Reference [43] presented an SVM-based approach for transient stability detection, using post-disturbance signals, from the optimally located distributed generations. Some other relevant work dealing with SVM-based transient stability classification can be found in [44]-[51]. Based on the detailed literature review and to the best of author's knowledge, there exists no research work on PTS which uses SVM-based SML approach, considering the uncertainties of load, faulted line, fault type, fault location (on the line), and FCT. Moreover, [52] specifically mentions the potential of SVM for online DSA, and [53]-[57] strongly indicate that ML is a promising and upcoming approach for online DSA. Thus, the main contribution of this paper is to predict PTS status using an SVM-based SML approach. As mentioned before, although, the time-domain simulation method is one of the most accurate methods to assess transient stability; it is very computationally intensive, particularly for large scale systems. Hence, this method is only suitable for offline applications. On the contrary, the direct analytical methods are comparatively fast, but requires a large number of approximations which significantly limit the model accuracy. The TEF-based methods are difficult to implement, especially due to many potential function terms of the TEF of the system. Also, these approaches require postfault data for transient stability assessment, and hence, they are not suitable for online transient stability assessment. Therefore, new approaches must be explored and applied to real-scale power systems to ensure accurate and effective online prediction of transient stability. Thus, this paper proposed an artificial intelligence-based approach for this application, and this is the main novelty and contribution of this research.

The rest of the paper is organized as follows. Section II describes various probabilistic factors associated with transient stability assessment. Section III discusses the PTS index used in this paper. Section IV provides a brief overview of SVM and its application to PTS classification problem.

Section V discusses the procedure for the proposed approach. Section VI and VII deals with the description of case study, and associated results and discussion, respectively. Section VIII describes sensitivity analysis, with respect to some important parameters/functions. Finally, Section IX concludes the paper, with a suggested direction for future research.

II. PROBABILISTIC FACTORS IN POWER SYSTEM TRANSIENT STABILITY

There are various factors which are involved in PTS assessment of power systems, such as fault type, fault location, load, and FCT. Suitable probability density functions (PDFs) are used to model these factors. The modeling approaches are described below [58]. Normally, shunt faults, such as three-phase (LLL), double-line-to-ground (LLG), line-to-line (LL) and single-line-to-ground (LG) short circuits, are considered for evaluating PTS. A probability mass functions (PMF) is normally used to model the fault type. Based on past system statistics, a usual practice is to select the probability of LLL, LL, LLG, and LG short circuits, as 0.05, 0.1, 0.15 and 0.7 respectively [22]. This paper adopts the same practice. The probability distribution of fault location on a transmission line is usually assumed to be uniform. This means that the fault can occur with equal probability at any line of the test system and at any point along the line [21]. This paper uses the same approach. The procedure of fault clearing constitutes of three stages: fault detection, relay operation and breaker operation. If the primary protection and breakers are 100% reliable, the clearing time is the only uncertain factor. A normal (Gaussian) PDF is generally used to model this time [21]. In this paper, fault is applied at 1 *s* and it is cleared, after a mean time of 0.9 *s* and standard deviation of 0.1 *s* (based on the normal PDF). A normal PDF was used to represent the uncertainty of loads. Let *f(X)* denote the PDF for individual bus loads, i.e.,

$$f(X) = \frac{1}{\sqrt{2\pi\sigma^2}} e^{\frac{-(X-\mu)^2}{2\sigma^2}} \qquad (1)$$

where μ and σ denotes the mean and standard deviation of the forecasted peak load, respectively.

III. QUANTIFICATION INDEX FOR PROBABILISTIC TRANSIENT STABILITY

The Transient Stability Index (*TSI*) was used to quantify the transient stability of a system consisting of synchronous machines [59]. This index is based on the maximum rotor angle separation between any two synchronous machines, after the fault has occurred. Mathematically, it is given by

$$TSI_i = \frac{360 - \delta_{\max i}}{360 + \delta_{\max i}}, \text{ where } -1 < TSI_i < 1 \qquad (2)$$

where $\delta_{\max i}$ is the post-fault maximum rotor angle separation (in degrees) between any two synchronous machines in the system at the same time (for a fault on i^{th} line). A negative *TSI* value indicates that the power system is transiently unstable. This is a global index for a swift indication of the transient stability status of the system (for a fault on any line, at any point, for any FCT and for any load). Therefore, this index is used in this paper to quantify the PTS status. Let S_i represent the PTS status indicator for i^{th} iteration of MCS. Mathematically,

$$S_i = \begin{cases} 1\,, & \text{if } TSI_i < 0 \\ 0, & \text{if } TSI_i \geq 0 \end{cases} \qquad (3)$$

Therefore, if the system is transiently stable, for i^{th} Monte-Carlo (MC) sample, value of S_i will be 0; otherwise, it will be 1. This information will be used for training the SVM model.

IV. SVM: BRIEF OVERVIEW AND APPLICATION TO PROBABILISTIC TRANSIENT STABILITY PREDICTION

Support vector machine (SVM), which is also known as maximum margin classifier, is a type of SML, that can be used both in classification and regression problems. It was first introduced by Vapnik [60]-[61] and was elaborated by Schölkopf et al. [62]. SVM classifiers depend on training points, which lie on the boundary of separation between different classes, where the evaluation of transient stability is important. A decent theoretical progress of the SVM, due to its basics built on the Statistical Learning Theory (SLT) [60], made it possible to develop fast training methods, even with large training sets and high input dimensions [63]-[65]. This useful characteristic can be applied to tackle the issue of high input dimension and large training datasets in the PTS problem. The basic implementation of an SVM, commonly known as a hard margin SVM, requires the binary classification problem to be linearly separable. This is frequently not the case in practical problems, and therefore, SVM provides a kernel trick to resolve this issue. The forte of the SVM algorithm is based on the use of this kernel trick to transform the input space into a higher dimensional feature space. This permits to define a decision boundary that linearly separates the classes. The SVM algorithm attempts to determine that decision boundary or hyperplane with the highest distance from each class [38], [66]. The hyperplane can be mathematically defined as [39]

$$(w^T x) + b = 0 \qquad (4)$$

where w is the weight vector (w^T is its transpose), x is the sample feature vector, and b is a bias value. The samples that assist the algorithm to define the optimal hyperplane are those that lie closest to it, and they are known as SVs. The kernel function plays a significant role in SVM classification [67]. The kernel function is applied on each data instance to map the original non-linear data points into a higher-dimensional space in which they become linearly separable. An SVM classifier minimizes the generalization error by optimizing the relation between the number of training errors and the so-called Vapnik-Chervonenkis (VC) dimension. This is attained using the approach of structural risk minimization (SRM) which states that the classification error expectation of unseen data is bounded by the sum of a training error rate and a term that depends on the VC dimension [39]. Compared to empirical risk minimization (ERM)-based formulation (which is used by most ML algorithms, including ANN), the SRM-based formulation allows the SVM to prevent overfitting problems, by defining an upper bound, on the expected risk. A formal theoretical bound exists for the generalization ability of an SVM, which depends on the number of training errors (*t*), the size of the training set (*N*), the VC dimension associated to the resulting classifier (*h*), and a chosen confidence measure for the bound itself (η) [39], [61], [68]:

$$R < \frac{t}{N} + \sqrt{\frac{h(\ln(\frac{2N}{h})+1) - \ln(\frac{\eta}{4})}{N}} \tag{5}$$

The risk (or classification error expectation) *R* represents the classification error expectation over all the population of input/output pairs, even though the population is only partially known. This risk is a measure of the actual generalization error and does not require prior knowledge of the probability distribution of the data. SLT derives inequality (5) to mean that the generalization ability of an SVM is measured by an upper limit of the actual error given by the right-hand side of (5), and this upper limit is valid with a probability of 1-η (0< η<1). As *h* increases, the first summand of the upper bound (5) decreases and the second summand increases, such that there is a balanced compromise between the two terms (complexity and training error), respectively [39]. The SVMs used for binary classification problems are based on linear hyperplanes to separate the data, as shown in Fig. 1. The hyperplane (represented by dotted line in Fig. 1) is determined by an orthogonal vector *w* and a bias *b*, which identify the points that satisfy $(w^T x) + b = 0$. By determining a hyperplane which maximizes the margin of separation, denoted by ρ, it is instinctively anticipated that the classifier will have an improved generalization ability. The hyperplane having the largest margin on the training set can be completely determined by the points that lie closest to the hyperplane. Two such points are x_1 and x_2 as shown in in Fig. 1 (b), and they are known as SVs because the hyperplane (i.e., the classifier) is completely dependent on these vectors. Consequently, in their simplest form, SVMs learn linear decision rules as

$$f(x) = sign(w^T x + b) \tag{6}$$

so that (*w, b*) are determined as to correctly classify the training examples and to maximize ρ. For linearly separable data, as shown in Fig. 1, a linear classifier can be found such that the first summand of bound (5) is zero.

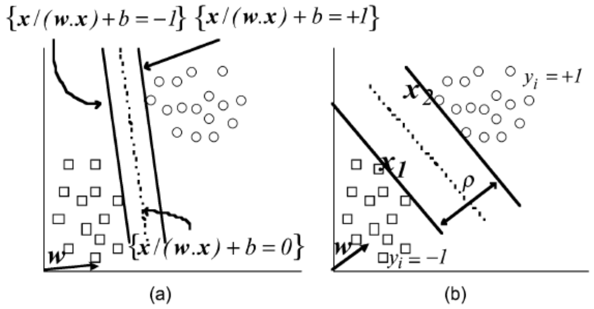

Fig. 1. SVM (maximum margin) classifier.

It is always possible to scale *w* and *b* such that

$$w^T x + b = \pm 1 \tag{7}$$

for the SVs, with

$$w^T x + b > +1 \text{ and } \; w^T x + b < -1 \tag{8}$$

for non-SVs.

Using the SVs x_1 and x_2 of Fig. 1 and (7), the margin ρ can be calculated as

$$\rho = \frac{w^T}{||w||}(x_2 - x_1) = \frac{2}{||w||} \tag{9}$$

where $||w||$ is the Euclidean Norm of *w*. For linearly separable data, the VC dimension of SVM classifiers can be evaluated as

$$h < \min\left\{n, \frac{4D^2}{\rho^2}\right\} + 1 = \min\left\{n, D^2 \square \quad \square\right\} \tag{10}$$

where *n* is the dimension of the training vectors and *D* is the minimum radius of a ball which contains the training points. Thus, the risk (5) can be reduced by lessening the complexity of the SVM, that is, by increasing the margin of separation ρ, which is equivalent to reducing $||w||$. In practice, as the problems are not probable to be detachable by a linear classifier, thus, the linear SVM can be extended to a nonlinear version by mapping the training data to an expanded feature space using a nonlinear transformation:

$$\Phi(x) = (\phi_1(x), \ldots\ldots, \phi_m(x)) \in R^m \tag{11}$$

where *m* > *n*. Then, the maximum margin classifier of the data for the new space can be determined. With this method, the data points which are non-separable in the original space may become separable in the expanded feature space. The next step is to approximate the SVM by minimizing (i.e., maximizing ρ)

$$V(w) = \frac{1}{2} w^T . w \tag{12}$$

subject to the constraint that all training patterns are correctly classified, i.e.,

$$y_i \cdot \{w^T \cdot \Phi(x_i) + b\} \geq 1, \quad i = 1, \ldots, N \tag{13}$$

Though, contingent on the kind of nonlinear mapping (11), the samples of training data may not be linearly separable. In this case, it is not possible to find a linear classifier that satisfies all the conditions given by (12). Thus, instead of (12), a new cost function is optimized, i.e.,

$$\begin{aligned} &\min \, V(w, \varepsilon) = \frac{1}{2} w^T . w + C \sum_{i=1}^{N} \varepsilon_i \\ &s.t. \;\; y_i \cdot \{w^T \cdot \Phi(x_i) + b\} \geq 1 - \varepsilon_i \;\; \text{for } i = 1, \ldots, N \\ &\qquad\qquad \varepsilon_i \geq 0 \qquad\qquad \text{for } i = 1, \ldots, N \end{aligned} \tag{14}$$

where N non-negative slack variables ε_i are introduced to allow training errors (i.e., training patterns for which $y_i \cdot \{w^T \cdot \Phi(x_i) + b\} \geq 1 - \varepsilon_i$ and $\varepsilon_i > 1$) and allow for some misclassification. By minimizing the first summand of (14), the complexity of the SVM is reduced, and by minimizing the second summand of (14), the number of training errors is decreased. C is a positive penalty factor (also known as regularization factor or soft margin parameter) which decides the tradeoff between the two terms. In case it is small, the separating hyperplane is more focused on maximizing the margin (at the expense of larger classification mistakes), while the number of misclassified points is minimized for larger C values (at the expense of keeping the margin small). The minimization of the cost function (14) leads to a quadratic optimization problem with a unique solution. The nonlinear mapping (11) is indirectly obtained by the kernel functions, which correspond to inner products of data vectors in the expanded feature space $K(a,b) = \Phi(a)^T \cdot \Phi(b),\ a,b \in R^n$ [39], [46], [68]. Common kernel functions include the linear, polynomial, sigmoid and Gaussian radial basis function (RBF). In general, there is no fixed criterion for selecting these kernel functions. It majorly depends on whether the data is linearly separable or not, and how many dimensions exist When the number of features is very large (depending on the data), dimensionality reduction is applied first using Principal Component Analysis (PCA) or Linear Discriminant Analysis (LDA) (linear or nonlinear kernel variants). In general, the RBF kernel is a reasonable first choice. In short, there is no way to figure out which kernel would do the best for a particular problem. The only way to choose the best kernel is to actually try out all possible kernels, and consequently, choose the one empirically performs the best. One can empirically determine the optimal kernel via experimentation. Doing so involves three major steps: (1) implementing a version of the SVM model using each kernel, (2) evaluating the SVM model's performance with each kernel via cross validation, and (3) selecting the kernel that yielded optimal results.

The Gaussian RBF kernel generally is preferred over others because it has the ability of mapping samples nonlinearly into a higher dimensional space, and therefore, unlike linear kernel, it can tackle the scenario when the relationship between class labels and attributes is nonlinear. Although, sigmoid kernel performs like a Gaussian RBF kernel for certain parameters, but there are some parameters for which the sigmoid kernel is not the dot product of two vectors, thus, it is invalid. Moreover, as compared to polynomial kernel, it has few hyperparameters (parameters whose values are used to control the learning process) [61]. Thus, this work uses a Gaussian RBF kernel, which is mathematically given by,

$$K(a,b) = e^{-(\gamma\square \quad \square}, \ \gamma > 0,\ \gamma = \frac{1}{2\sigma^2} \tag{15}$$

where γ denotes the kernel parameter of the SVM classifier and σ is the width of the Gaussian function.

The hyperparameters C and γ impact how sparse and easily separable the training data are in the expanded feature space. Subsequently, these parameters decide the complexity and training error rate of the resulting SVM classifier. These parameters must be optimized for achieving the best performance for the SVM classifier. The block diagram for the proposed SVM framework is shown in Fig. 2. The proposed SVM framework used has four inputs (system load, fault type, fault location and FCT), and one output (for S_i). Samples for training data were chosen using the MCS-based time domain simulation approach (described in Section V).

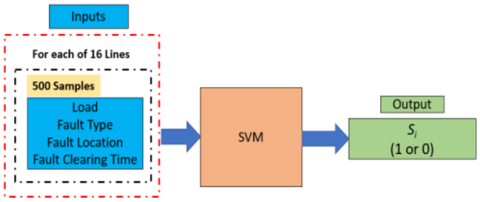

Fig. 2. Framework for the proposed SVM approach (input features and corresponding output).

For the PTS classification task, the first step was feature extraction, i.e., to select the most relevant input and output data for the SVM classification model. System load, fault type, fault location, and FCT were chosen as inputs, and transient stability status, S_i, was selected as the output (the binary variable to be classified as transiently stable or unstable). 500 samples were used for each line to train the SVM model, as shown in Table I. It must be mentioned that generally, there is no accepted rule of thumb to determine the number of samples for training the ML model; this typically depends on complexity of the problem, required performance level, and the ML algorithm used. As there are 16 lines in the system, thus, the total number of samples used for SVM model were 8000 (500×16). Thus, the size of the input feature matrix was 8000×4. The Gaussian RBF kernel function was used for training the SVM as there is ample nonlinearity amongst the data presented to the SVM classifier. The hyperparameters C and γ were optimized using Bayesian optimization (other approaches such as Grid search or Random search may also be used). The optimum values of C, γ, and σ were found to be 210, 0.22, and 1.5, respectively. The data presented to SVM is randomly divided in two subsets: training subset and testing subset. The K-fold cross-validation approach is used to accomplish this as this prevents over fitting while training the data. In this approach, the entire data is divided into K partitions of equal size. Training and testing are repeated, each time selecting a different partition for testing data, until all K partitions are utilized for testing, i.e., every data point gets to be in a test set exactly once and gets to be in a training set (K-1) times [38]. Eventually, the average of these errors is taken as the expected prediction error. This work used the value of K as 5, i.e., in each fold, 20% data was used for testing and 80% for training.

V. PROCEDURE FOR THE PROPOSED APPROACH

The methodology for the proposed approach is described in Fig. 3. The IEEE-14 bus system was used to test and validate the proposed approach. This system has 16 transmission lines. For each line, 500 random MC samples were generated (the symbol i indicates the sample number for the MCS). It is assumed that pre-fault system topology (configuration) is fixed, i.e., there is no contingency before the fault occurrence. In the first step, the first line is selected. In the next step, MCS is initiated with 500 samples. In each sample, system load, fault type, fault location and FCT are randomly chosen (based on the respective defined PDFs, as described in Section II). The fault is created at time t=1 s. For each MC sample, time-domain stability simulation is run for 10 s to determine the outcome (transiently stable or unstable). This is determined based on the value of S_i, as described in Section III. These steps are repeated and MCS is performed (for 500 samples) for all the remaining lines. When the MCS is run for all the 16 lines in the network, the resulting data obtained is used as training data for the SVM classification model.

A summarized workflow of SML application for online PTS prediction is shown in Fig. 4. As illustrated, the first step deals with the offline mode. In this mode, time-domain simulations are conducted, considering the uncertainties of input variables in the form of PDFs (generally obtained from past historical observations). In the next step, these distributions are sampled to gather enough training data. For each sample, the PTS status is measured by a binary variable, say, x, which can take two labels (say, 1 for transiently unstable, and 0 for transiently stable). Therefore, the final training data consists of the PTS status labels and the corresponding input operating conditions. In the next step, this offline-based database is used for online PTS prediction. The SML model 'learns' the stability rules and consequently, can be used to predict the PTS status for current operating point.

VI. CASE STUDY

The IEEE 14-bus test transmission system was used to conduct the required simulations. The numerical data and parameters were taken from [69]. The single line diagram is shown in Fig. 5. It should be highlighted that the proposed methodology is applicable to any test system. As mentioned before, a normal PDF is used to define the uncertainty in system loads. The active power of each load was assigned a mean equal to the original load active power value, as given in test system data in [69], and a standard deviation equal to 10% of the mean value. All time-domain simulations are RMS simulations and are performed using DIgSILENT PowerFactory software [70]. For SML application, Classification Learner tool of MATLAB was used [71].

TABLE I
SELECTED FEATURES FOR EACH LINE

Feature Name	Number of Samples
System load	500
Fault type	500
Fault location	500
FCT	500

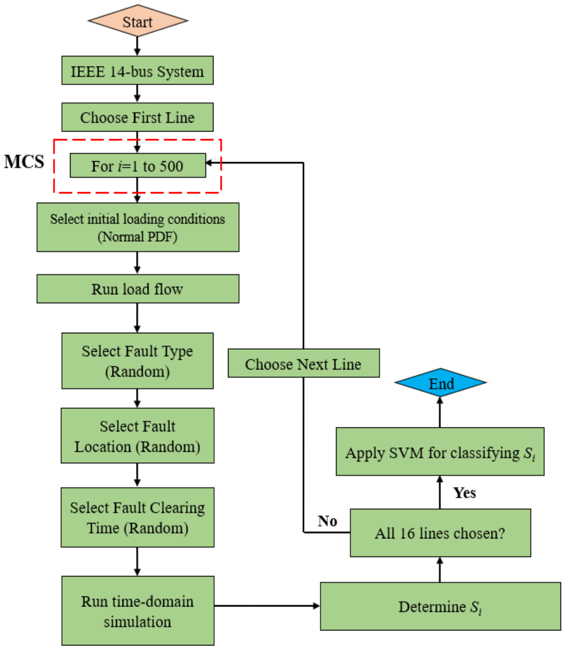

Fig. 3. Flowchart for the proposed SVM approach.

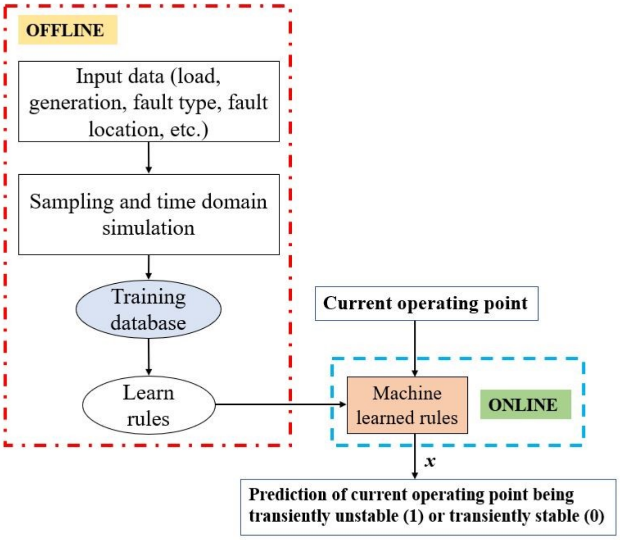

Fig. 4. Proposed SML approach for online PTS prediction.

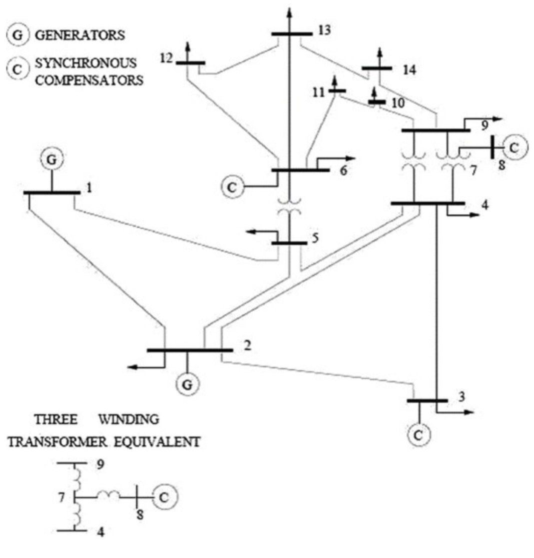

Fig. 5. IEEE 14-bus test system.

VII. Results and Discussion

It is assumed that required accuracy of the classifier must be more than 95%. To quantify the performance of the trained SVM classifier, the confusion matrix was used. This matrix is a graphical representation of the number of samples predicted correctly and incorrectly. The confusion matrix obtained for PTS classification is shown in Fig. 6 (1 and 0 represents transiently unstable and transiently stable class, respectively). Classification accuracy (*CA*) is a commonly used classification performance metric [72]. It is calculated as the proportion of correct predictions from the total number of the data points. The ideal value of *CA* is 1, whereas the worst is 0. It is mathematically defined as

$$CA = \frac{TP+TN}{TP+TN+FP+FN} = \frac{TP+TN}{N} \tag{16}$$

where *TP* (true positives), *TN* (true negatives) denotes the correctly predicted data, and *FP* (false positives), *FN* (false negatives) denotes the incorrectly predicted data. *N* denotes total data points (which are 8000 in this paper). Similarly, classification error (*CE*) represents the number of incorrect predictions from the total number of the data points. The closer it is to zero, the better. Mathematically,

$$CE = \frac{FP+FN}{TP+TN+FP+FN} = \frac{FP+FN}{N} \tag{17}$$

A receiver operating characteristic (ROC) curve is a graphical plot that establishes the diagnostic ability of a binary ML classifier [73]. In this plot, the true positive rate (sensitivity) is plotted against the false positive rate (1-specificity). Sensitivity is a measure of actual positives which are correctly identified, whereas specificity is the proportion of truly negative cases that were classified as negative [74]. A classification SVM model with perfect discrimination has a ROC plot that passes through the upper left corner (100% sensitivity, 100% specificity), i.e., its area under curve (*AUC*) is equal to 1. The closer the *AUC* is to 1, the greater the classification accuracy. The confusion matrix and the ROC curve (for testing data), for the classification of S_i, are shown in Fig. 6 and Fig. 7, respectively. From Fig. 6, it is evident that *CA* for the confusion matrix is very high, i.e., approximately 97% (59.46% + 37.23%). Moreover, as evident from Fig. 7, the ROC curve is very accurate (*AUC* >0.99). The values of various classification metrics are summarized in Table II. As evident, values for *CA* and *AUC* are in the desired high accuracy range (>0.95), and *CE* is quite small (0.033). Once trained, the SVM classifier can be directly used to classify S_i. The training time for the SVM classifier was only 0.03 *s*. Thus, it can be inferred that the trained SVM algorithm can rapidly classify the PTS status, S_i, with a high accuracy (≈97%). This makes it suitable for an online application and therefore, can drastically help power system operators in the control center for decision-making tasks.

Thus, to sum up, the proposed SVM approach can be used to predict the PTS status, incorporating various uncertain factors (system load, faulted line, fault type, fault location, and FCT), with a superior accuracy. This approach has an edge over the conventional approaches, as it is computationally efficient, as well as, fairly accurate. It is strongly believed that the proposed approach can drastically contribute to progressing the prevailing methods for online DSA.

It must be mentioned that the proposed ML algorithm is system-specific and, although, it performed quite well for the IEEE 14-bus system, it is not assured that it will perform the same for other systems. Therefore, ample testing and validation of the proposed approach must be conducted on other standard test systems, before reaching a generic conclusion on the performance of ML algorithm. Additional generic limitations exist for ML-based approach, for instance, the training database and ML model must be updated when the PDFs of the input random variables, and the network topology varies over time, and consequently, the number of transient stability simulations required for training may be greater than that estimated for a fixed topology. An additional limitation regarding SVM is that it is sensitive to noise (target classes overlap) and outliers (target classes deviate significantly from the rest of the classes), and consequently, does not give a good performance. Moreover, choosing the optimal kernel function is not straightforward and may require several optimization simulations [75]. Also, the best ML approach may change depending on the application [55]. An avid reader can refer to [76] for further details.

VIII. Sensitivity Analysis

As mentioned before, the value of *K* used in this work was 5. To verify that it is indeed the best value, a sensitivity analysis was performed. The SVM classifier was trained for various values of *K*, and the corresponding *CA* values were determined. The results obtained are shown in Fig. 8. As evident, increasing *K* beyond 5 does not alter the *CA*. Hence, *K*=5 is a good choice for *K*-fold cross-validation, for this work. This also validates the fact that *K*=5 and *K*=10 are generally the most commonly used values for a *K*-fold cross-validation procedure [77]. Moreover, for *K*=5, the values of *CA*, *CE*, and *AUC*, for different kernel functions, are shown in Table III. As evident, Gaussian RBF kernel has the highest accuracy and minimum error. This also validates the reason of Gaussian RBF kernel being the most commonly used kernel function for SVM classification [61]. Also, Table IV displays optimal values of various hyperparameters obtained for the proposed SVM model. Table V displays the comparison of performance metrics for the proposed approach with other related research. As evident, the results obtained by the proposed approach are comparable to similar research, and hence, this validates its effectiveness for the desired application of transient stability status prediction, in the presence of uncertainties. Table VI presents a comparison of the proposed method with conventional approaches, in terms of computational performance. As evident, the proposed SVM method is quite fast in predicting the transient stability status. Hence, the approach is very useful for online application. Moreover, various recent research [78-80] has indicated the significance of using SVM for transient stability prediction.

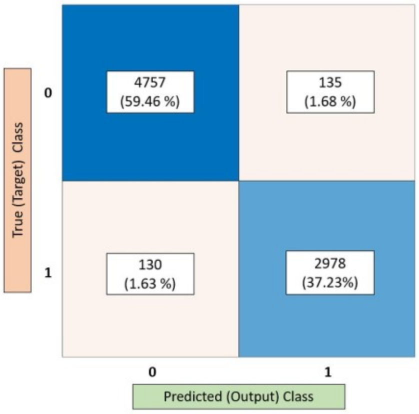

Fig. 6. Confusion matrix for transient stability classification performance assessment.

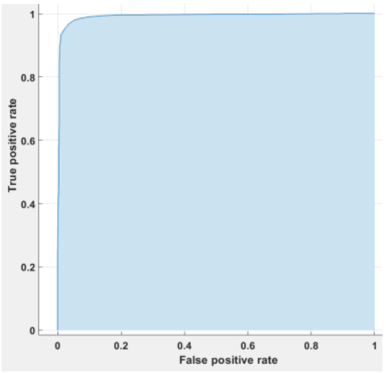

Fig. 7. ROC curve for transient stability classification performance assessment.

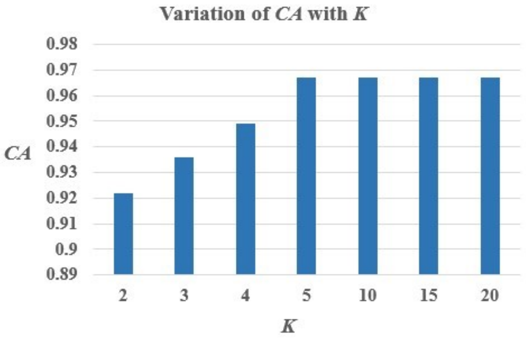

Fig. 8. Variation of *CA* with *K*.

IX. CONCLUSION AND FUTURE WORK

Power system transient stability is an integral part of power system planning and operation. Traditionally, it has been assessed using deterministic approach. With the increasing system uncertainties, environmental pressures of incorporating green energy, and widespread electricity market liberalization (deregulation), there is a strong need to incorporate probabilistic analysis in transient stability evaluation. Moreover, conventional approaches (direct method, time-domain simulation method, TEF approach, etc.) to assess transient stability are time consuming and hence, are not suitable for online application. ML can provide a good alternate to achieve this important goal. Hence, this paper applies an SVM-based approach to predict transient stability status, in the presence of uncertainty.

The paper highlighted the need to consider a faster method for PTS assessment and hence, proposed a binary SVM approach for predicting PTS status. In addition to uncertain system load conditions, various uncertain factors such as faulted line, fault type, fault location and FCT were considered. Time-domain simulations were used to gather the data required for training the SVM model. The *TSI* was used as the indicator for the PTS status. The proposed method was applied to the IEEE 14-bus system, and promising results were obtained, indicating the significance of SVM in power system PTS assessment. The results indicated that the proposed approach predicted the PTS status with an excellent accuracy, in a computationally efficient manner. This indicates the potential of SVM for online DSA, especially for large-scale power systems.

As a future work, ensemble learning, incorporating multiple learning methods, can be applied for prediction of PTS. Moreover, incorporating data from renewable energy generation sources (such as wind and solar) in the SVM training model can prove to be very useful in online DSA procedure.

TABLE II
SVM PERFORMANCE ASSESSMENT USING VARIOUS CLASSIFICATION METRICS

Classification Metric	**Value**
CA	0.967
CE	0.033
AUC	0.991

TABLE III
Variation of *CA*, *CE*, *AUC* For Different Kernel Functions

Kernel Function	*CA*	*CE*	*AUC*
Linear	0.872	0.128	0.894
Polynomial (order 2)	0.916	0.084	0.937
Polynomial (order 3)	0.829	0.171	0.848
Gaussian RBF	0.967	0.033	0.991

TABLE IV
Optimal Hyperparameter Values For The Proposed SVM Model

Hyperparameter	Type/value
Kernel function	RBF
Penalty Factor, *C*	210
Gamma, γ	0.22
Sigma, σ	1.5

TABLE V
Comparison Of SVM Performance Metrics With Related Research

Approach type	*CA*	*CE*
Proposed in this paper	0.967	0.033
[38]	0.893	0.107
[45]	0.959	0.041
[72]	0.968	0.032
[81]	0.935	0.065

TABLE VI
Comparison Of Proposed SVM Method With Traditional Methods

Approach type	Time (s)
SVM (proposed in this paper)	0.005
Time-domain	1.26
EEAC	0.91
TEF	0.86
Hybrid (time-domain+TEF)	1.04

References

[1] M. P. Bhavaraju, R. Billinton, R. E. Brown, J. Endrenyi, W. Li, A. P. Meliopoulos, and C. Singh, “IEEE Tutorial on electric delivery system reliability evaluation,” in *Proc. IEEE Power Energy Soc. Gen. Meet.*, 2005, pp. 68-78.

[2] P. Kundur, J. Paserba, V. Ajjarapu, G. Andersson, A. Bose, C. Canizares, N. Hatziargyriou, D. Hill, A. Stankovic, C. Taylor, T. V. Cutsem, and V. Vittal, “Definition and classification of power system stability IEEE/CIGRE joint task force on stability terms and definitions,” *IEEE Trans. Power Syst.*, vol. 19, no. 3, pp. 1387-1401, Aug. 2004.

[3] A. M. A. Haidar, M. W. Mustafa, F. A. F. Ibrahim, and I. A. Ahmed, “Transient stability evaluation of electrical power system using generalized regression neural networks*,” Appl. Soft Comp*., vol. 1, no. 4, pp. 3558-3570, Jun. 2011.

[4] A. L. Bettiol, A. Souza, J. L. Todesco, and J. R. Tesch, “Estimation of critical clearing times using neural networks,” in *Proc. IEEE Bologna Pow. Tech Conf.*, 2003, pp. 1-6.

[5] A. Karami, “Power system transient stability margin estimation using neural networks,” *Int. J. Electr. Power Energy Syst.*, vol. 33, no. 4, pp. 983-991, May 2011.

[6] M. A. Pai, *Energy Function Analysis for Power System Stability*. Boston, MA, USA: Kluwer, 1989.

[7] A. A. Fouad and V. Vittal, *Power System Transient Stability Analysis Using the Transient Energy Function Method*. Upper Saddle River, NJ, USA: Prentice-Hall, 1992.

[8] Y. Xue, T. V. Cutsem, and M. Ribbens-Pavella, “Extended equal area criterion justifications, generalizations, applications,” *IEEE Trans. Power Syst.*, vol. 4, no. 1, pp. 44-52, Feb. 1989.

[9] L. D. Colvara, “Stability analysis of power systems described with detailed models by automatic method,” *Int. J. Electr. Power Energy Syst.*, vol. 31, no. 4, pp. 139-145, May 2009.

[10] H. Sawhney and B. Jeyasurya, “A feed-forward artificial neural network with enhanced feature selection for power system transient stability assessment,” *Elect. Power Syst. Res.,* vol. 76, no. 12, pp. 1047-1054, Aug. 2006.

[11] J. G. Slootweg and W. L. Kling, “Impacts of distributed generation on power system transient stability,” in *Proc. IEEE Power Energy Soc. Gen. Meet.*, 2002, pp. 862-867.

[12] A. M. Azmy and I. Erlich, “Impact of distributed generation on the stability of electrical power system,” in *Proc. IEEE Power Energy Soc. Gen. Meet.*, 2005, pp. 1056-1063.

[13] A. Khosravi, M. Jazaeri, and S. A. Mousavi, “Transient stability evaluation of power systems with large amounts of distributed generation,” in *Proc. Intl. Uni. Power Eng. Conf.*, 2010, pp. 1-5.

[14] X. Zhao and J. Zhou, “Probabilistic transient stability assessment based on distributed DSA computation tool,” in *Proc. PMAPS.,* 2010, pp. 685-690.

[15] R. Billinton and P. R. S. Kuruganty, “Probabilistic assessment of transient stability in a practical multimachine system,” *IEEE Trans. Power App. Syst.*, vol. PAS-100, no. 7, pp. 3634–3641, Jul. 1981.

[16] Y.-Y. Hsu and C. Chung-Liang, “Probabilistic transient stability studies using the conditional probability approach,” *IEEE Trans. Power Syst.*, vol. 3, no. 4, pp. 1565–1572, Nov. 1988.

[17] E. Vaahedi, W. Li, T. Chia, and H. Dommel, “Large scale probabilistic transient stability assessment using B.C. Hydro’s on-line tool,” *IEEE Trans. Power Syst.*, vol. 15, no. 2, pp. 661–667, May 2000.

[18] P. M. Anderson and A. Bose, “A probabilistic approach to power system stability analysis,” *IEEE Trans. Power App. Syst.*, vol. PAS-102, no. 8, pp. 2430–2439, Aug. 1983.

[19] K. J. Timko, A. Bose, and P. M. Anderson, “Monte Carlo simulation of power system stability,” *IEEE Trans. Power App. Syst.*, vol. PAS-102, no. 10, pp. 3453–3459, Oct. 1983.

[20] W. Li, “Probabilistic transient stability assessment,” in *Risk Assessment of Power Systems: Models, Methods, and Applications*. New York, NY, USA: Wiley-IEEE Press, 2014.

[21] P. N. Papadopoulos and J. V. Milanović, “Probabilistic framework for transient stability assessment of power systems with high penetration of renewable generation,” *IEEE Trans. Power Syst.,* vol. 32, no. 4, pp. 3078-3088, Jul. 2017.

[22] M. Abapour and M. Haghifam, “Probabilistic transient stability assessment for on-line applications,” *Int. J. Electr. Power Energy Syst.*, vol. 42, no. 1, pp. 627-634, Nov. 2012.

[23] J. Fang, W. Yao, J. Wen, S. Cheng, Y. Tang, and Z. Cheng, “Probabilistic assessment of power system transient stability incorporating SMES,” *Phy. C: Supercond.*, vol. 484, pp. 276-281, Jan. 2013.

[24] S. O. Faried, R. Billinton, and S. Aboreshaid, “Probabilistic evaluation of transient stability of a power system incorporating wind farms,” *IET Ren. Power Gen.*, vol. 4, no. 4, pp. 299-307, Jul. 2010.

[25] S. O. Faried, R. Billinton, and S. Aboreshaid, “Probabilistic evaluation of transient stability of a wind farm,” *IEEE Trans. Energy Convers.*, vol. 24, no. 3, pp. 733-739, Sep. 2009.

[26] R. Billinton and P. R. S. Kuruganty, “Probabilistic considerations in transient stability assessment,” *Canad. Electr. Eng. J.*, vol. 4, no. 2, pp. 26-30, Apr. 1979.

[27] L. Shi, S. Sun, L. Yao, Y. Ni, and M. Bazargan, "Effects of wind generation intermittency and volatility on power system transient stability," *IET Ren. Power Gen.*, vol. 8, no. 5, pp. 509-521, Jul. 2014.

[28] D. Han, J. Ma, A. Xue, T. Lin, and G. Zhang, "The uncertainty and its influence of wind generated power on power system transient stability under different penetration," in *Proc. Int. Conf. Power Syst. Tech.*, 2014, pp. 675-680.

[29] M. Al-Sarray, H. Mhiesan, M. Saadeh ,and R. McCann, "A probabilistic approach for transient stability analysis of power systems with solar photovoltaic energy sources," in *Proc. GreenTech*, 2016, pp. 159-163.

[30] P. Ju, H. Li, C. Gan, Y. Liu, Y. Yu, and Y. Liu, "Analytical assessment for transient stability under stochastic continuous disturbances," *IEEE Trans. Power App. Syst*., vol. 33, no. 2, pp. 2004-2014, Mar. 2018.

[31] D. J. Sobajic and Y. Pao, "Artificial neural-net based dynamic security assessment for electric power systems," *IEEE Trans. Power App. Syst*., vol. 4, no. 1, pp. 220-228, Feb. 1989.

[32] M. Djukanovic, D. J. Sobajic, and Y. Pao, "Neural-net based unstable machine identification using individual energy functions," *Int. J. Electr. Power Energy Syst.*, vol. 13, no. 5, pp. 255-262, Oct. 1991.

[33] Y. Pao and D. J. Sobajic, "Combined use of unsupervised and supervised learning for dynamic security assessment," *IEEE Trans. Power App. Syst*., vol. 7, no. 2, pp. 878-884, May 1992.

[34] M. S. Ibrahim, W. Dong, and Q. Yang, "Machine learning driven smart electric power systems: Current trends and new perspectives," *Appl. Energy*, vol. 272, pp. 1-19. Aug. 2020.

[35] R. Saravanan and P. Sujatha, "A state of art techniques on machine learning algorithms: a perspective of supervised learning approaches in data classification," in *Proc. ICICCS*, 2018, pp. 945-949.

[36] T. S. Dillon, and D. Niebur, *Neural Networks Applications in Power Systems*. Leicestershire, UK: CRL Publishing, 1996.

[37] S. Kalyani and K. S. Swarup, "Classification and assessment of power system security using multiclass SVM," *IEEE Trans. Syst., Man, Cybern A., Syst., Humans,* vol. 41, no. 5, pp. 753-758, Sep. 2011.

[38] D. You, K. Wang, L. Ye, J. Wu, and R. Huang, "Transient stability assessment of power system using support vector machine with generator combinatorial trajectories inputs", *Int. J. Electr. Power Energy Syst.*, vol. 44, no. 1, pp. 318-325, Jan. 2013.

[39] L. S. Moulin, A. P. A. da Silva, M. A. El-Sharkawi, and R. J. Marks, "Support vector machines for transient stability analysis of large-scale power systems," *IEEE Trans. Power App. Syst*., vol. 19, no. 2, pp. 818-825, May 2004.

[40] A. D. Rajapakse, F. Gomez, K. Nanayakkara, P. A. Crossley, and V. V. Terzija, "Rotor angle instability prediction using post-disturbance voltage trajectories," *IEEE Trans. Power App. Syst.,* vol. 25, no. 2, pp. 947-956, May 2010.

[41] B. P. Soni, A. Saxena, V. Gupta, and S. L. Surana, "Assessment of transient stability through coherent machine identification by using least-square support vector machine", *Mod. Simul. Eng*., vol. 2018, pp. 1-18, May 2018.

[42] F. R. Gomez, A. D. Rajapakse, U. D. Annakkage, and I. T. Fernando, "Support vector machine-based algorithm for post-fault transient stability status prediction using synchronized measurements," *IEEE Trans. Power App. Syst.*, vol. 26, no. 3, pp. 1474-1483, Aug. 2011.

[43] P. Pavani and S. N. Singh, "Support vector machine based transient stability identification in distribution system with distributed generation," *Electr. Power Comp. Syst.,* vol. 44, no. 1, pp. 60-71, Nov. 2015.

[44] A. E. Gavoyiannis, D. G. Vogiatzis, D. R. Georgiadis, and N. D. Hatziargyriou, "Combined support vector classifiers using fuzzy clustering for dynamic security assessment," in *Proc. IEEE Power Energy Soc. Gen. Meet*., 2001, pp. 1281-1286.

[45] S. Ye, X. Li, X. Wang, and Q. Qian, "Power system transient stability assessment based on adaboost and support vector machines," in *Proc. Asia-Pacific Power Ener. Eng. Conf.*, 2012, pp. 1-4.

[46] L. S. Moulin, A. P. A. da Silva, M . A. El-Sharkawi, and R. J. Marks, "Neural networks and support vector machines applied to power systems transient stability analysis," *Int. J. Eng. Intel. Syst. Elect. Eng. Comm*., vol. 9, no. 4, pp. 205-211, Nov. 2001.

[47] N. I. A. Wahab, A. Mohamed, and A. Hussain, "Transient stability assessment of a power system using PNN and LS-SVM methods," *J. Appl. Sci*., vol. 7, no. 21, pp. 3208-3216, 2007.

[48] B. D. A. Selvi and N. Kamaraj, "Investigation of power system transient stability using clustering based support vector machines and preventive control by rescheduling generators," in *Proc. ICTES*, 2007, pp. 137-142.

[49] N. G. Baltas, P. Mazidi, J. Ma, F. A. Fernandez, and P. Rodriguez, "A comparative analysis of decision trees, support vector machines and artificial neural networks for on-line transient stability assessment," in *Proc SEST*, 2018, pp. 1-6.

[50] M. Arefi and B. Chowdhury, "Ensemble adaptive neuro fuzzy support vector machine for prediction of transient stability," in *Proc. NAPS*, 2017, pp. 1-6.

[51] E. A. Frimpong, P. Y. Okyere, and J. Asumadu, "Prediction of transient stability status using Walsh-Hadamard transform and support vector machine," in *Proc. IEEE PES PowerAfrica*, 2017, pp. 301-306.

[52] B. D. A. Selvi and N. Kamaraj, "Support vector regression machine with enhanced feature selection for transient stability evaluation," in *Asia-Pacific Pow. and Energy Eng. Conf.*, 2009, pp. 1-5.

[53] A. Sabo and N. I. A. Wahab, "Rotor angle transient stability methodologies of power systems: a comparison," in *IEEE Student Conf. on Res. and Dev.*, 2019, pp. 1-6.

[54] W. Li and J. Zhou, "Probabilistic reliability assessment of power system operations," *Electr. Power Comp. Syst*., vol. 36, no. 10, pp. 1102-1114, Sep. 2008.

[55] J. L. Cremer and G. Strbac, "A machine-learning based probabilistic perspective on dynamic security assessment," *Int. J. Electr. Power Energy Syst.*, vol. 128, pp. 1-15, Jun. 2021.

[56] H. Yuan, J. Tan, and Y. Zhang, "Machine learning-based security assessment and control for bulk electric system operation," NREL, Feb. 2020. [Online]. Available:

https://www.nrel.gov/docs/fy21osti/76089.pdf

[57] T. Zhang, M. Sun, J. L. Cremer, N. Zhang, G. Strbac, and C. Kang, "A confidence-aware machine learning framework for dynamic security assessment," *IEEE Trans. Power Syst.*, pp. 1-14, Feb. 2021.

[58] K. Jayashree and K. S. Swarup, "A distributed computing environment for probabilistic transient stability analysis," in *16th Nat. Power Syst. Conf.,* 2010, pp. 329-335.

[59] P. N. Papadopoulos and J. V. Milanović, "Impact of penetration of non-synchronous generators on power system dynamics," in *Proc. IEEE Eindhoven Power Tech*., 2015, pp. 1-6.

[60] V. Vapnik, *Statistical Learning Theory*. New York, NY, USA: John Wiley & Sons, 1998.

[61] V. Vapnik, *The Nature of Statistical Learning Theory*. New York, NY, USA: Springer-Verlag, 1995.

[62] B. Scholköpf, C. Burges, and A. Smola, *Advances in Kernel Methods—Support Vector Learning*. Cambridge, MA, USA: MIT Press, 1999.

[63] E. Osuna, R. Freund, and F. Girosi, "Training support vector machines: au application to face detection," in *Proc. CVPR*, 1997, pp. 1-8.

[64] T. Joachims, "Making large-scale SVM learning practical," in *Advances in Kernel Methods - Support Vector Learning.* Cambridge, MA, USA: MIT Press, 1998.

[65] N. Cristianini and J. Shawe-Taylor, *An Introduction to Support Vector Machines and Other Kernel-Based Learning Methods*. Cambridge, UK: Cambridge University Press, 2000.

[66] G. N. Baltas, P. Mazidi, F. Fernandez, and P. Rodríguez, "Support vector machine and neural network applications in transient stability," in *Proc. ICRERA*, 2018, pp. 1010-1015.

[67] C. Savas and F. Dovis, "The impact of different kernel functions on the performance of scintillation detection based on support vector machines," *Sensors*, vol. 19, no. 23, pp. 1-16, Nov. 2019.

[68] L. S. Moulin, A. P. A. da Silva, M. A. El-Sharkawi, and R. J. Marks, "Support vector and multilayer perceptron neural networks applied to power systems transient stability analysis with input dimensionality reduction," in *Proc. IEEE Power Energy Soc. Gen. Meet.*, 2002, pp. 1308-1313.

[69] Power Systems Test Case Archive. [Online]. Available: http://www.ee.washington.edu/research/pstca/pf14/pg_tca14bus.htm

[70] DIgSILENT PowerFactory User Manual, DIgSILENT GmbH, 2018. [Online]. Available: https://www.digsilent.de/en/downloads.html

[71] Classification Learner. [Online]. Available: https://www.mathworks.com/help/stats/classificationlearner-app.html

[72] N. I. A. Wahab, A. Mohamed, and A. Hussain, "Fast transient stability assessment of large power system using probabilistic neural network with feature reduction techniques," *Exp. Syst. Appl.*, vol. 38, no. 9, pp. 11112-11119, Sep. 2011.

[73] Using the ROC curve to analyze a classification model. [Online]. Available: http://www.math.utah.edu/~gamez/files/ROC-Curves.pdf

[74] C. Sammut and G. I. Webb, *Encyclopedia of Machine Learning*. New York, NY, USA: Springer, 2011.

[75] S. Karamizadeh, S. M. Abdullah, M. Halimi, J. Shayan and M. J. Rajabi, "Advantage and drawback of support vector machine functionality," in *International Conf. on Comput., Commun., and Contr. Tech.*, 2014, pp. 63-65.

[76] L. Duchesne, E. Karangelos, and L. Wehenkel, "Recent developments in machine learning for energy systems reliability management," *Proc. IEEE*, vol. 108, no. 9, pp. 1656-1676, Sep. 2020.

[77] J. Brownlee, A gentle introduction to k-fold cross-validation, 2018. [Online]. Available: https://machinelearningmastery.com/k-fold-cross-validation/

[78] C. Wang and F. Liu, "An improved support vector machine method for transient stability assessment in bulk power grid," in *Proc. IEEE Sustain. Power and Energy Conf.*, 2020, pp. 2423-2428.

[79] Q. Wang, C. Pang, and H. Alnami, "Transient stability assessment of a power system using multi-layer SVM method," in *Proc. IEEE Texas Power and Energy Conf.*, 2021, pp. 1-5.

[80] C. Wang, S. Li, C. Lin, and H. Chen, "Transient stability assessment of power system based on enhanced projection twin SVM," in *Proc. IEEE Int. Conf. on Digit. Twins and Parallel Intell.*, 2021, pp. 148-151.

[81] E. M. Voumvoulakis, A. E. Gavoyiannis, and N. D. Hatziargyriou, "Application of machine learning on power system dynamic security assessment," in *Proc. Int. Conf. on Intell. Systems Appl. to Power Syst.*, 2007, pp. 1-6.

Umair Shahzad was born in Faisalabad, Pakistan. In 2021, he received the Ph.D. degree in Electrical Engineering from The University of Nebraska-Lincoln, USA, as a Fulbright Scholar. Moreover, he received a B.Sc. Electrical Engineering degree from the University of Engineering and Technology, Lahore, Pakistan, and a M.Sc. Electrical Engineering degree from The University of Nottingham, England, in 2010 and 2012, respectively. His research interests include power system security assessment, power system stability, machine learning, and probabilistic methods applied to power systems.